Distribution Functions of Rotating Galaxies: an Integral Field Spectroscopy Perspective

---

Simona Bekeraitė

Dissertation zur Erlangung des akademischen Grades "doctor rerum naturalium" (Dr. rer. nat.) in der Wissenschaftsdisziplin Astrophysik

Dissertation eingereicht an der Mathematisch-Naturwissenschaftlichen Fakultät der Universität Potsdam und Leibniz-Institut Für Astrophysik Potsdam

August 2017

Hauptbetreuer: prof. Dr. Lutz Wisotzki
Betreuer: prof. Dr. Martin Roth
Betreuer: Dr. C.J. Walcher

Published online at the
Institutional Repository of the University of Potsdam:
URN urn:nbn:de:kobv:517-opus4-420950
http://nbn-resolving.de/urn:nbn:de:kobv:517-opus4-420950

Summary

The work done during the PhD studies has been focused on measurements of distribution functions of rotating galaxies using integral field spectroscopy observations.

Throughout the main body of research presented here we have been using CALIFA (Calar Alto Legacy Integral Field Area) survey stellar velocity fields to obtain robust measurements of circular velocities for rotating galaxies of all morphological types. A crucial part of the work was enabled by well-defined CALIFA sample selection criteria: it enabled reconstructing sample-independent distributions of galaxy properties.

In Chapter 2, we measure the distribution in absolute magnitude - circular velocity space for a well-defined sample of 199 rotating CALIFA galaxies using their stellar kinematics. Our aim in this analysis is to avoid subjective selection criteria and to take volume and large-scale structure factors into account. Using stellar velocity fields instead of gas emission line kinematics allows including rapidly rotating early type galaxies. Our initial sample contains 277 galaxies with available stellar velocity fields and growth curve r-band photometry. After rejecting 51 velocity fields that could not be modelled due to the low number of bins, foreground contamination or significant interaction we perform Markov Chain Monte Carlo (MCMC) modelling of the velocity fields, obtaining the rotation curve and kinematic parameters and their realistic uncertainties. We perform an extinction correction and calculate the circular velocity $v_{\rm circ}$ accounting for pressure support a given galaxy has. The resulting galaxy distribution on the M_r - $v_{\rm circ}$ plane is then modelled as a mixture of two distinct populations, allowing robust and reproducible rejection of outliers, a significant fraction of which are slow rotators. The selection effects are understood well enough that the incompleteness of the sample can be corrected and the 199 galaxies can be weighted by volume and large-scale structure factors enabling us to fit a volume-corrected Tully-Fisher relation (TFR). More importantly, we also provide the volume-corrected distribution of galaxies in the M_r - $v_{\rm circ}$ plane, which can be compared with cosmological simulations. The joint distribution of the luminosity and circular velocity space densities, representative over the range of -20 > M_r > -22 mag, can place more stringent constraints on the galaxy formation and evolution scenarios than linear TFR fit parameters or the luminosity function alone.

In Chapter 3, we measure one of the marginal distributions of the M_r - $v_{\rm circ}$ distribution: the circular velocity function of rotating galaxies. The velocity function is a fundamental observable statistic of the galaxy population, being of a similar importance as the luminosity function, but much more difficult to measure. We present the first directly measured circular velocity function that is representative between $60 < v_{\rm circ} < 320$ km s^{-1} for galaxies of all morphological types at a given rotation velocity. For

the low mass galaxy population ($60 < v_{\rm circ} < 170$ km s^{-1}), we use the HIPASS velocity function. For the massive galaxy population ($170 < v_{\rm circ} < 320$ km s^{-1}), we use stellar circular velocities from CALIFA. The CALIFA velocity function includes homogeneous velocity measurements of both late and early-type rotation-supported galaxies. It has the crucial advantage of not missing gas-poor massive ellipticals that HI surveys are blind to. We show that both velocity functions can be combined in a seamless manner, as their ranges of validity overlap. The resulting observed velocity function is compared to velocity functions derived from cosmological simulations of the $z = 0$ galaxy population. We find that dark matter-only simulations show a strong mismatch with the observed VF. Hydrodynamic Illustris simulations fare better, but still do not fully reproduce observations.

In Chapter 4, we present some other work done during the PhD studies, namely, a method that improves the precision of specific angular measurements by combining simultaneous Markov Chain Monte Carlo modelling of ionised gas 2D velocity fields and HI linewidths. To test the method we use a sample of 25 galaxies from the Sydney-AAO Multi-object Integral field (SAMI) survey that had matching ALFALFA HI linewidths. Such a method allows constraining the rotation curve both in the inner regions of a galaxy and in its outskirts, leading to increased precision of specific angular momentum measurements. It could be used to further constrain the observed relation between galaxy mass, specific angular momentum and morphology (Obreschkow & Glazebrook 2014).

Mathematical and computational methods are presented in the appendices.

Zusammenfassung

Die Arbeit, die während dises Promotionsstudiums durchgeführt wurde, konzentrierte sich auf die Messungen von Verteilungsfunktionen rotierender Galaxien, unter Verwendung von integralen Feldspektroskopiebeobachtungen.

Im Rahmen der hier vorgestellten Hauptforschung haben wir CALIFA (Calar Alto Legacy Integral Field Area) mit stellaren Geschwindigkeitsfeldern verwendet, um robuste Messungen von Kreisförmigen Geschwindigkeiten für rotierende Galaxien aller Morphologien zu erhalten. Der entscheidende Teil dieser Arbeit wurde durch wohl definierte CALIFA-Probenselektionskriterien ermöglicht: Es ermöglichte die Rekonstruktion von probenunabhängigen Verteilungen von Galaxieneigenschaften.

In Kapitel 2 messen wir die Verteilung in absoluten Magnituden für eine wohldefinierte Stichprobe von 199 rotierenden CALIFA-Galaxien unter Berücksichtigung ihrer stellaren Kinematik. Das Ziel in dieser Analyse ist es, subjektive Auswahlkriterien zu vermeiden und Volumenfaktoren und Faktoren großräumiger Strukturen zu berücksichtigen. Die Verwendung von stellaren Geschwindigkeitsfeldern statt der Gas-Emissionslinien-Kinematik ermöglicht auch schnell rotierende frühe Galaxien zu berücksichtigen.

Unsere erstes Sample enthält 277 Galaxien mit verfügbaren stellaren Geschwindigkeitsfeldern und eine *r*-Band-Photometrie Wachstumskurve. Nach der Verwerfung von 51 Geschwindigkeitsfeldern, die aufgrund der geringen Anzahl von Bins, der Vordergrundverunreinigung oder der signifikanten Interaktion nicht modelliert werden konnten, führen wir die Modellierung der Geschwindigkeitsfelder mit Markov-Ketten-Monte-Carlo (MCMC) durch, wobei die Rotationskurve und die kinematischen Parameter und deren realistischen Unsicherheiten enthalten sind. Wir führen eine Extinktionskorrektur durch und berechnen die Kreisgeschwindigkeit $v_{\rm circ}$ unter Berücksichtigung der Druckunterstützung des gegebenen Galaxien-Bias.

Die daraus resultierende Galaxienverteilung auf der M_r - $v_{\rm circ}$-Ebene wird dann als Mischung aus zwei verschiedenen Populationen modelliert, was eine robuste und reproduzierbare Verwerfung von Ausreißern ermöglicht, deren signifikanter Bruchteil langsame Rotatoren sind. Die Selektionseffekte sind verstanden genug, damit die Unvollständigkeit der Probe korrigiert werden kann und die 199 Galaxien durch Volumen und großräumige Strukturen gewichtet werde können, um es uns ermöglichen, eine volumenkorrigierte Tully-Fisher-Relation (TFR) anzupassen. Noch wichtiger ist es, dass wir auch die volumenkorrigierte Verteilung von Galaxien in der M_r - $v_{\rm circ}$ Ebene bereitstellen, die mit kosmologischen Simulationen verglichen werden können. Die gemeinsame Verteilung der Helligkeits- und Kreisgeschwindigkeitsraumdichten, die über den Bereich von -20 > M_r > -22 Mag repräsentativ sind, kann strengere Einschränkungen für die Galaxienbildung und Evolutionsszenarien als lineare TFR-Fit-Parameter oder

die Luminositätsfunktion setzen .

In Kapitel 3 messen wir eine der Randverteilungen der M_r - $v_{\rm circ}$ Verteilung: die Kreisgeschwindigkeitsfunktion der rotierenden Galaxien. Die Geschwindigkeitsfunktion ist eine fundamentale, beobachtbare Messgröße der Galaxienpopulationen, welche von ähnlicher Bedeutung ist wie die Helligkeitsfunktion, aber viel schwerer zu messen ist. Wir präsentieren die erste direkt gemessene Kreisgeschwindigkeitsfunktion, die bei einer gegebenen Rotationsgeschwindigkeit zwischen $60 < v_{\rm circ} < 320$ km s $^{-1}$ für Galaxien aller morphologischen Typen repräsentativ ist.

Für die Galaxienpopulation mit niedrigen Massen ($60 < v_{\rm circ} < 170$ km s $^{-1}$) verwenden wir die HIPASS-Geschwindigkeitsfunktion.

Für die massiven Galaxienpopulationen ($170 < v_{\rm circ} < 320$ km s $^{-1}$) verwenden wir stellare Kreisgeschwindigkeiten von CALIFA.

Die CALIFA-Geschwindigkeitsfunktion umfasst homogene Geschwindigkeitsmessungen sowohl der späten als auch der frühen Rotations-gestützten Galaxien. Sie hat den entscheidenden Vorteil Gas-arme, massive elliptische Galaxien nicht zu verfehlen, was bei HI-Surveys der Fall ist. Wir zeigen, dass beide Geschwindigkeitsfunktionen nahtlos kombiniert werden können, da sich ihre Gültigkeitsbereiche überschneiden. Die resultierende beobachtete Geschwindigkeitsfunktion wird mit Geschwindigkeitsfunktionen verglichen, die von kosmologischen Simulationen bei $z = 0$ Galaxien abgeleitet sind.

Wir finden, dass dunkle Materie-Simulationen eine starke Diskrepanz mit dem beobachteten VF vorweisen. Hydrodynamische Illustris Simulationen passen besser, aber reproduzieren immer noch nicht vollständig die Beobachtungen.

In Kapitel 4 stellen wir einige andere Arbeiten vor, die während der Promotion durchgeführt wurden, nämlich eine Methode, die die Präzision bestimmter Winkelmessungen durch die Kombination der gleichzeitigen Markov-Kette-Monte-Carlo Modellierung von ionisierten Gas 2D Geschwindigkeitsfeldern und HI Linienbreiten verbessert. Um diese Methode zu testen, verwenden wir eine Stichprobe von 25 Galaxien aus der Sydney-AAO Multi-Objekt Integral Field (SAMI) Surveys, welche die passenden ALFALFA HI Linenbreite hatte.

Ein solches Verfahren ermöglicht es, die Rotationskurve sowohl in den inneren Bereichen einer Galaxie als auch in ihrem Außenbereich zu bestimmen, was zu einer erhöhten Präzision spezifischer Drehimpulsmessungen führt. Es könnte verwendet werden, um die beobachtete Beziehung zwischen Galaxienmasse, spezifischem Drehimpuls und Morphologie (Obreschkow & Glazebrook 2014) weiter zu verfeinern.

Mathematische und rechnerische Methoden werden in den Anhängen dargestellt.

Contents

1 Introduction **1**
- 1.1 Galaxy formation in ΛCDM cosmology . . . 1
- 1.2 Galaxy distribution functions . . . 2
- 1.3 Origin of galaxy angular momentum . . . 3
  - 1.3.1 Alignments of angular momentum . . . 4
- 1.4 Integral Field Spectroscopy . . . 4
  - 1.4.1 Overview . . . 4
  - 1.4.2 IFS studies of galaxy kinematics and dynamics . . . 6
  - 1.4.3 The CALIFA survey . . . 7
  - 1.4.4 CALIFA sample characterisation . . . 8
- 1.5 Outline of the thesis . . . 11

2 The space density distribution of galaxies in the absolute magnitude - rotation velocity plane **12**
- 2.1 Abstract . . . 12
- 2.2 Introduction . . . 13
  - 2.2.1 The Tully-Fisher relation . . . 13
- 2.3 Data, sample selection, and characterisation . . . 17
  - 2.3.1 CALIFA Survey . . . 17
  - 2.3.2 Volume corrections . . . 19
- 2.4 Luminosity data . . . 20
  - 2.4.1 Observed magnitudes . . . 20
  - 2.4.2 Corrections for intrinsic absorption . . . 21
- 2.5 Velocity field modelling . . . 24
  - 2.5.1 Model description . . . 24
  - 2.5.2 Definition of rotation velocity measure . . . 26
  - 2.5.3 Modelling results and uncertainties . . . 27
  - 2.5.4 Calculating the circular velocity . . . 30
- 2.6 Separation of different populations of galaxies in the M_r - $v_{\rm circ}$ plane . . . 33
  - 2.6.1 Specific angular momentum . . . 33
  - 2.6.2 Modelling the TFR as a mixture of Gaussians . . . 34
  - 2.6.3 Properties of the outlier galaxies . . . 35
  - 2.6.4 Properties of the Tully-Fisher sample . . . 36
- 2.7 Tully-Fisher relation . . . 38
- 2.8 Volume-corrected bivariate distribution function in the Tully-Fisher plane 41

2.9 Conclusions 44

3 The CALIFA and HIPASS Circular Velocity Function for All Morphological Galaxy Types 45
3.1 Abstract 45
3.2 Introduction 46
3.3 CALIFA stellar circular velocity measurements 47
3.4 Results 48
3.4.1 CALIFA circular velocity function 48
3.4.2 Uncertainties 48
3.4.3 Combined CALIFA-HIPASS circular velocity function 50
3.4.4 Discussion 51
3.4.5 Comparison with simulations 53
3.5 Conclusions 54

4 Combining SAMI IFU data with HI linewidths for precision angular momentum measurements 55
4.1 Introduction 55
4.2 Feasibility tests using the THINGS data 56
4.3 Observations and sample 60
4.4 Fitting the velocity fields 60
4.5 Discussion 63

5 Conclusions and outlook 68
5.1 Conclusions 68
5.2 Outlook 69

Appendix A: growth curve photometry measurements 71

Appendix B: Two-dimensional Gaussian kernel density estimation 77

Bibliography 81

Chapter 1

Introduction

1.1 Galaxy formation in ΛCDM cosmology

Hierarchical cold dark matter model (Blumenthal et al. 1982, 1984; Davis et al. 1985) has become the preferred model of structure assembly during the last few decades.

In the current cosmological paradigm, which includes the ΛCDM model and inflation, the Universe started with a hot Big Bang, most likely followed by a brief period of exponential expansion (Guth 1981; Linde 1982).

The components of our Universe can be classified by their equation of state:

- Non-relativistic matter
- Relativistic matter (photons, neutrinos)
- The "dark energy", or the cosmological constant Λ

The current consensus model, the so-called Benchmark Model, assumes that the Universe is homogeneous, isotropic, and spatially flat. The density parameters of the components of the Universe adopted by the Benchmark Model, and through this work, are $\Omega_m = 0.3$ and $\Omega_\Lambda = 0.7$. Ω_m is equal to the sum of baryonic matter density parameter $\Omega_b = 0.04$ and dark matter density parameter $\Omega_{DM} = 0.26$.

The current cosmology paradigm which includes the expansion term, Λ, was first envisioned in the 1990s as a part of an effort to explain the observed amount of clustering on large scales. The existance of the dark energy component was confirmed in 1999 by observations of type Ia supernovae (Schmidt et al. 1998; Riess et al. 1998; Perlmutter et al. 1999). The ΛCDM paradigm remains the best model of the Universe, with its parameter values matching and increasingly constrained by independent observations of large scale clustering, dark energy density, cosmic microwave background and other observation.

The fact that the observed luminous objects cannot account for a significant fraction of mass in the Universe was first noticed back in 1930's, based on motions of galaxies in the Coma cluster (Zwicky 1937). Later on this currently prevailing idea gained ground, moved by additional pieces of evidence such as galaxy disk and cluster stability studies (Ostriker & Peebles 1973; Einasto et al. 1974) and rotation curves of spiral galaxies (Rubin & Ford 1970; Roberts 1976; Bosma 1978; Rubin et al. 1978).

According to the current galaxy formation scenario, the structures we now observe started to grow via gravitational instabilities from quantum fluctuations in the inflation field. The resulting density field is assumed to be Gaussian, with a nearly scale-invariant initial fluctuation spectrum. The observations of density distribution just after recombination, imprinted on the cosmic microwave background, confirm the picture so far (Planck Collaboration et al. 2014).

The initial Gaussian perturbations initially grew linearly with time, in an interplay between gravitational self-attraction and the expansion of the Universe. Galaxies form at the Gaussian density field peaks through ellipsoidal collapse (Sheth et al. 2001) in which a halo ceases expanding with the Hubble flow and starts contracting under its own gravity. The subsequent structure assembly is usually analysed as highly non-linear collapse of dark matter into dense haloes, followed by the baryonic matter which settles into the bottom of the resulting potential wells (White & Rees 1978). The baryon gas cools and fragments, eventually forming the luminous galaxies.

1.2 Galaxy distribution functions

With the advent of large surveys and large, resolved cosmological simulations it has become possible to investigate the statistical properties of the galaxy population. The statistical relations could be divided into several groups:

1. Statistical distributions of individual galaxy properties. It is not possible yet to obtain a full multidimensional distribution function of important galaxy properties (luminosity, size, morphology, dynamical state, colour, nuclear activity, mass, etc.), however, even the marginal distributions are helpful in understanding the formation and evolution of galaxies (Mo et al. 2010). The most important observed distribution functions in this regard are the luminosity, size and stellar mass functions, correlations between luminosity, morphology and color, and between morphology, angular momentum and galaxy mass.

2. Relations between galaxies and their host haloes. Developments in theory and cosmological simulations allowed linking the observed intrinsic properties of galaxies with the dark matter halos they form in. Important relations include the relations between halo and stellar masses or luminosities, halo spin and galaxy disk size and, indirectly, the relation between rotation velocity and luminosity of rotating galaxies.

3. Relations between galaxies and their environment: morphology-density relation, statistical differences between colours and luminosities of central and satellite galaxies.

4. Relations between galaxy properties and their super-halo scale environment, for example, indications of assembly bias (dependence of halo clustering on assembly history) and spin alignment with the large-scale structure.

5. Spatial distribution statistics: two- and three-point correlation functions, power spectrum analysis and other statistics.

6. Properties of the unresolved galaxy population (extragalactic background light, cosmic shear).

7. Evolution of galaxy statistical properties with redshift.

1.3 Origin of galaxy angular momentum

Rotation-supported galaxies formed from cooling gas falling inward inside massive dark matter haloes, conserving its specific angular momentum. The angular momentum of dark matter haloes is, in essence, an environmental effect explained by the tidal torque theory (Peebles 1969; Doroshkevich 1970), also see a review in Schäfer (2009), which demonstrates how the angular momentum has been transferred to protogalaxies by the gravitational interaction with the tidal field of neighbouring structures. The maximum rate of the angular momentum transfer occurred at the stage when the halos had started to be denser than the surrounding field, but before they have collapsed and moved to larger distances due to the expansion of the Universe. Each halo acquires a rotational motion component from the gravitational shear flows in which it is embedded. As the gravitational collapse of the halo continues and it contracts, the torquing becomes inefficient. The first N-body simulations (Peebles 1971; Efstathiou & Jones 1979), using 100 and 1000 particles respectively, have confirmed this picture. In addition, Efstathiou & Jones (1979) demonstrated that the disks could not have collapsed without being hosted by dark matter haloes, as predicted by White & Rees (1978).

Obviously, the halo angular momentum and the properties of the galaxy which forms inside the halo are closely linked. A dimensionless spin parameter λ describes the ratio between the angular velocity of a galaxy and the angular velocity which is necessary for it to be rotationally-supported (Schäfer 2009) or, roughly, the square root of the ratio between the rotational and total energy of the galaxy:

$$\lambda = \frac{L\sqrt{E}}{GM^{5/2}} \tag{1.1}$$

where L is the halo angular momentum, E is the gravitational binding energy and M is the mass. All these quantities (and, consequently, λ as well) are conserved in a system which evolves without dissipation. The initial specific angular momentum of the disk and halo particles, $j = L/M$, is thought be the same for the baryons and for the dark matter (van den Bosch et al. 2002; Mo et al. 2010) as they experience the same tidal forces.

The mean spin parameter of the dark matter halo population has been shown to be approximately equal to 0.035 with large dispersion, implying that the dark haloes are supported by anisotropic velocity dispersion. Disk galaxies, in contrast, are highly-flattened, rotation-supported systems with a characteristic $\lambda \approx 0.425$. Detailed calculations involving realistic dark halo density profiles and disk self-gravity agree with observations and show that baryons are expected to preserve their specific angular momentum during the disk formation (Mo et al. 2010).

1.3.1 Alignments of angular momentum

Since the angular momentum of haloes and, consequently, of galaxies, is an environmental effect, it is correlated with both the neighbouring structures and with large scale structure. Neighbouring dark matter haloes show alignment expressed by the spin-spin correlation function. Numerical simulations (Hahn et al. 2007) have shown that there is weak tendency of massive haloes in clusters and their close neighbours (closer than a few Mpc) to have antiparallel spins. Observations using Galaxy Zoo data detected spin chirality correlation of spiral galaxies at various spatial scales up to 10 Mpc, confirming that inertia tensors of nearby galaxies are indeed correlated (Slosar et al. 2009) and related to the environment in which the galaxies had formed (Jimenez et al. 2010).

Another form of spatial spin alignment is spin correlation with the surrounding large scale structure (sheets, clusters, filaments, voids), usually analysed via numerical simulations. In (Hahn et al. 2007) it is shown that dark matter angular momentum vectors tend to be parallel to the sheet the halo is in. Codis et al. (2012) detect a mass transition, claiming that spins of haloes with masses above $5{\times}10^{12}$ $M_{\odot}$ tend to be perpendicular to the nearest filament of the cosmic web, while those of low mass haloes tend to be aligned with the filaments. They interpret it as a fossil record of large-scale cosmic flows: the higher mass haloes form as mergers along the filaments, whereas the lower mass haloes form during intersection of misaligned walls which form a filament. Similar conclusions are made by Libeskind et al. (2012) and Trowland et al. (2013).

Observationally, the picture is not yet clear. Trujillo et al. (2006) use 2dFGRS and SDSS survey data to rule out the hypothesis that rotation axes of galaxies on the shell voids are aligned randomly. Lee & Erdogdu (2007) confirm the existence of spin axis correlations with the density field, finding an increasing trend with the Hubble type. Tempel et al. (2013) find that spin axes of bright spirals preferentially are aligned parallel to their host filaments, while ellipticals/S0s tend to be perpendicular to them. Extending their method to galaxies in sheets (Tempel & Libeskind 2013), they confirm such a picture, also finding much stronger correlation at the outer parts of a filament.

1.4 Integral Field Spectroscopy

1.4.1 Overview

Imaging spectroscopy uses instruments that provide spectroscopic information over a two-dimensional field-of-view, combining imaging (which normally has very crude wavelength resolution) and spectroscopy (providing little or no spatial information) and yielding a 3D data-cube with 2 spatial and 1 spectral dimension. 3D spectroscopy has been rapidly developing over the last few decades, moving from specialised portable instruments to dedicated general purpose instruments on many telescopes, as well as spilling over to another areas of research such as Earth observations, agriculture or medical science – see an instrumentation review by Hagen & Kudenov (2013).

Observations in other wavelengths than optical/IR (X-ray(Fraser 2009), millimeter/submillimeter interferometry (e.g. ALMA), radio (Wilson et al. 2013) also provide 3D data-cubes, although these methods are not classified as imaging spectroscopy.

Optical imaging spectroscopy instrumentation in astrophysics can be divided into

3 groups (Eisenhauer & Raab 2015):

1. **Scanning spectrometry**. Fabry-Pérot interferometers (Fabry & Perot 1901) is the most common tunable filter used to produce a series of images at different wavelengths, resulting in a data-cube. In these interferometers the beam goes through two very reflective parallel surfaces, which cause interference between the original beam and its reflections, resulting in strongly-wavelength dependent transmission. They can provide a wide field of view, however, accurate flux-calibration and flat-fielding is very complicated. Fourier-transform spectrometry, today largely supplanted by Fabry-Pérot instruments, obtain the source spectrum by feeding the light into an interferometer and performing an inverse Fourier transformation of the measured interferogram.

2. **Energy-resolving detector arrays** are exceptional in the sense that they do not require optics to obtain a spectrum – the detector itself is capable of measuring the energy of each incident photon. Still in a nascent, but promising, stage, such detectors are superconductor-based as their band gaps are orders of magnitude smaller than those of typical semiconductors.

3. **Integral field spectroscopy** uses integral field units (IFUs) which divide the 2D spatial field before passing it to a spectroscope. They have the benefit of simultaneously obtaining the full spectrum on all spaxels, and therefore minimising the impact of varying observing conditions (Eisenhauer & Raab 2015). Integral field spectroscopy is the most widely used imaging spectroscopy technique in astrophysics, described below in more detail.

Integral field spectroscopy instruments can be divided into three main groups based on their IFU design:

- **Image slicers**, first envisioned by Bowen (1938) as a means to improve light retention at the slit of a spectrograph, later applied to NIR (Weitzel et al. 1996) and optical observations. Image slicers are used to cut the image into slices using an array of thin mirrors, each of which sends light from its slice to a different channel. Each slice is then sent toward the spectrograph slit by the second set of mirrors. In this design, spatial sampling along the 1st axis occurs at the slicer, while spatial sampling along the second axis occurs at the detector. The advantages of image slicers include efficient CCD usage, no crosstalk between neighbouring pixels, high throughput and sensitivity. Despite challenging optics systems, image slicers are used on the largest telescopes, sometimes even employing adaptive optics and multi-IFU systems (Eisenhauer et al. 2003; Content 2006; Sharples et al. 2006; Bacon et al. 2010; Laurent et al. 2010).

- In **lenslet array**-based IFUs (Courtes 1982; Bacon et al. 1995), an array of microlenses is placed on the image plane. Each lenslet focuses light in the focal plane of the spectrograph, acting as a pixel. The advantages of lenslets are relatively simple design and high throughput, however, it comes with a cost of suboptimal detector space usage, spectral crosstalk and lower spectral coverage (Eisenhauer & Raab 2015). Instruments such as VIMOS (Le Fèvre et al. 2003), SAURON (Bacon et al. 2001) are using lenslet array IFUs.

- Optical **fiber IFU** systems (Vanderriest 1980; Barden & Wade 1988) use a packed fiber bundle placed in the focal plane in order to direct light to the spectrograph. A modification of this design combine a lenslet array with the fibers (for example, used in PMAS LArr mode), improving the fill factor. Pure fiber bundles or lenslet+fiber designs are used in several large IFS galaxy surveys such as CALIFA, using the PMAS instrument (Roth et al. 2005) in PPaK (Verheijen et al. 2004) mode, mounted on the 3.5 m telescope at the Calar Alto observatory, SAMI survey (Croom et al. 2012) using the SAMI instrument on the Anglo-Australian Telescope, MaNGA (Bundy et al. 2015; Drory et al. 2015) which uses the the Sloan 2.5 m telescope at Apache Point Observatory.

1.4.2 IFS studies of galaxy kinematics and dynamics

Despite being a relatively new method of spectroscopy, especially in survey mode, IFS has already yielded groundbreaking results in galaxy kinematics and dynamics. The SAURON instrument and the eponymous survey (Bacon et al. 2001; de Zeeuw et al. 2002) measured the kinematics of a representative sample of 72 local early-type galaxies (ellipticals, S0s and Sa bulges). The flagship result of the SAURON survey, demonstrating the power of IFS observation, is a kinematic classification scheme for early-type galaxies (Emsellem et al. 2007), different from the classical morphology-based classification. They introduce a new parameter λ_R, which is a luminosity-weighted average over the 2D kinematics, to estimate the projected specific stellar angular momentum and quantify the degree of rotational support a galaxy has. The early-type galaxies were found to fall into two groups: 'fast' rotators, having $\lambda_R > 0.1$, which are flattened, fainter, axisymmetric systems showing ordered stellar rotation, and the 'slow' rotators, which are massive triaxial systems with little or no net rotation, except at the central kinematically decoupled cores. The slow rotators, on average brighter than the fast rotators and classified as ellipticals from photometry, are thought to have been formed via gas-poor mergers. Further studies, such combined analysis of the $V/\sigma, \epsilon$ diagram and dynamical axisymmetric Schwarzschild modelling of 24 SAURON galaxies (Cappellari et al. 2006, 2007) find that the main physical difference between slow and fast rotators is their physical shape, as the slow rotators are triaxial systems.

Motivated by these results, ATLAS^{3D} survey (Cappellari et al. 2011a), using a volume complete sample of 260 nearby early-type galaxies, extended SAURON investigation of galaxy kinematics and dynamics. Emsellem et al. (2011) revisited the kinematic galaxy classification scheme, suggesting a better classification scheme based on λ_R and apparent ellipticity ϵ, while Cappellari et al. (2011b) investigated the kinematic density-morphology relation for the first time. Kinematic maps of simulated galaxies connected their kinematic properties to their cosmological formation histories, reinforcing the importance of mergers in galaxy angular momentum evolution and demonstrating how slow rotators could have formed via minor gas-poor mergers (Naab et al. 2014). SAURON's study of intrinsic shapes of early type galaxies was extended by Weijmans et al. (2014), who showed that fast rotators are indeed predominantly axisymmetric, whereas slow rotators are slightly triaxial.

In parallel, the DiskMass survey (Bershady et al. 2010) investigated the stellar kinematics of nearby spiral galaxies. Using PMAS (Roth et al. 2005) in conjunction

with SparsePaK (Bershady et al. 2004) and PPaK (Verheijen et al. 2004) instruments, with 1 arcmin field-of-view, it obtained gas and stellar kinematics for a sample of 30 nearly face-on spiral galaxies.

The main question DiskMass has sought to answer was whether the spiral galaxy disks are submaximal. The degeneracy between the disk and dark matter halo means that an observed rotation curve cannot be decomposed into contributions from dark matter halo and the baryonic components, because the dark matter density profile cannot be constrained without an independent knowledge of the mass-to-light ratio of the stellar disk. The maximum-disk hypothesis (van Albada & Sancisi 1986) tried to evade this degeneracy by assuming maximum possible contribution from the baryons, i.e. increasing the mass-to-light ratio until the inner parts of the observed rotation curve could be fit by the contribution from the stars and gas. However, this had been an untested assumption which only allowed setting the upper limit to the baryonic contribution, but did not reliably constrain the dark matter density profiles. DiskMass measured vertical velocity dispersion component of the stars, computing the dynamical mass surface densities and showing that the disks are submaximal (Martinsson et al. 2013).

1.4.3 The CALIFA survey

The CALIFA survey (Sánchez et al. 2012; Walcher et al. 2014; García-Benito et al. 2015; Sánchez et al. 2016) was designed to extend the existing IFU surveys by combining the benefits of a large PPaK field-of-view (74" × 64") and unbiased, statistically significant sample of galaxies.

The PPaK IFU fibers form a hexagonal pattern, with additional sky fibers placed outside it. CALIFA observations are made in two overlapping wavelength ranges: the red setup (V500, 3745-7500 Å) with lower resolution R ≈ 850, and the blue setup (V1200, R ≈ 1650, 3400-4840 Å). CALIFA mother sample and Extension sample observations and data reduction pipeline are described in greater detail in Sánchez et al. (2012, 2016); Husemann et al. (2013).

The main CALIFA sample (Walcher et al. 2014; Sánchez et al. 2016) consists of 937 galaxies selected from SDSS DR7 and satisfying the following constraints:

- the isophotal angular diameter limit: 45" $< isoA_r <$ 79.2"
- the redshift limit: $0.005 < z < 0.03$
- the Galactic latitude $|b| > 20°$
- the SDSS Petrosian r-band magnitude $\mathrm{petroMag}_r < 20$ mag
- $\delta > 7°$

The position and flux limits were set in order to satisfy various observational constraints. The diameter limit was chosen in order to use the detector area efficiently. The lower redshift limit was explicitly chosen in order to avoid having a sample dominated by dwarf galaxies, therefore introducing a lower 95 % completeness limit in luminosity (-19 $> M_r$) or stellar mass ($10^{9.7}$ $M_\odot$). The upper redshift limit was applied in order to keep the relevant spectroscopic features within the observed wavelength interval. The cosmological volume accessible to the CALIFA survey was then of the order of 10^6

Mpc^3, setting the upper limits of -23.1 mag in luminosity and $10^{11.4}$ $M_\odot$ in stellar mass due to the rare nature of such galaxies.

In Walcher et al. (2014) we showed that it is possible to derive V_{max} values for the galaxies of CALIFA mother sample, which enable calculating statistical galaxy distribution functions. The CALIFA sample is a unique IFS survey in this regard.

CALIFA studies of galaxy kinematics and dynamics The CALIFA gas and stellar kinematics data and extraction procedures are presented in García-Lorenzo et al. (2015) and Falcón-Barroso et al. (2016). A number of studies has since been done with these maps, investigating the kinematics of interacting galaxies (Barrera-Ballesteros et al. 2015), the pattern speed of barred galaxies (Aguerri et al. 2015), non-circular kinematic flows (Holmes et al. 2015), analysis of the origin of S0 galaxies (van de Ven et al., in prep) and Querejeta et al. (2015).

A CALIFA perspective on angular momentum, a study of galaxies of all morphological types, was first introduced in Falcón-Barroso et al. (2015a). In short, they show the distribution of CALIFA galaxies on the λ_{Re} (λ inside the effective radius) - ϵ plane, demonstrating that Sb galaxies tend to have the highest λ_R values. In contrast, several Sc and Sd galaxies have very low $\lambda_R e$ values well inside the slow-rotator range. Another result of the study is the high dark-matter fraction of the low mass spirals, found by comparing the dynamical masses determined by constructing axisymmetric Jeans models with stellar masses obtained by stellar population modells. They find that even within one effective radius the dark matter fraction is high for low mass Sc-Sd galaxies, which is supported by their low λ_{Re} values.

A similar approach was used in Lyubenova et al. (2016), who used dynamical and stellar mass-to-light ratios are used in order to constrain the shape of the IMF, finding that a double power law IMF with a varying high-mass slope is the preferred model for the majority of galaxies. Other ongoing work includes constructing an orbit-based Hubble sequence, dynamical decomposition of galaxies of all morphological types, dark matter halo studies of compact early type galaxies (Yıldırım et al. 2016, using the CALIFA extension sample).

1.4.4 CALIFA sample characterisation

Part of this analysis was published as part of Walcher et al. (2014) and presented as a poster in the 9th Potsdam Thinkshop 2012: Galaxy surveys using Integral Field Spectroscopy: Achievements and Opportunities.

Motivation

It was noted long ago (Opik 1922; Wyatt & Brown 1955)) that diameter-limited disk galaxy surveys could be susceptible to selection effects due to inclination (related to disk galaxies axis ratio as $cos(i) = b/a$). A highly-inclined disk galaxy would have an apparently larger angular diameter than an otherwise identical face-on galaxy, because the same (barring dust influence) flux would be confined within a smaller projected area.

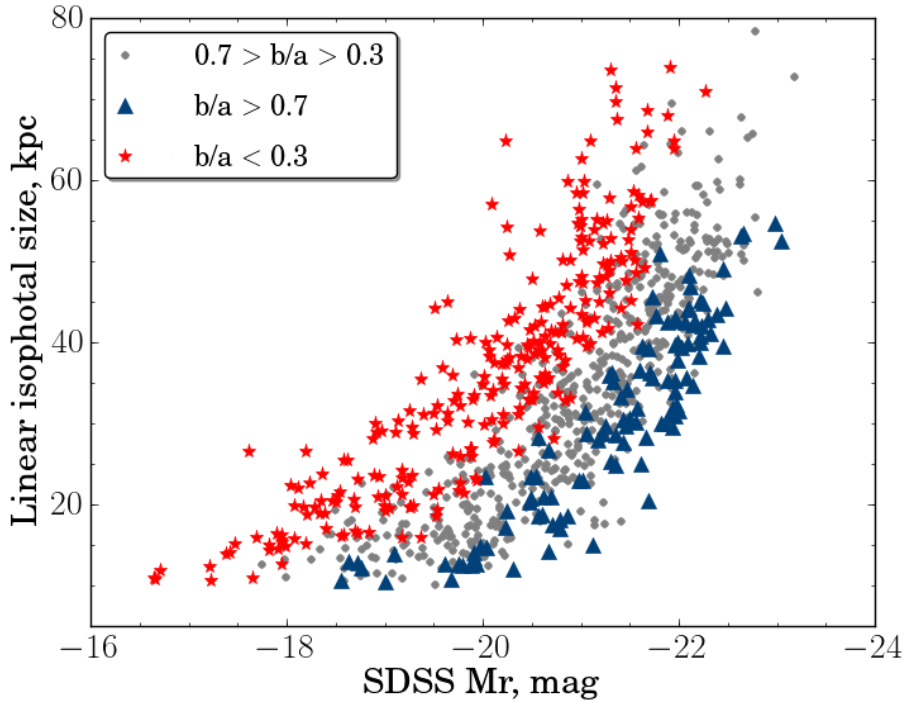

Figure 1.1: Size-magnitude relation, colour-coded for different b/a bins.

Before we can evaluate the statistical completeness of the CALIFA sample and calculate the volume corrections, an analysis of the axis ratio distribution of the galaxies in the CALIFA sample is necessary.

CALIFA sample selection

937 galaxies for the CALIFA mother sample were selected from the SDSS DR7 photometric objects database, supplanting the missing redshift data with NED information. The survey is primarily redshift- and isophotal diameter-limited. The diameter cut (45" < D < 80") used $isoA_r$, the SDSS equivalent of isophotal radius D25, as the diameter measure.

Size-luminosity relation

The physical size-luminosity relation for the CALIFA sample illustrates the possible effects of b/a on the overall distribution of galaxy parameters in a diameter-selected sample. Galaxies of the same luminosity appear to have larger isophotal (and physical) radii if their axis ratio is smaller.

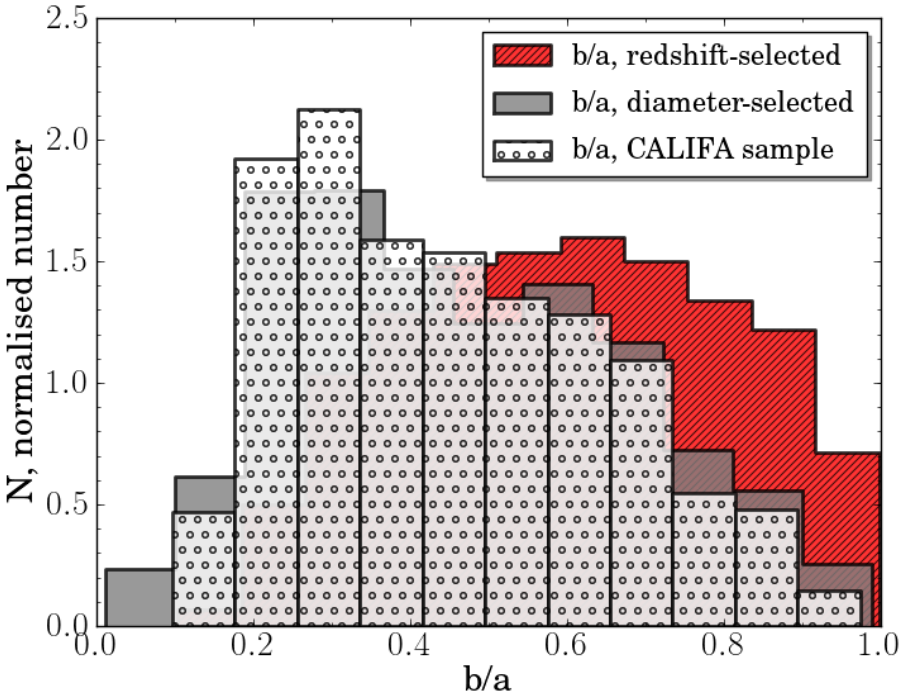

Figure 1.2: Axis ratio distributions of the three galaxy samples.

Comparison with the underlying SDSS sample

We checked whether the CALIFA mother sample's b/a distribution is similar to b/a distribution of two related samples selected from the SDSS DR7 catalogue. We selected a redshift-limited sample, with the same redshift cuts and a minimum isophotal diameter limit (> 8", to avoid including unresolved galaxies). The second sample was diameter-limited, with the same angular diameter cuts as the CALIFA mother sample.

The b/a distributions of diameter-selected samples and the redshift-selected sample demonstrate that diameter cuts can lead to a higher ratio of low b/a galaxies, however, further analysis would be needed to clarify the extent of this effect. The CALIFA sample consists of predominantly late-type galaxies (787 out of 939, visual classification by the CALIFA collaboration), whereas the morphological type ratio in the SDSS database can be significantly different.

Conclusions

Volume correction is a process of reconstructing properties distribution and statistics of a volume-complete sample from a flux- or diameter-limited one. It usually involves recalculating the property distributions weighting each object by the inverse of the volume within the survey limits where it can be observed. In order to fully avoid possible bias described above, volume correction weighting functions for intrinsic properties of the sample galaxies, such as physical size distribution or luminosity function, should have

inclination-dependent terms accounting for the fact that accessible volumes for identical disk galaxies with different inclinations are not the same. Projected surface brightness increases with inclination, leading to apparently larger isophotal sizes, whereas dust extinction has the opposite effect, affecting the absolute magnitude and colour distributions. Marginalising over the inclination distribution can lead to selection effects: for example, there might be an excess of low b/a galaxies near the lower diameter cut, and a lack of such systems near the higher limit. This is analysed in more detail in Walcher et al. (2014) and shown to be relatively unimportant for the CALIFA survey.

1.5 Outline of the thesis

In this work we use integral field spectroscopy in order to gain insight into two angular momentum-related distribution functions of nearby galaxies.

After this introduction, we devote the second chapter of this thesis to the CALIFA Tully-Fisher relation (Tully & Fisher 1977), obtaining a volume-complete 2D distribution of SDSS *r*-band absolute luminosity and circular rotation velocity at 80% light radius.

The third chapter investigates the circular velocity function of galaxies. We complement CALIFA measurements with HIPASS HI velocity function in order to obtain a circular velocity function that is representative between $60 < v_{\rm circ} < 320$ km s^{-1} for all morphological types relevant at a given velocity. We also compare our velocity function with cosmological simulations and find that while dark matter-only simulations fail to reproduce the observed VF, while baryonic simulations also show a strong mismatch.

The fourth chapter contains other work: a feasibility study of simultaneous kinematic modelling of SAMI gas velocity fields and ALFALFA HI linewidths with a goal of precise angular momentum determination. Mathematical and computational methods follow in the appendices.

Chapter 2

The space density distribution of galaxies in the absolute magnitude - rotation velocity plane

A version of this chapter was published in 2016 as "Space density distribution of galaxies in the absolute magnitude - rotation velocity plane: a volume-complete Tully-Fisher relation from CALIFA stellar kinematics", S. Bekeraitė, C.J. Walcher, J. Falcón-Barroso, Astronomy & Astrophysics, Volume 593, id.A114, 16 pp.

2.1 Abstract

We measured the distribution in absolute magnitude - circular velocity space for a well-defined sample of 199 rotating galaxies of the Calar Alto Legacy Integral Field Area Survey (CALIFA) using their stellar kinematics. Our aim in this analysis is to avoid subjective selection criteria and to take volume and large-scale structure factors into account. Using stellar velocity fields instead of gas emission line kinematics allows including rapidly rotating early-type galaxies. Our initial sample contains 277 galaxies with available stellar velocity fields and growth curve r-band photometry. After rejecting 51 velocity fields that could not be modelled because of the low number of bins, foreground contamination, or significant interaction, we performed Markov chain Monte Carlo modelling of the velocity fields, from which we obtained the rotation curve and kinematic parameters and their realistic uncertainties. We performed an extinction correction and calculated the circular velocity $v_{\rm circ}$ accounting for the pressure support of a given galaxy. The resulting galaxy distribution on the M_r - $v_{\rm circ}$ plane was then modelled as a mixture of two distinct populations, allowing robust and reproducible rejection of outliers, a significant fraction of which are slow rotators. The selection effects are understood well enough that we were able to correct for the incompleteness of the sample. The 199 galaxies were weighted by volume and large-scale structure factors, which enabled us to fit a volume-corrected Tully-Fisher relation (TFR). More importantly, we also provide the volume-corrected distribution of galaxies in the M_r - $v_{\rm circ}$ plane, which can be compared with cosmological simulations. The joint distribution of the luminosity and circular velocity space densities, representative over the range of

-20 > M_r > -22 mag, can place more stringent constraints on the galaxy formation and evolution scenarios than linear TFR fit parameters or the luminosity function alone.

2.2 Introduction

2.2.1 The Tully-Fisher relation

The Tully-Fisher relation (TFR, Tully & Fisher 1977) links two intrinsic properties of rotationally supported galaxies: their circular rotation velocities, and their luminosities. Stated in physical terms, this relation indicates a close relation between the total dynamical mass and the stellar mass (or the total baryonic content, McGaugh et al. 2000) of the galaxies.

Circular velocities and luminosities of galaxies have long been used to estimate extragalactic distances (see Opik 1922, for the first use), also see Roberts (1969); Bottinelli (1971); Balkowski et al. (1974) and Shostak (1975) for early analyses of scaling relations of spiral galaxies.

The low intrinsic scatter of the TFR cannot be explained by initial conditions (Eisenstein & Loeb 1996), which implies that the subsequent evolutionary processes were crucial in determining the shape of the relation. The fact that the TFR exists is thought to be a natural outcome of hierarchical structure assembly (Steinmetz & Navarro 1999).

Although the TFR has primarily been envisaged and successfully used as a tool to determine extragalactic distances (Tully & Fisher 1977), it also offers fundamental insights into the processes of disk assembly and evolution. We summarize the many uses of TFR in the following paragraphs.

The TFR in its initial form and in its many variants (relations between different measures of rotational velocity and the stellar mass, total baryonic mass, absolute magnitude in different passbands) has been extensively employed as a constraint on galaxy formation and evolution models (Koda et al. 2000; Croton et al. 2006; Dutton & van den Bosch 2009; Dutton et al. 2011; Tonini et al. 2011; McCarthy et al. 2012; Vogelsberger et al. 2013). It also provided independent constraints on cosmological parameters (Eisenstein & Loeb 1996; van den Bosch 2000; Masters et al. 2006), has been used to test the predictions of ΛCDM (Blanton et al. 2008), and to characterise the properties of dark matter haloes such as their concentration (Dutton et al. 2011) and response to galaxy formation (Dutton & van den Bosch 2009; Chan et al. 2015). The TFR has also been used to place constraints on virial properties of barred and unbarred galaxies (Courteau et al. 2003), on disk submaximality (Courteau & Rix 1999; Courteau & Dutton 2015), to investigate the origin of S0 galaxies (Neistein et al. 1999; Williams et al. 2009; Tonini et al. 2011), test the universality of the initial mass function (Bell & de Jong 2001; Dutton et al. 2011), and to infer the galaxy velocity function (Gonzalez et al. 2000).

In addition, TFR measurements at higher redshifts provided insights into the mode of gas accretion at $z \approx 2.2$ (Cresci et al. 2009), the stellar-to-dynamical mass ratio at $z \approx 3$ (Gnerucci et al. 2011), disk assembly timescales (Miller et al. 2012), the evolution of bulgeless galaxies (Miller et al. 2013), the "downsizing" effect (Böhm & Ziegler 2007), and the luminosity evolution of rotating disks (Ziegler et al. 2002; Puech

et al. 2008; Miller et al. 2011).

Reproducing the observed redshift evolution, slope, offset, and intrinsic scatter of the TFRs is a standard test of cosmological simulations. It has been a long-standing problem of cosmological simulations (Steinmetz & Navarro 1999; van den Bosch 2000; Koda et al. 2000; Cole et al. 2000; Eke et al. 2001; Croton et al. 2006; Courteau et al. 2007; Dutton et al. 2011), but this problem has been significantly remedied by a combination of more sophisticated feedback implementations, prescriptions for dark halo response, and the increased accuracy of cosmological parameters.

Several studies have described the convergence on reproducing the observed TFR: Dutton et al. (2007); Governato et al. (2007); Trujillo-Gomez et al. (2011); Tonini et al. (2011); McCarthy et al. (2012); Vogelsberger et al. (2014a). Semi-analytical models by Tonini et al. (2011) reproduced the TFR at higher redshifts, but yield too bright values at z=0, probably as a result of the uncertainties in star formation histories. Hydrodynamical zoom-in re-simulations by McCarthy et al. (2012) reproduced the TFR for galaxies with $\log(M_*) < 10.7$. The authors claimed that the turn-off at the higher mass end is due to the lack of AGN feedback prescription. Governato et al. (2007) employed N-body SPH simulations with supernova feedback to produce disk galaxies that lie on both the *I* band and the baryonic TFR. Trujillo-Gomez et al. (2011) used Bolshoi dark-matter-only simulations and abundance matching to demonstrate that the luminosity-velocity relation and the baryonic TFR match the observed ones. The Illustris project implements a sophisticated feedback model that includes both stellar and AGN feedback, reporting slightly too high circular velocities in the $M_* - v_{circ}$ relation (Vogelsberger et al. 2014a). The goal of this study is to provide a measurement of the TFR and $M_r - v_{circ}$ distribution that is best suited for a comparison with these theoretical predictions.

Given the large body of literature on the TFR, we need to justify revisiting the relation. The Calar Alto Legacy Integral Field Area (CALIFA) provides three main reasons, two related to the observational data type at hand (integral field spectroscopy – IFS), and the last one tied to the available sample properties.

First, optical long-slit observations have traditionally been the observational basis for the TFR analysis. Long-slit observations have the drawback of not being able to view the entire velocity field of a galaxy and thus are prone to being affected by non-circular velocity field distortions. IFS data allow using the full velocity information available to correct for non-axisymmetric velocity field features, characterise the specific angular momentum of galaxies, and distinguish between disturbed velocity fields, pristine disks, and slow rotators. The possibility of performing the sample selection using kinematic properties of galaxies is more relevant to the TFR than visual morphological classification. This has strikingly been confirmed by Flores et al. (2006). These authors showed that the very large scatter in the intermediate-redshift TFR, previously reported from long- or multi-slit spectroscopic observations, is a result of modelling a large portion (≈65%) of galaxies with anomalous kinematics. A similar point has been made by Andersen & Bershady (2003), who demonstrated that galaxies with large kinematic and photometric asymmetries in their velocity fields tend to be offset from the TFR. Using 2D velocity fields also prevents slit misalignment with the semi-major axis of the galaxy, even if such differences are not expected be a major problem in the TFR context (Amram et al. 1994; Courteau 1997; Giovanelli et al. 1997; Barrera-Ballesteros

et al. 2014).

In addition, the observed line-of-sight rotation velocities must be de-projected to obtain the true circular rotation velocities. However, inclination is a notoriously difficult parameter to measure and is frequently the largest source of uncertainty in circular velocity measurement (Schommer et al. 1993; Garrido et al. 2004; Giovanelli et al. 1997; Obreschkow & Meyer 2013). In most of the Tully-Fisher studies, inclination estimates are obtained from the variously defined apparent axis ratios b/a in the following way (Hubble 1926):

$$cos(i)^2 = \frac{(\frac{b}{a})^2 - q^2}{1 - q^2}. \tag{2.1}$$

Here q is the intrinsic axis ratio of the galaxy, which is different for different galaxy morphological types (e.g. Rodríguez & Padilla 2013), but a mean value of $q = 0.2$ is frequently used (Tully & Pierce 2000). However, there are several shortcomings of this method. It frequently overestimates the inclination for face-on galaxies because any irregularity (such as the spiral arms, bars, and disk asymmetries) at the outskirts of a galaxy will make the b/a seem higher (e.g. Maller et al. 2009). For galaxies that are observed close to edge-on, photometric inclination estimates suffer from uncertainty in the intrinsic axis ratio q, which depends on the Hubble type of the galaxy and evolves through cosmic time (Obreschkow & Meyer 2013). However, this is not thought to be very significant in the context of TFR (Courteau 1997; Hall et al. 2012).

We are able to circumvent these difficulties with assumptions made for photometric inclination estimates and directly model the velocity fields as rotating disks, obtaining kinematic inclination and position angles as free parameters. These methods were first used a few decades ago by radio (Rogstad et al. 1976; Bosma 1978) and Fabry-Perot interferometry observers (Marcelin & Athanassoula 1982; Bland et al. 1987; Nicholson et al. 1992; Schommer et al. 1993; Amram et al. 1994).

To our knowledge, the first analysis of TFR using 2D IFS velocity fields was reported by Courteau et al. (2003) for of barred and unbarred disk galaxies. The authors used the SparsePak IFU (Bershady et al. 2004) to test whether the rotation velocities measured using long-slit spectroscopy are reliable. Andersen & Bershady (2003) derived a face-on Tully-Fisher relation based on 24 Hα velocity fields of low-inclination (16°- 41°) galaxies. They showed that kinematic inclination estimates are sufficiently accurate down to $\approx$15° and that this approach allows avoiding systematic and random errors arising from use of photometric axis ratio-based inclination estimates. For example, Schommer et al. (1993) found that photometric inclination estimates are systematically larger than inclinations derived from kinematics for galaxies with inclinations of up to 50°. As shown in this paper, by combining the photometric and kinematic data, we can model the velocity fields consistently and obtain the full distributions of parameter uncertainties for inclinations, position angles, and kinematic parameters, including the estimated rotation velocity.

Although several other IFS-based Tully-Fisher studies exist, they tend to focus on higher redshifts and have small sample sizes, aiming to investigate the dynamical state of high-redshift galaxies, assembly times of rotating disks, and morphological evolution (Swinbank et al. 2006; Puech et al. 2008; Cresci et al. 2009; Gnerucci et al. 2011). Similarly, Green et al. (2014) used the TFR measured from Hα velocity fields of local gas-rich galaxies to gain insight into their high-redshift analogues. Recently, Di

Teodoro et al. (2016) used a sample of 18 z 1 KMOS galaxies to demonstrate that the TFR obtained from Hα emission is identical to the present one.

Therefore, the third major reason to revisit the TFR is that the CALIFA survey has better-defined sample selection criteria than earlier published work. In virtually all past TFR studies, the authors aimed for a clean sample, meaning a set of late (usually Sa or later) morphological type galaxies with ordered circular motions (e.g. Courteau 1996; Tully & Pierce 2000; McGaugh et al. 2000). The goal of most of these studies was to estimate or calibrate a template Tully-Fisher relation that would be best suited for distance measurements. Many methods to account for selection effects in TFR samples have been developed, such as employing galaxy cluster observations to obtain volume-complete samples, using the so-called inverse fitting methods, performing corrections based on morphology and extinction estimates, also attempting to account for varying distances to a cluster centre, implicit sample incompleteness, and many other possible sources of bias (see Giovanelli et al. (1997); Tully & Pierce (2000); Verheijen (2001); Masters et al. (2006); Saintonge & Spekkens (2011) and references therein for in-depth discussions of these methods and their shortcomings). While the above approaches are justified when the goal is to obtain a tight linear distribution with the least possible amount of scatter, our objective is different. We aim to use data-driven modelling to obtain a volume-corrected 2D distribution of rotationally supported galaxies. While such a distribution would not be directly useful for distance measurements (although we provide the parameters of a standard linear fit), it could place more stringent constraints on galaxy evolution models than the standard TFR or luminosity and velocity functions separately.

A sample selected for this purpose needs to span the widest possible range of morphologies (Verheijen 2001). The wish to include galaxies of all types and be able to perform consistent volume and large-scale structure corrections has compelled us to use the stellar velocity fields in this study. Stellar velocity fields have rarely been used for TFR measurements, mainly because of their lower signal-to-noise ratio (S/N) level. Emission lines are more easily detected in spectroscopic data, meaning that velocity fields based on emission line kinematics will extend farther out in the disk and have better spatial resolution. However, the main advantage of stellar velocity fields is that they can be obtained for galaxies without significant gas emission lines, that is, for early-type galaxies. A significant percentage of early type galaxies follows the TFR: for example, Krajnović et al. (2008) stated that about 80% of early-type galaxies and S0s have a rotating-disk component. Similarly, Emsellem et al. (2011) showed that the majority of early type galaxies in the ATLAS3D sample are fast rotators, while Davis et al. (2011) demonstrated that early-type galaxies lie on the CO Tully-Fisher relation, albeit likely offset from the one derived for spirals.

CALIFA is the first IFS survey to include many late-type galaxies as well, to have a large and statistically well-defined sample, and a sufficiently large field of view, all of which is necessary for this type of analysis.

2.3 Data, sample selection, and characterisation

2.3.1 CALIFA Survey

CALIFA (Sánchez et al. 2012; Walcher et al. 2014, hereafter W14) is a legacy IFS survey of 600 nearby galaxies. Observations use the PMAS instrument (Roth et al. 2005) in PPaK (Verheijen et al. 2004) mode, mounted on the 3.5 m telescope at the Calar Alto observatory. The sample of galaxies that are observed with CALIFA is drawn from a larger pool of galaxies, selected from the SDSS DR7 survey, and termed the mother sample (MS). The MS is primarily diameter-limited and aimed at using the detector area efficiently. The CALIFA selection criteria are described in W14 in more detail. One salient feature of the CALIFA MS is that its selection criteria are well understood, providing us with a representative sample of galaxies that can be corrected for selection effects down to an absolute r-band magnitude of -19 mag. By adopting a probabilistic approach to outlier rejection, we show in this paper that we can keep a similar property of the sample even as we restrict it to conform to more stringent criteria.

The CALIFA data have been reduced using the CALIFA pipeline, and we refer to Sánchez et al. (2012); Husemann et al. (2013); García-Benito et al. (2015) for all the details. The result of the data reduction is two spectral cubes of the target galaxy, one in the V1200 grating and one in the V500 grating, which can be used to extract kinematic information. V1200 grating has been used here because this setup allowed measuring the velocity dispersion down to ≈50 km/s.

Kinematic information of the stars was extracted from CALIFA datacubes using the pPXF fitting procedure (Cappellari & Emsellem 2004) and INDO-US (Valdes et al. 2004) spectral templates library. Bad pixels, foreground contamination, low-quality spaxels with S/N < 3, emission line regions in the spectra and regions outside 3750–4650 Å range (for the V1200 setup) were excluded from the fit. Spatial Voronoi binning (Cappellari & Copin 2003) was applied to ensure a constant S/N = 20 in velocity dispersion, and it led to variable size bins with diameters ranging from 0.1 kpc to 21 kpc in linear size. On average, the galaxies have 131 useful kinematic data points, with the lowest number being 1 (galaxies with too few Voronoi bins were excluded from further analysis, as described in the next paragraphs) and the highest number of bins being 760. The velocity and velocity dispersion values for each bin and the associated uncertainties were derived using 100 MCMC realisations of the fit. We refer to the first paper of the CALIFA stellar kinematics series (Falcón-Barroso et al., submitted) where the kinematic map extraction is described in full detail.

We started with the sample of galaxies observed by CALIFA until October 2013. This corresponded to 277 objects with derived stellar velocity fields. We term this the observed sample. Out of these, 51 were rejected at the beginning as not usable. A significant fraction of the rejected galaxies, 17, had too few bins ($N_{bins} < 6$) to even try to reliably constrain the rotation curves with the stellar velocity fields. In addition, we excluded 31 galaxies whose velocity fields could not provide a physical model. This included several heavily masked mergers, 4 galaxies where foreground objects obscured a significant part of the velocity map, 2 galaxies with significant dust lanes that obscured velocity fields, and the 5 galaxies that were excluded because they are unsuitable for the volume-correction procedure described below. We emphasize that the

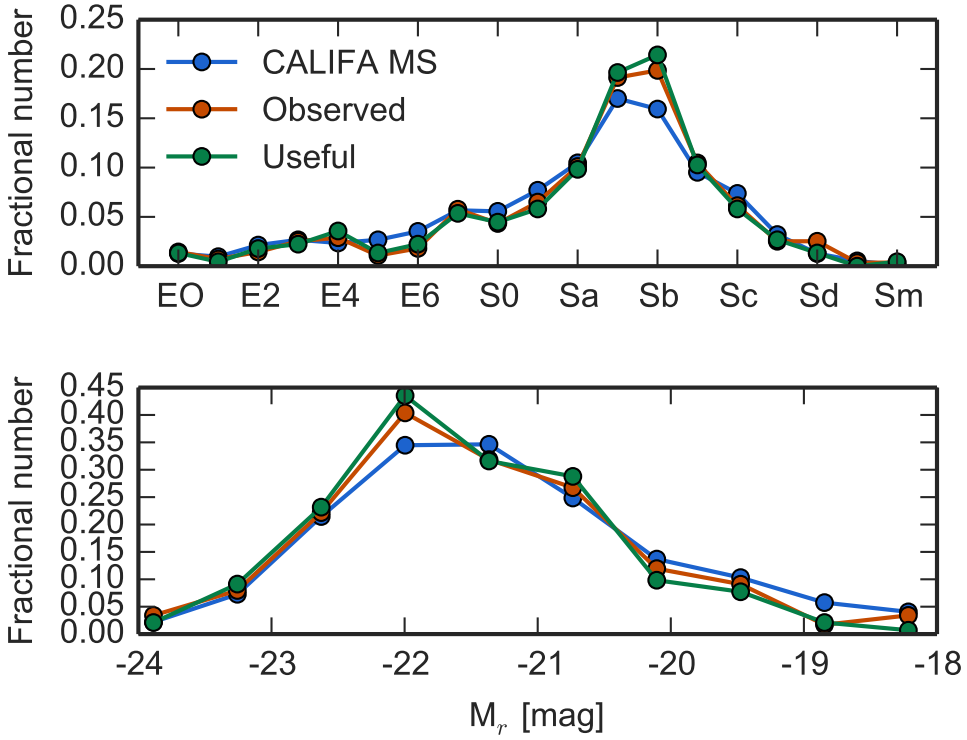

Figure 2.1: Normalised histograms of SDSS Petrosian M_r and morphological types of the CALIFA mother sample, observed sample (as of October 2013), and the useful subsample that we included in our analysis.

rejection here was not directly related to the internal properties of the galaxies that were relevant to this analysis (absolute magnitude, stellar mass, and rotation velocity), but to problematic observational data that precluded making realistic models. The resulting sample contains 226 useful velocity fields, and we refer to it as the useful sample in the following sections.

Figure 2.1 shows the normalised SDSS Petrosian absolute magnitude M_r and morphological type histograms for the CALIFA mother sample, the observed sample, and the useful sample. As shown in the top panel, the observed sample contains slightly more Sa-Sb type galaxies than the CALIFA mother sample. Even though the observing selection should be random, observing constraints and spatial variation within the sample volume might have introduced this discrepancy.

The lower panel of Fig. 2.1 shows normalised histograms of M_r. The observed and especially the useful sample lack the least luminous galaxies that are included in the mother sample. This effect in the useful sample is exacerbated because we were more likely to reject intrinsically fainter, later-type galaxies at this step, whihc were more likely to have fewer Voronoi bins. This must affect the outcome of the volume correction we perform at later steps.

2.3.2 Volume corrections

The CALIFA sample is limited by two main selection criteria, including all galaxies within the SDSS DR7 footprint that have (i) redshifts within $0.005 < z < 0.03$, and (ii) isophotal angular extents within $40 < \theta < 79$ arcsec. This construction principle allows us to perform volume corrections using the $V_{\rm max}$ method (Schmidt 1968) in much the same way as with a flux-limited sample (see W14 for details). While the sample as a whole is not volume complete, each galaxy can be assigned a well-defined accessible survey volume $V_{\rm max}$ over which it would be included given its properties and given the sample selection criteria.

It is important to realise that the selection by apparent diameter in CALIFA does by no means introduce a bias in terms of linear sizes of the galaxies in the sample because of the broad redshift range. Within the completeness range of the sample ($-19 > M_r > -23.1$; see W14), low-luminosity and small galaxies match the angular diameter criterion close to the low-redshift limit, while more luminous and larger galaxies occupy higher redshifts. By adding the contributions $1/V_{\rm max}$ of all galaxies in suitable bins, we can calculate a volume-corrected estimate of a distribution function of the galaxy population. W14 demonstrated that the galaxy luminosity function as well as the size distribution function estimated in this way from the CALIFA mother sample are in excellent agreement with results from SDSS.

Another potential source of bias is related not to the sample selection process, but to the properties of the particular cosmological volume a given survey, is probing. The CALIFA survey samples two nearby clusters (Virgo and Coma) as well as the underdensities in between, resulting in significant radial number density variations. W14 showed how these radial variations can be quantified and absorbed into effective volume correction factors. All volume-corrected quantities shown in this paper use these effective $V_{\rm max}$ values.

In this paper we also exploit the concept of volume corrections for the Tully-Fisher relation. Since our useful sample is much smaller than the CALIFA MS, the volume-correction factors need to be adjusted to reflect the size of the subsample. As long as the sample is a random subset of the mother sample, it is sufficient to reduce $V_{\rm max}$ by the sampling rate; this concept was used in the first two CALIFA data releases to verify that the releases subsets (of 100 and 200 galaxies, respectively) are consistent in their statistical distribution properties with the mother sample and with the galaxy population as a whole (Husemann et al. 2013; García-Benito et al. 2015). In Fig.2.2 we used the same approach to compare the galaxy luminosity function constructed from our useful sample with the results from the CALIFA MS and from SDSS. The agreement is excellent for absolute magnitudes $M_r < -20$ mag, but there seem to be too few galaxies in the bins fainter than -20 mag for the useful sample. As mentioned above, this is probably due to our rejection of some late-type galaxies from the kinematic analysis because they have an insufficient number of Voronoi elements. Apart from this caveat, we conclude that our sample can be seen as volume-representative for the local galaxy population, at least for absolute magnitudes $-22 < M_r < -20$.

Five more galaxies were excluded from further analysis: NGC 4676B and NGC5947 had been added to the CALIFA MS by hand (see W14) and have no associated $V_{\rm max}$ values, while for NGC 7625, NGC 1056, and NGC 3057 these values are dispropor-

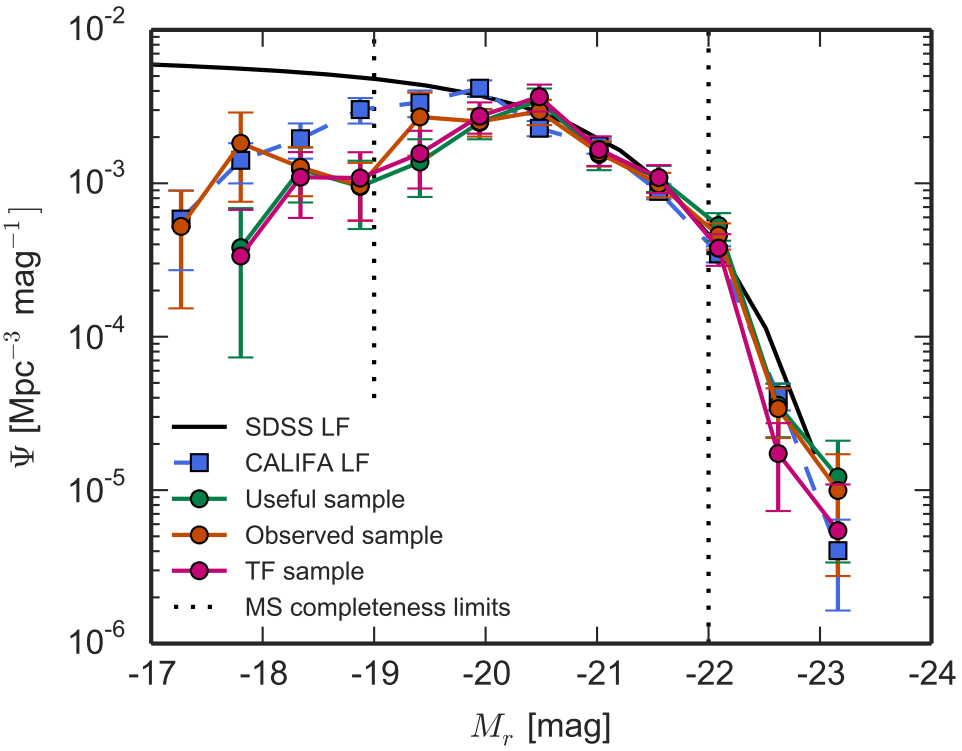

Figure 2.2: Luminosity functions of the CALIFA mother sample (MS), the observed sample, the useful sample (see text), and the final Tully-Fisher sample defined in Sect. 2.6.2. The dotted lines denote the MS completeness limits calculated in W14. SDSS DR7 Petrosian *r*-band magnitudes were used for comparison with the SDSS luminosity function. The effects of outlier rejection steps are evident, especially for the more numerous low-luminosity galaxies with higher $1/V_{max}$ weights.

tionally low ($< 10^4$ Mpc^3). Since the $1/V_{max}$ weights are then correspondingly large, these few galaxies would totally dominate any $1/V_{max}$-weighted fit to the Tully-Fisher relation. We note that this is an inherent weakness of the V_{max} method. While more sophisticated approaches are conceivable that are more robust against such statistical fluctuations, we simply decided to remove these three objects. The effects of using or omitting $1/V_{max}$ weights when fitting the TFR are shown in Sect. 2.7.

2.4 Luminosity data

2.4.1 Observed magnitudes

We used the *r*-band growth curve photometry measurements described in W14. The uncertainties account for the combination of the contributions from the dark current and read noise, Poissonian sky counts error, uncertainties due to sky subtraction, and an estimate of uncertainties arising from masked foreground objects. The formal errors

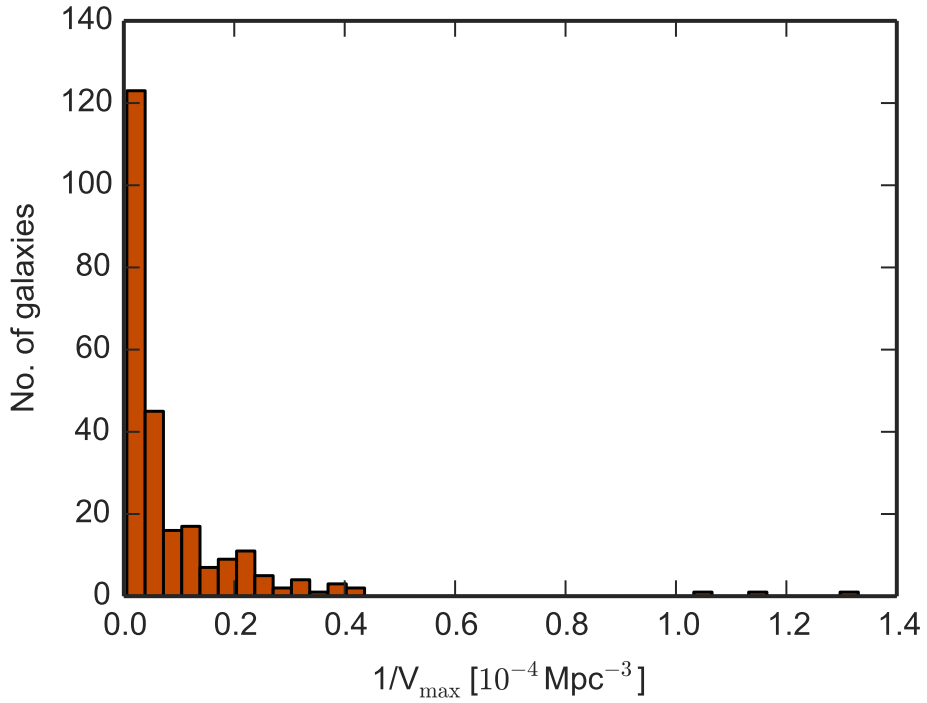

Figure 2.3: Volume and radial-density weight factor $1/V_{\rm max}$ histogram. The three outliers with $1/V_{\rm max} > 0.0001$ were excluded from further analysis.

due to shot noise contribute only little to the error budget because of the large apparent sizes of our galaxies in the SDSS images. The magnitudes were corrected for Galactic extinction using SDSS pipeline values.

Absolute magnitudes were calculated using the prescriptions presented in W14. In short, the redshifts were corrected for Virgo-centric and Shapley and Great-Attractor infall motions using the model by Mould et al. (2000). K-corrections were determined from spectral energy distributions as described in W14 and Walcher et al. (2008). The distance uncertainties were derived from group velocity dispersions obtained by the collaboration in W14 and combined with the photometric uncertainties when calculating the absolute magnitude uncertainties.

2.4.2 Corrections for intrinsic absorption

The absolute magnitudes need to be corrected for internal extinction, which depends on the inclination, bandpass, and morphology in a non-trivial way. We adopted the methods described in Wild et al. (2011a,b), which provide dust attenuation as a function of the photometric axis ratio b/a, the specific star formation rate, and the presence or absence of a significant bulge. We used the star formation rates determined from CALIFA Hα line emission based on the prescriptions of Calzetti (2013) (Catalán-Torrecilla et al.

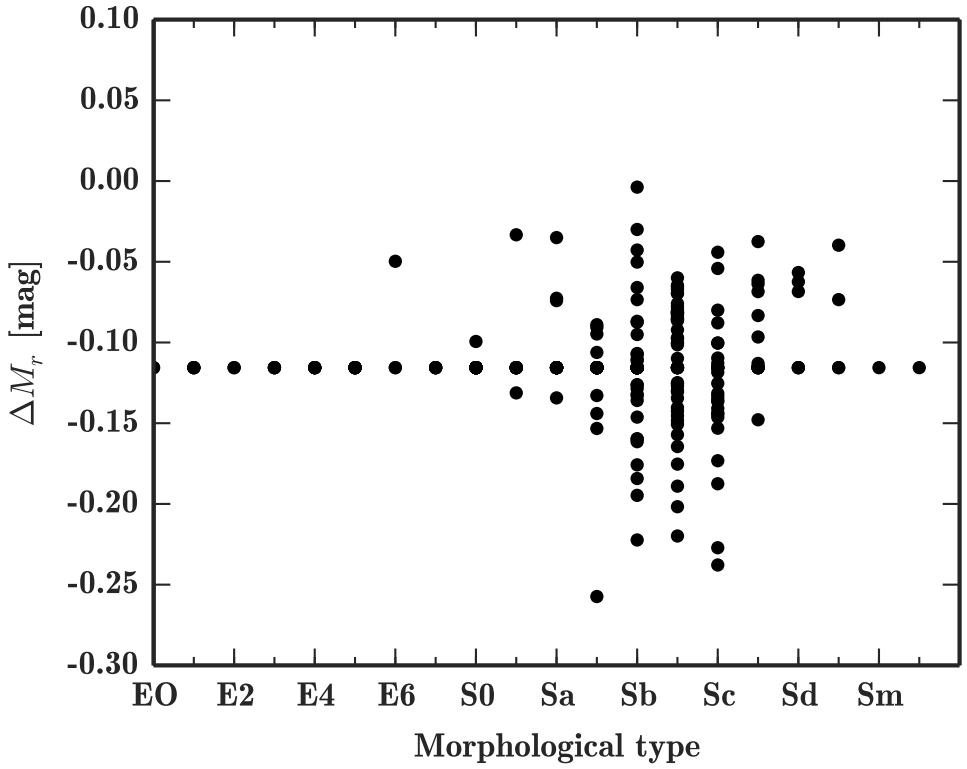

Figure 2.4: Extinction correction vs. visual morphological classification.

2015), photometric stellar masses determined by the collaboration (W14) and integrated CALIFA Hα and Hβ fluxes. The corrected magnitude M_r^c was calculated as $M_r^c = M_r + \Delta M_r$.

To correct the magnitudes for intrinsic attenuation, we needed the Balmer decrement of our sample galaxies. The emission line properties of 30" radius aperture spectra were extracted from the V500-datacubes of the galaxies. This aperture is large enough to include virtually 100% of the FoV of the CALIFA datacubes, without the need to select a different aperture for each galaxy.

To extract the information contained in the spectra, we followed the procedures described in Sánchez et al. (2014), using the fitting package FIT3D[1].

Individual emission line fluxes were measured using FIT3D in the stellar-population-subtracted spectra performing a multicomponent fitting using a single Gaussian function. By subtracting a stellar continuum model derived with a set of SSP templates, we corrected for the effect of underlying stellar absorption, which is particularly important in Balmer lines (such as Hβ).

Visual morphological classifications were used to distinguish between galaxies with and without significant bulges, which have different dust correction prescriptions. We assumed that galaxies that had been classified as Sc and later had no significant

[1] `http://www.caha.es/sanchez/FIT3D/`

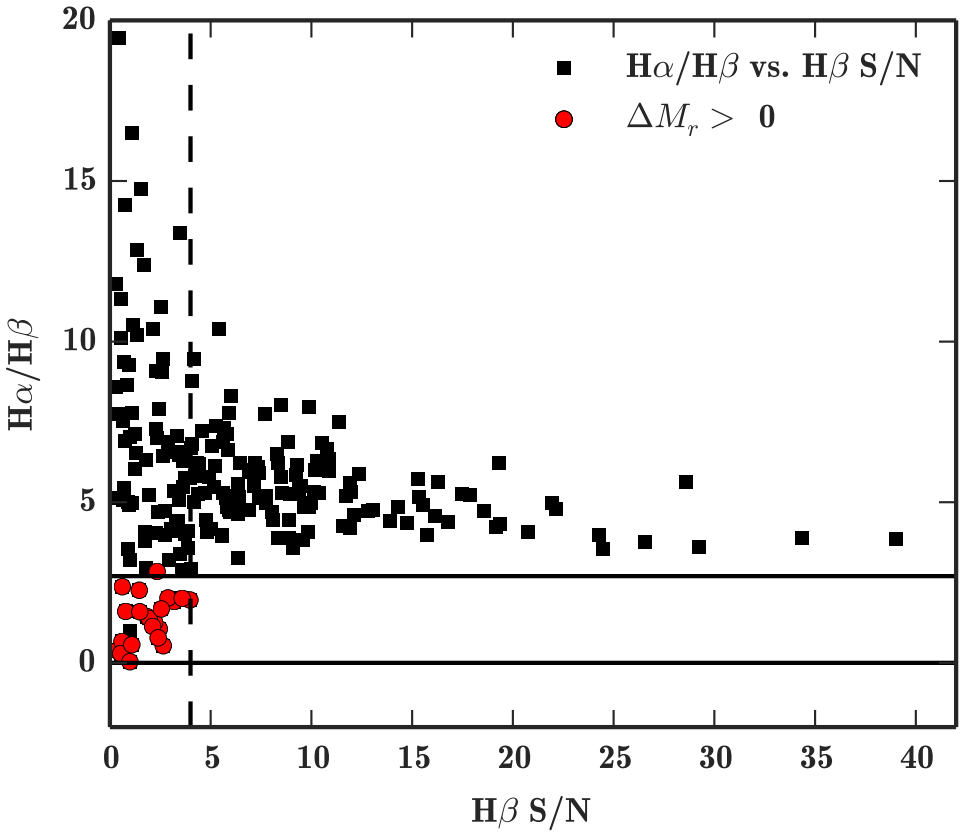

Figure 2.5: Balmer decrement vs. H_β S/N. The red points are the galaxies that had unreliable extinction corrections due to their low S/N and correspondingly erroneous Balmer decrement values. The horizontal and vertical dashed lines show the region of probably untrustworthy extinction correction estimates. We used the mean magnitude of the extinction correction for these galaxies, see text.

bulge. The correspondence between the visual morphological classification and the magnitude of the extinction correction is shown in Fig. 2.4.

It should be noted that we used kinematic inclination values obtained in the following section elsewhere in the analysis, especially when correcting the rotation curves for inclination. However, the methods described in Wild et al. (2011a,b) were derived using the photometric axis ratio as an input, therefore we employed it in our analysis for the sake of consistency.

We clipped the star formation rates and axis ratios to the maximum values provided in Wild et al. (2011a) (0.3 $< b/a <$ 0.9, -10.2 $<$ log($sSFR$) $<$ -9.3 yr^{-1} for bulge-dominated galaxies and -10.0 $<$ log($sSFR$) $<$ -9.1 yr^{-1} for disk-dominated galaxies).

The CALIFA Hα and Hβ fluxes are not reliable at the low S/N limit, leading to unrealistic Balmer decrements. We settled on making a S/N cut at Hα/Hβ = 2.7 (S/N was very close to 4 there, see Fig. 2.5 for an illustration). For galaxies below the S/N = 4 limit and for those that had no reliable Hα or Hβ fluxes, we adopted the average

extinction correction value $\Delta M_r = -0.11$ mag.

2.5 Velocity field modelling

2.5.1 Model description

It has long been noted that the deprojected rotation curves of galaxies show a variety of shapes (Rubin et al. 1985; Verheijen 2001), exhibiting differences attributed to morphology (Rubin et al. 1985; Verheijen 2001) or luminosity (Persic & Salucci 1991). Several parameterisations of rotation curves exist, some being purely phenomenological (Courteau 1997; Vogt et al. 1996; Rix et al. 1997), some attempting physical parameterisation (Persic & Salucci 1991; van den Bosch et al. 2000; Persic et al. 1996).

We used a variant of the *arctan* function (Courteau 1997), the hyperbolic tangent (Neumayer et al. 2011):

$$v(r) = v_0 + \frac{2}{\pi} v_c \cdot tanh\left[\frac{r}{k \cdot r_{50}}\right], \tag{2.2}$$

where v_0 is the recession velocity, v_c is a free parameter governing the amplitude of the rotation curve, k describes the sharpness of RC turnover, and r_{50} is the optical half-light semi-major axis, determined from r -band growth curve photometry. In addition, a galaxy was allowed to have arbitrary inclination and position angles. We did not allow the kinematic centre position to vary because the spatial resolution of Voronoi bins is variable and sometimes too low to provide a meaningful constraint on the centre position.

The main attraction of this model was its simplicity, that is, the lowest number of free parameters. However, we found that this simple model was unable to fit the rising or falling rotation curves.

At the cost of parameter degeneracy, we assumed another model for RC shapes, implemented in Bertola et al. (1991) and also discussed in Böhm et al. (2004):

$$v(r) = v_0 + \frac{v_c r}{(r^2 + k^2)^{\frac{\gamma}{2}}}. \tag{2.3}$$

The model has four free parameters – v_c, k, v_0 , and γ. The v_c and k parameters here take on similar roles as in the *tanh* model (Eq. 2.2), but their values are different. The γ parameter, which typically varies between 0.8 and 1.2, allows modelling rising and falling rotation curves. A flat rotation curve is obtained when $\gamma = 1$.

In most optical studies the TFR defines the rotation velocity as measured at the outer part of a galaxy where the rotation curves are no longer rising. To achieve this, we had to extrapolate the rotation curves of galaxies that were not sampled up to the point of turnover.

We took advantage of an open-source Python implementation (Foreman-Mackey et al. 2013) of affine-invariant MCMC sampler (Goodman & Weare 2010), called through a customised wrapper. MCMC methods provide the full posterior distributions of model parameters, leading to more realistic uncertainty estimates.

To constrain the physical parameters of the models, we applied a truncated Gaussian prior on the γ parameter, effectively constraining it to lie between 0.8 - 1.2. We

found that this range of γ values describes the range of physically possible rotation curves well and helps avoid degeneracies. In addition, we constrained the marginalised rotation velocity at 2.2 scale lengths ($v_{2.2}$) to be below 600 km/s, and restricted $k > 0$.

Even with the simplest hyperbolic tangent model, we observed a strong coupling between the inclination angle and the v_c parameter, that is, the amplitude of the rotation curve. This is expected because almost any velocity field can potentially be modelled as a fast-rotating, almost face-on disk or as an inclined disk with a lower intrinsic rotation velocity if the spatial resolution is low. This proved to be a problem for highly inclined galaxies with a small number of bins (Fig.2.6) because the inclination could not be constrained well.

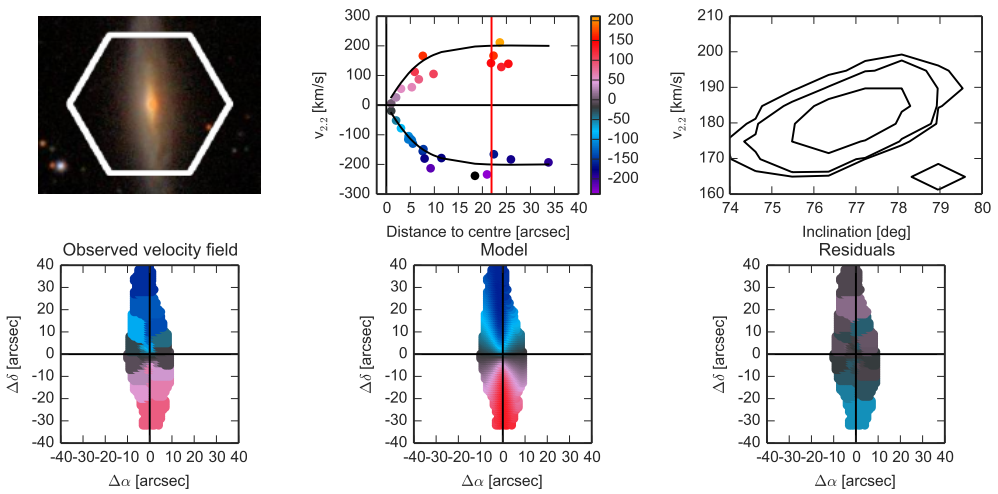

Figure 2.6: Velocity field of an inclined galaxy (IC5376, $i_{phot} = 80°$). Top: SDSS composite image (left), model (black) and measured rotation curves (middle), joint i - $v_{2.2}$ distribution (shown as 1, 2, and 3 standard deviation contours). Bottom: observed velocity field (left), model (middle), and residuals. The red line indicates the location of $2.2l_{sc}$. The velocity scale is the same in all panels.

To break this degeneracy, we introduced a truncated Gaussian prior on the inclination angle for galaxies with $i_{phot} > 75°$. We estimated the prior inclination using Eq. 2.1 and the photometric axis ratios provided in W14, assuming the intrinsic disk thickness $q = 0.2$ and the standard deviation of the Gaussian $\sigma = 3°$.

All photometric axis ratios were inspected visually and found to be quite accurate inclination indicators for highly inclined galaxies. This is not necessarily the case for low-inclination galaxies that can look less circular than they are as a result of spiral arms and other irregularities.

We noted a strong bimodality in the marginalised $v_{2.2}$ distribution for a number of objects. It occurred either as a consequence of a low number of Voronoi bins and therefore poorly constrained inclination, or of the inability to constrain the model based on kinematic information alone. In these cases, an identical truncated Gaussian prior was placed to constrain the inclination (and, consequently, $v_{2.2}$) to a more plausible range.

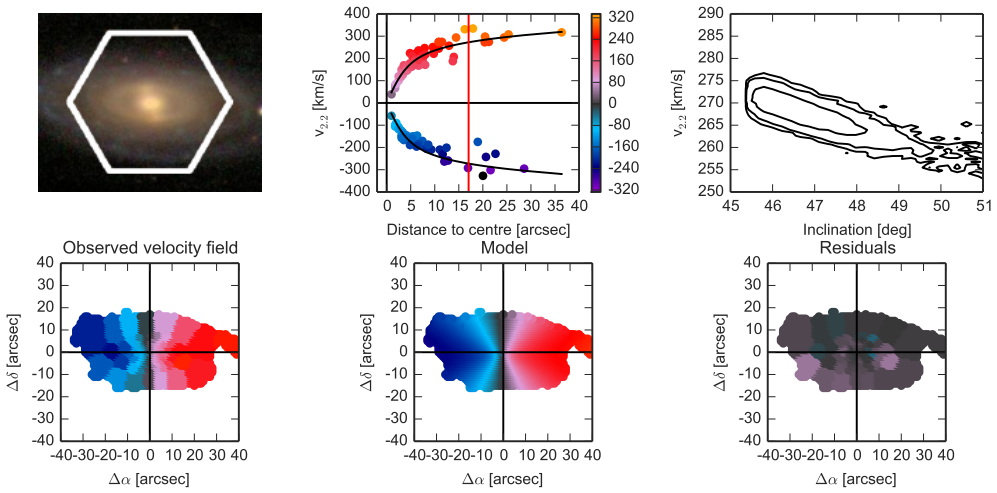

Figure 2.7: Top: SDSS composite image of NGC1645 (left), model (black), and measured rotation curves (middle), joint i - $v_{2.2}$ distribution. Bottom: observed velocity field (left), model (middle), and residuals. The photometric inclination was estimated to be equal to 52°.

We took 480000 MCMC samples for each galaxy, rejecting the first 160000 to reduce the effect of the choice of initial parameters. The chain lengths were chosen after repeated modelling had shown that the models selected were robust, meaning that the parameter distributions did not change between fits. The MCMC outputs provide the full distributions of rotation curve parameters, inclination, and position angle values for each galaxy. From these we can obtain the marginalised posterior distribution of the modelled velocity at a given radius, as well as kinematic inclination and position angle estimates. Two examples of observed and model velocity fields, as well as their rotation curves and joint inclination-$v_{2.2}$ distributions, are shown in Figs. 2.6 and 2.7.

The mean values and standard deviations of kinematic inclination and position angles were determined through directional statistics, that is, by calculating the vector means and circular standard deviations of the chain values. Although the inclination and position angles were allowed to vary freely during fitting, the resulting chain values were wrapped to intervals $[0; 90]$ and $[0; 180]$, respectively.

2.5.2 Definition of rotation velocity measure

When the rotation velocity is measured at the outer parts of a galaxy, the TFR links the halo properties and the baryonic mass. However, in practice it is difficult to connect the true halo-induced velocity and the measured velocity because the radial coverage is limited (Verheijen 2001). The rotation velocity has to be measured at a particular point of the rotation curve, which affects the slope of the TFR (Yegorova & Salucci 2007). It is often measured at $r_{2.2} = 2.2\ l_{sc}$, where l_{sc} is the exponential scale radius of the disk, as well as at r_{opt}, the radius containing 83% of all light (Courteau 1997). Other non-parametric definitions are also employed, for example, the maximum rotation velocity v_{max}, rotation velocity at the flat part of the rotation curve (v_{flat}), and the mean value of

the outermost points of a rotation curve (see Böhm et al. (2004) for a discussion).

Two practical measures are $v_{2.2}$ and $v_{\rm opt}$. We were reluctant to use $v_{\rm max}$, $v_{\rm flat}$ and other non-parametric measures of the circular velocity because outlier points on the rotation curves were frequent as a result of Voronoi binning or lack of masking and not all the rotation curves were asymptotically flat. We decided to use $v_{\rm opt}$ as our velocity measure because it is straightforward to compare with simulations and other observations as opposed to $v_{2.2}$ measuring, which requires structural decomposition of a galaxy.

The mean coverage of CALIFA velocity fields, that is, the largest radius divided by $r_{\rm opt}$, is shown in Fig.2.9.

In addition, we checked whether the galaxies with lower spatial coverage are offset from the TFR. We did not find a significant offset (see Fig.2.18 in Sect.2.7).

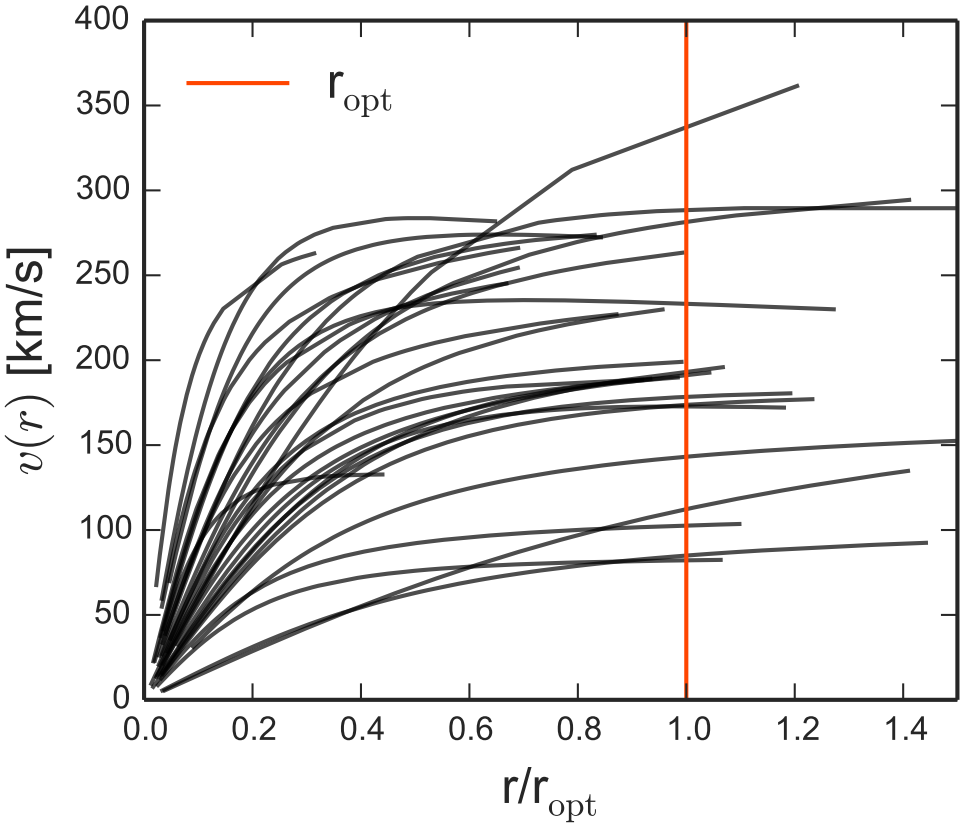

Figure 2.8: Random sampling of 30 rotation curves scaled to $r_{\rm opt}$, shown as the vertical line.

2.5.3 Modelling results and uncertainties

For each galaxy we estimated the rotation velocity $v_{\rm opt}$ by choosing between the two models described in Sect. 2.5.1. For the absolute majority (all except nine) of the galaxies, the more complex Bertola et al. (1991) model was preferable. In the three

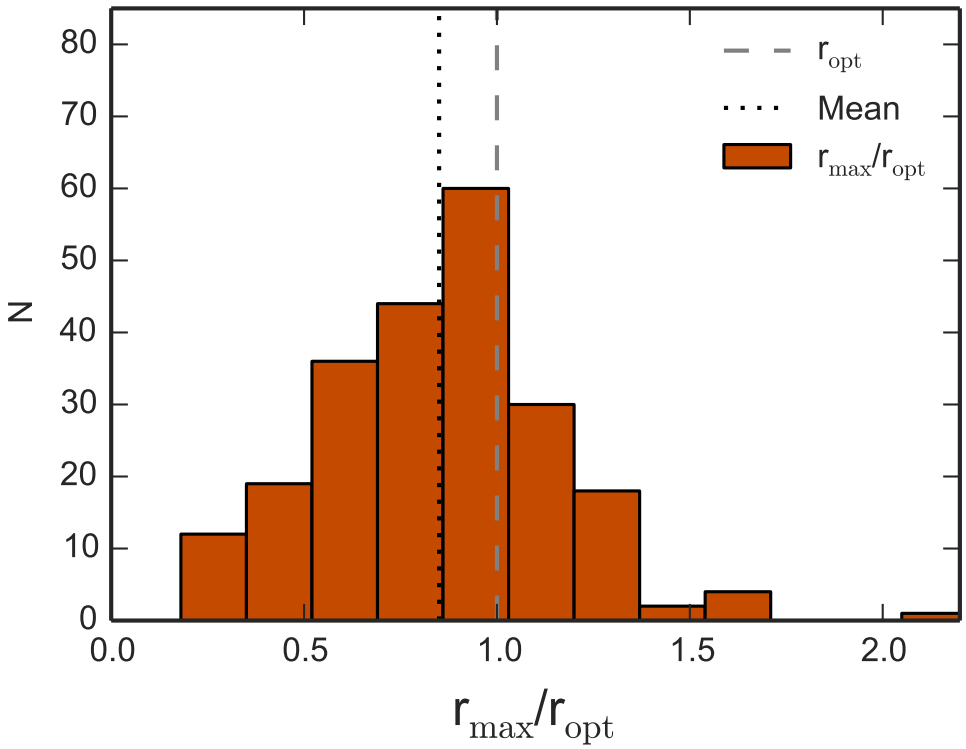

Figure 2.9: Relative spatial coverage histogram of CALIFA stellar velocity fields. The dotted line denotes the mean value within the sample, the dashed line is at r_{opt}.

cases when both models were clearly incorrect in the outer parts of the galaxies, we picked the mean value of the last two points and added 20 km/s to the rotation velocity uncertainty.

Figure 2.10 shows the comparison of kinematic and photometric inclination estimates. As expected (Schommer et al. 1993), the photometric inclination estimates are systematically higher for low-inclination galaxies because any irregularity in the apparent light distribution forces the axis ratio towards lower values. At higher inclinations, inclination estimates of galaxies classified as mergers and slow rotators tended to differ the most. Nevertheless, this does not present a problem for TF studies because the intrinsic rotation velocity is obtained by dividing the line-of-sight rotation velocity by the sine of the inclination angle, and the slope of the sine function is shallow for angles above 75°. We employed an identical Gaussian prior as above for the majority of galaxies with $i \geq 75°$, therefore kinematic and photometric estimates tend to converge at the highest inclinations.

To estimate the reliability of v_{opt} measurements, we discuss the potential sources of uncertainties. MCMC modelling provides estimates for uncertainties inherent in modelling a particular galaxy.

For some galaxies the main source of velocity uncertainties was the limitations of the simple rotating disk model. For instance, mergers and slow rotators showing

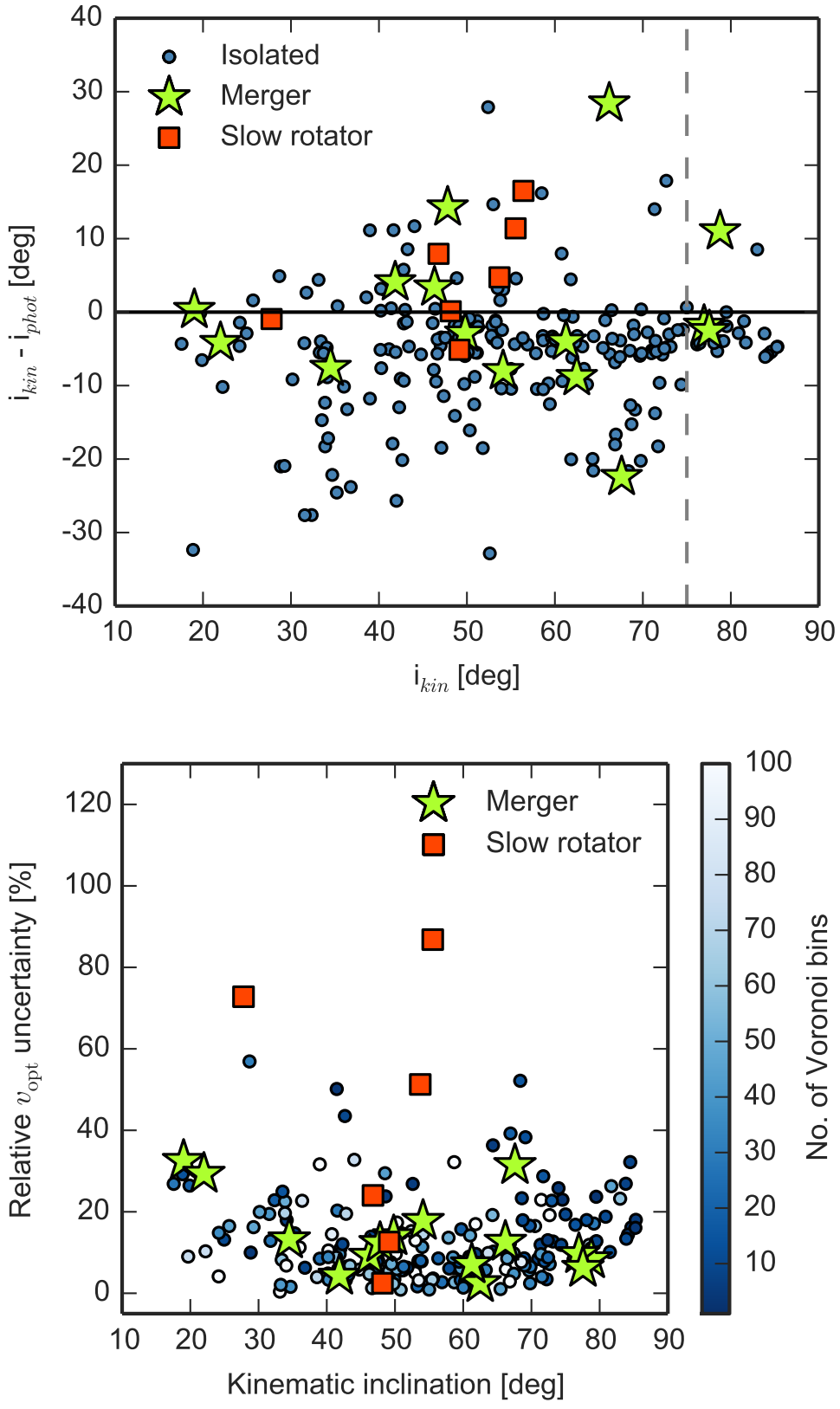

Figure 2.10: Top: Difference between kinematic and photometric inclination estimates, calculated from *r*-band axis ratios assuming the intrinsic disk thickness $q = 0.2$. Slow rotators and interacting galaxies are marked in red and light green, respectively. Bottom – $v_{\rm opt}$ uncertainties vs. kinematic inclinations.

little or no ordered rotation could not be well constrained and had broad, non-Gaussian posterior distributions of $v_{2.2}$. Relative v_{opt} uncertainties vs. kinematic inclinations are shown in Fig.2.10, demonstrating the difficulty of constraining the rotation velocity of slow rotators. Because of their large velocity uncertainties, they would not contribute significantly to the fit of the TFR. However, the majority of such galaxies were rejected from the final Tully-Fisher sample as described in Sect.2.6.2.

Other potential sources of uncertainties include the limited CALIFA field of view and the spatial resolution of the binned stellar velocity fields. However, they are either implicitly included in the posterior v_{opt} uncertainties or too difficult to estimate within the scope of this paper. A careful analysis of uncertainties in the template TFR context is presented in Saintonge & Spekkens (2011).

In most previous TF work the photometric axis ratio b/a has been directly converted into inclination, without assuming any associated uncertainties or potential difference between kinematic inclination (i.e. the real inclination of the observed rotating component) and its photometric estimate based on b/a. This has led to rotation velocity estimates with uncertainties of the order of a few km/s and TFRs with negligible uncertainties on the line fit parameters. In our opinion, using kinematic inclination values is more justified than deriving them independently from the photometric axis ratio. In addition, MCMC modelling of the velocity fields provides the full posterior distribution of velocity uncertainties. This consistent self-contained rotation curve modelling is only possible with IFS data.

However, the stellar velocity fields we used here have their own share of problems, such as large Voronoi bins and limited spatial extent, and therefore are likely to lead to larger velocity measurement uncertainties than the other methods. A direct comparison on the velocity uncertainties derived using the different methods and data (such as stellar or gas 2D velocity fields or long-slit observations) is beyond the scope of this paper. The consistent velocity uncertainties provided by the methods presented here can be propagated into a TFR fit, providing more reliable constraints on its internal scatter.

2.5.4 Calculating the circular velocity

We used stars as the tracer of the circular velocity of the galaxies. Stellar velocity fields have the advantage of being available for all morphological types and also of being less distorted than gas fields (Adams et al. 2012; Kalinova & Lyubenova 2015). However, stars are dynamically hot tracers, and a so-called asymmetric drift correction, which takes the velocity dispersion into account, is frequently applied to obtain the circular velocity v_{circ}.

According to Kalinova & Lyubenova (2015) and Kalinova et al. (submitted), the classical (Weijmans et al. 2008) asymmetric drift correction (ADC) underestimates the real underlying potential if the local inclination-corrected rotation velocity and velocity dispersion ratio V/σ is lower than 1.5. This implies that asymmetric drift corrections would be inaccurate for the majority of galaxies within our sample. Even though the asymmetric drift correction changes the shape of the inner rotation curve dramatically, the estimated circular velocity does not change significantly for rotation-supported galaxies. However, the classical ADC approach is unsuitable when the assumption of a thin disk is not valid.

We decided to avoid the classical ADC to treat our sample in a consistent, homogeneous manner. Although advanced dynamical modelling is beyond the scope of this observational paper, we decided to apply an empirical correction based on the findings of Kalinova & Lyubenova (2015). They analysed the difference between dynamical masses inferred using classical ADC models and axisymmetric Jeans anisotropic multi-Gaussian (JAM) models applied to stellar mean velocity and velocity dispersion fields of 18 late-type galaxies observed with the SAURON IFS instrument. We used the relation derived from Table 4 of Kalinova et al. (submitted) and calculated the circular velocities by multiplying the measured velocity by the square root of the factors provided, based on the local measured $v_{\rm opt}$/LOS $\sigma_{\rm opt}$ of a galaxy. The uncertainty of the calculated circular velocity was calculated by adding in quadrature 10 km/s multiplied by 1 + ΔV (where ΔV is the square root of the uncertainty factor from Kalinova et al. (submitted)) to the $v_{\rm circ}$ uncertainty budget. The magnitude of the correction is shown in Fig. 2.11.

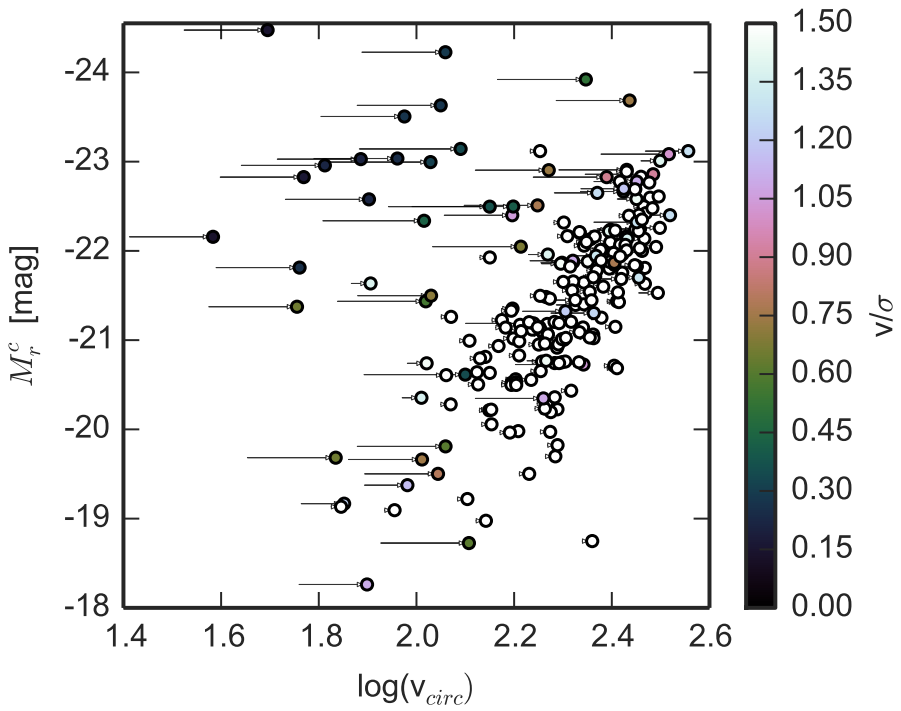

Figure 2.11: Magnitude of the circular velocity correction shown as arrows. The points are the final circular velocity values, colour-coded for the $v_{\rm opt}/\sigma$ factor. The galaxy with the lowest log($v_{\rm circ}$) value, a slow rotator, is not shown for clarity. This galaxy, NGC 6515 (log($v_{\rm circ}$) = 1.05), was excluded from further analysis during the outlier rejection procedure described in Sect. 2.6.2.

We compared the gas rotation velocities of 44 galaxies obtained from CALIFA DR1 data (García-Lorenzo et al. 2015) with their stellar circular velocity values, shown

in Fig.2.12 below. Ionised gas rotation curves were obtained from the envelope of the position-velocity diagram and corrected for inclination using photometric axis ratio b/a, then gas v_{opt} values were evaluated at the optical radius.

This is not a direct and accurate comparison for many reasons. First of all, even though ionised gas is typically less dynamically hot than the stars, the measured gas rotation velocity does not trace the gravitational potential directly and the gas dispersion needs to be taken into account. This presents additional difficulties because the gas dispersion cannot be measured directly with the CALIFA spectral resolution. Furthermore, thermal motion and gas turbulence also contribute to the total gas velocity dispersion and cannot be distinguished from gravitationally induced velocity dispersion without additional data (Weijmans et al. 2008). In addition, the gas v_{opt} was estimated in a different way from the stellar rotation velocity. Photometric inclination estimates were used instead of kinematic ones and no rotation curve modelling was performed, which means that any warps or distortions present in ionised gas were not accounted for. The most noticeable outliers in Fig.2.12 are offset as a result of the latter reasons. Despite this, the two quantities are close to each other for most of the galaxies, with the stellar v_{circ} being typically larger as expected from the arguments above. A similar comparison for several CALIFA galaxies, using a different asymmetric drift correction method, is shown in Aguerri et al. (2015).

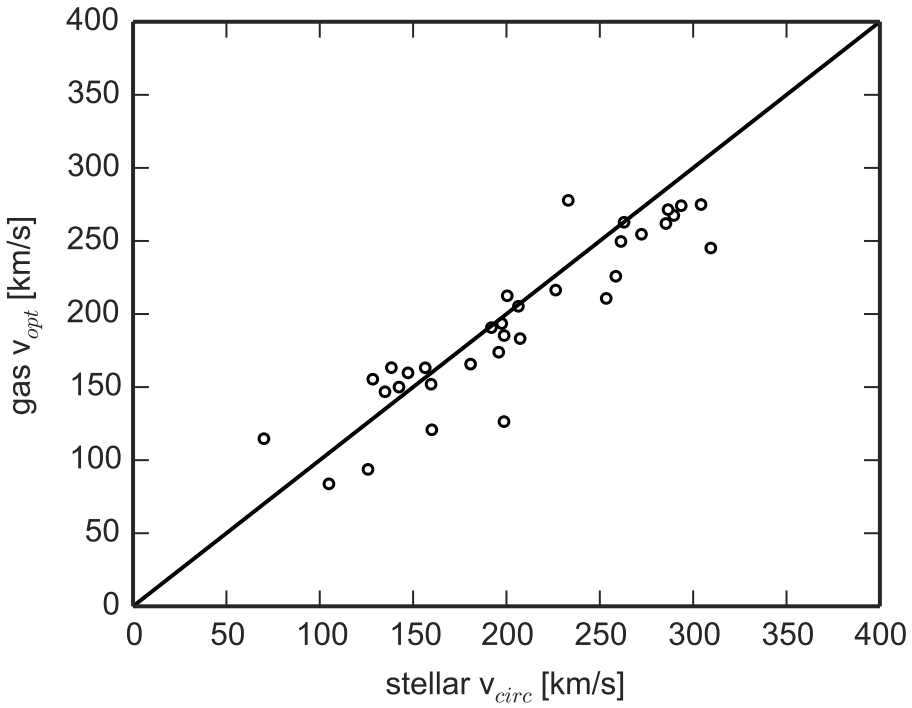

Figure 2.12: Comparison between ionised gas rotation velocity at the optical radius and the stellar circular rotation velocity for 44 CALIFA DR1 galaxies.

We use the calculated circular velocity values in all further analysis unless noted otherwise.

2.6 Separation of different populations of galaxies in the M_r - $v_{\rm circ}$ plane

2.6.1 Specific angular momentum

The specific angular momentum j and the total mass are key properties of galaxies that strongly influence their morphology, luminosity, and secular evolution. A directly measurable quantity in IFS observations, related to j, is the λ_R parameter, defined in Emsellem et al. (2007) as

$$\lambda_R \equiv \frac{\langle R\ |V|\rangle}{\langle R\ \sqrt{V^2+\sigma^2}\rangle}. \tag{2.4}$$

In practice, λ_R is calculated in the following way (Emsellem et al. 2007):

$$\lambda_R = \frac{\sum_{i=1}^{N_p} F_i R_i\,|V_i|}{\sum_{i=1}^{N_p} F_i R_i \sqrt{V_i^2+\sigma_i^2}}, \tag{2.5}$$

where F_i, R_i, V_i and σ_j are the fluxes, semi-major axis values, velocities, and velocity dispersion values of a spatial Voronoi bin i.

Measurements of λ_R parameter values are available for the galaxies in our sample from work done within the CALIFA team. For CALIFA galaxies, the $\lambda_{\rm Re}$ parameter (λ_R within one effective radius R_e) was calculated as described by Eq. 2.5 and corrected for inclination as described in Falcón-Barroso et al. (submitted), also see Falcón-Barroso et al. (2015b) and Querejeta et al. (2015). Briefly, ellipticities ϵ were obtained from IRAF ellipse fit models of the SDSS r-band images, and the probability of observing a galaxy with an inclination i, given its ellipticity ϵ, was calculated as

$$f(i|\epsilon) = \frac{f(q)(1-\epsilon)}{\sqrt{sin^2 i - \epsilon(2-\epsilon)}}, \tag{2.6}$$

where $f(q)$ is the intrinsic shape distribution of galaxies. The $\lambda_{\rm Re}$ values were available for 206 out of 226 galaxies because the authors rejected the galaxies with a low number of bins (typicaly ≤ 10) and interacting galaxies showing obvious kinematic irregularities from their calculation.

Although minor inconsistencies arise from using slightly different parameters (such as inclinations) in this analysis, we emphasize that the lambda parameter was used in this study only as a qualitative illustration of the degree of rotation support in our sample galaxies. These minor inconsistencies and lack of $\lambda_{\rm Re}$ values for some of the galaxies thus have no influence on any quantitative result in the paper.

Figure 2.13 shows that the galaxies on the circular velocity-luminosity plane are drawn from at least two parent distributions: galaxies that exhibit significant ordered rotation and belong on the TFR, and the rest, including pressure-supported galaxies and some ongoing mergers. As a consequence, some of the data, even though they are of reasonable quality, are simply beyond the scope of the simple model of the TFR, which

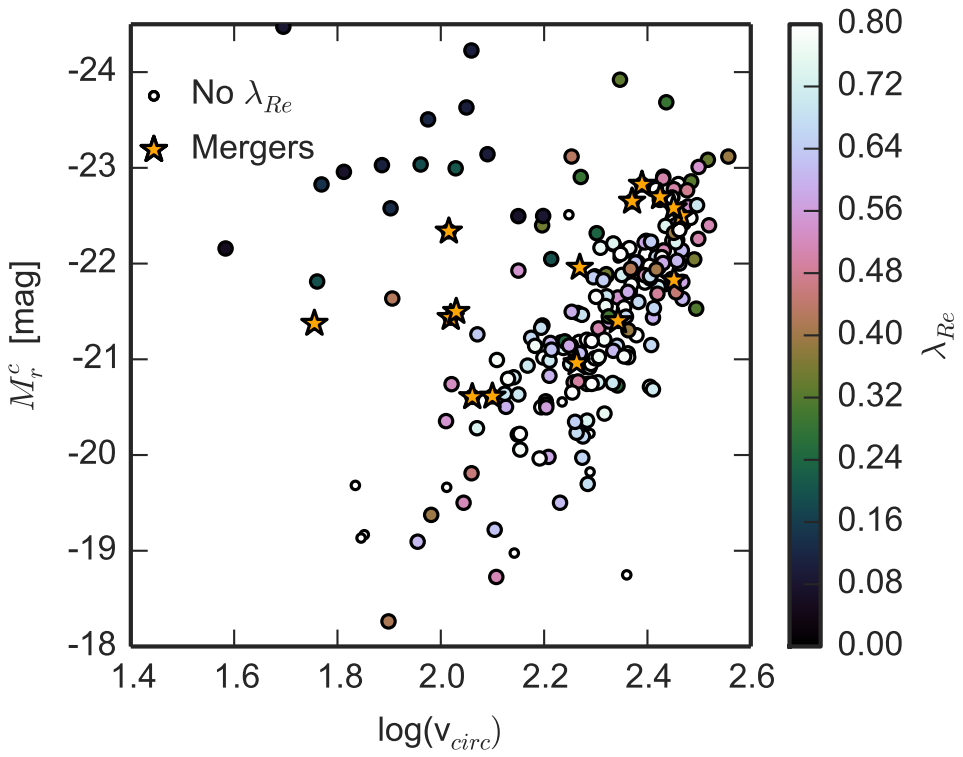

Figure 2.13: Galaxies on the $v_{\rm circ} - M_r^c$ plane, colour-coded for inclination-corrected $\lambda_{\rm Re}$ parameter. The 20 galaxies without $\lambda_{\rm Re}$ values available (see text) are shown as smaller white circles.

is a linear relation with small intrinsic scatter. Since linear regression is very sensitive to outliers and, more importantly, some of the galaxies in our sample do not belong on the TFR by definition, some sort of outlier rejection must be performed.

2.6.2 Modelling the TFR as a mixture of Gaussians

We did not apply any additional selection criteria to our galaxy sample (see Sect. 2.3), except for those that are implicit in the CALIFA mother sample selection and properties of the SDSS survey. As a result, it contains different galaxy populations, not all of which are well described by a thin rotating-disk model assumed in Sect. 2.5 (mergers and slow rotators are two examples).

We did not simply reject the outliers using an arbitrary procedure such as hand-pruning the data, sigma-clipping, or straightforward rejection of slow rotators and visually classified mergers. Instead, we modelled the distribution as a mixture of data obtained from two different generative models: a narrow, linear relation with Gaussian noise and small intrinsic scatter (corresponding to the subset of galaxies to which the TFR applies) and a two-dimensional Gaussian distribution that includes the galaxies that lie farther away from the linear relation.

The probability density function of a linear TFR with a small intrinsic Gaussian

scatter σ_i is

$$P(v|M,m,b,\sigma) = \frac{1}{\sqrt{2\pi(\sigma_y^2 + m^2\sigma_x^2 + \sigma_i^2)}} \exp\left[-\frac{(M - mv - b)^2}{2(\sigma_y^2 + m^2\sigma_x^2 + \sigma_i^2)}\right], \tag{2.7}$$

where v is the logarithm of circular velocity, M is the absolute magnitude, and m and b are the slope and the offset of the linear relation.

The non-TF distribution is quite sparse, therefore we chose a non-restrictive two-dimensional Gaussian model described by its mean in two dimensions (μ_x, μ_y) and a covariance matrix

$$\Sigma = \begin{vmatrix} \sigma^2_{\rm bad_x} & \rho\sigma_{\rm bad_x}\sigma_{\rm bad_y} \\ \rho\sigma_{\rm bad_x}\sigma_{\rm bad_y} & \sigma^2_{\rm bad_y} \end{vmatrix}. \tag{2.8}$$

Here $\sigma_{\rm bad_{x,y}}$ are the standard deviations of the non-TF points population, whose shape is allowed to vary, and ρ is its correlation term.

When we combine both models, we can obtain a probability of belonging to the TFR for each datapoint and reject the outliers based on this probability. We finally had seven free parameters describing the two distributions $(m, b, \sigma_i, \mu_x, \mu_y, \sigma_{\rm bad_x}, \sigma_{\rm bad_y})$, which we inferred and marginalised over the nuisance parameters P_b (the probability of any point belonging to the non-TF distribution) by finding their posterior distributions using MCMC. The log-likelihood of the mixture of the two distributions described above is

$$\begin{aligned} &\ln \mathcal{L} \propto \\ &\propto -0.5\Sigma\left((1 - P_b)\cdot\left[\ln(\sigma_y^2 + m^2\sigma_x^2 + \sigma_i^2) + \frac{(y - mx - b)^2}{(\sigma_y^2 + m^2\sigma_x^2 + \sigma_i^2)}\right]\right. \\ &\left. + P_b\cdot\left[\frac{(x - \mu_x)^2}{(\sigma_x^2 + \sigma^2_{\rm bad_x})} + \frac{(y - \mu_y)^2}{(\sigma_y^2 + \sigma^2_{\rm bad_y})}\right]\right) \end{aligned} \tag{2.9}$$

Modelling involves setting priors on several of the parameters. The sparsity of the population offset from the TFR and because we worked with the logarithm of velocity, which skews the error distribution, meant that we applied Gaussian priors on its mean and variance, based on the estimated moments of the slow rotators population. We also applied a wide Gaussian prior, based on a simple linear fit to the fast rotators alone, on the slope m, and, naturally, limited the P_b to be between 0 and 1 and $\sigma_i, \sigma_{\rm bad} > 0$.

The results of the mixture modelling are shown in Fig. 2.14. We rejected the datapoints with likelihoods lower than $1 - P_{\rm good} = 0.5$, which were those that more likely belong to the non-TFR distribution. This resulted in the rejection of 27 galaxies that were not compatible with being on a linear relation. The remaining 199 galaxies were used in the further analysis and are named the TF sample.

2.6.3 Properties of the outlier galaxies

Seven out of 27 rejected galaxies are slow rotators with $\lambda_{\rm Re} < 0.1$ (Fig. 2.15). Two galaxies are classified as mergers, and several of the rejected galaxies are not sufficiently sampled by the CALIFA observations.

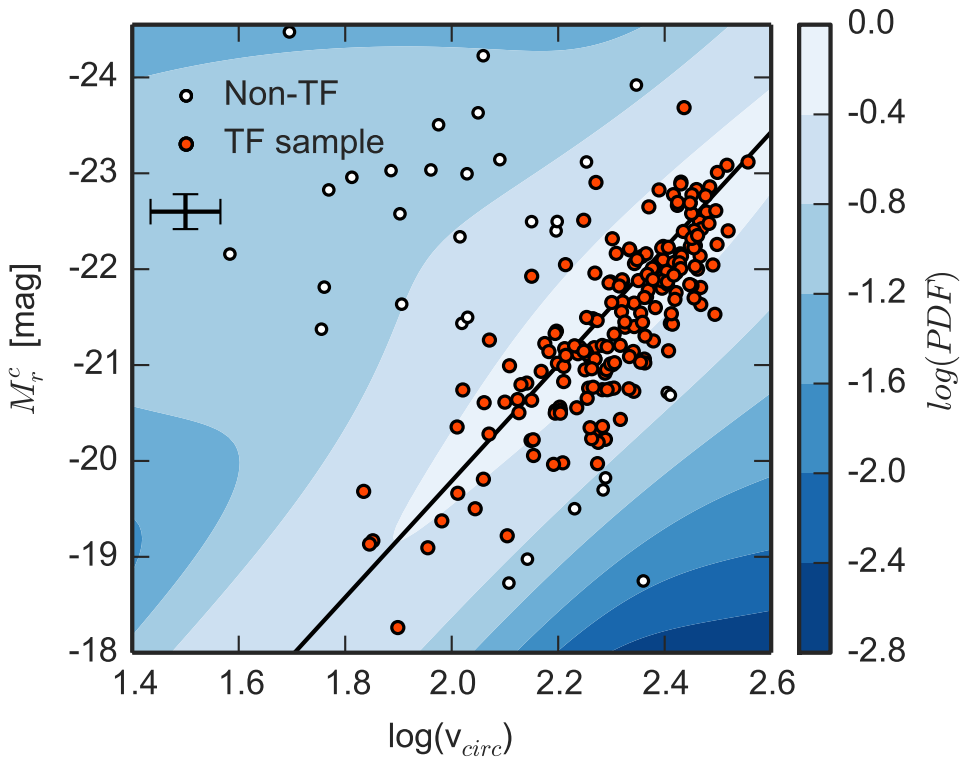

Figure 2.14: Distribution of non-TF points (white) and the TF population (red), together with their underlying estimated generative functions (a 2D Gaussian and a linear relation with small intrinsic scatter), as described in the text. Error bars in the upper left corner show the mean uncertainties in M_r^c and $\log(v_{\rm circ})$.

A comparison of absolute magnitudes and morphologies between the useful sample (described in Sect. 2.3) and the resulting TF and non-TF samples yielded by the mixture of Gaussian modelling is shown in Fig. 2.16. The most salient property of the outlier rejection is the removal of the majority of bright early-type ellipticals from the TF sample, which has a clear physical basis because such galaxies are much more likely to be slow rotators. However, even if this is expected, the rejection was based not on visual classification, but driven by the data, meaning that it was based on the location of the galaxy on the M_r^c - $v_{\rm circ}$ plane and the uncertainties.

2.6.4 Properties of the Tully-Fisher sample

To characterise the final TF sample, we compared the luminosity functions derived from the volume-corrected CALIFA mother sample and the volume-corrected TF sample (Fig. 2.2). We performed the procedure as described in Sec.2.3 and W14: by weighting each galaxy with its $1/V_{\rm max}$ factor.

They differ significantly at the lower luminosity end, where the LF of the TF sample falls off sharply. The difference is not as pronounced for the brightest galaxies

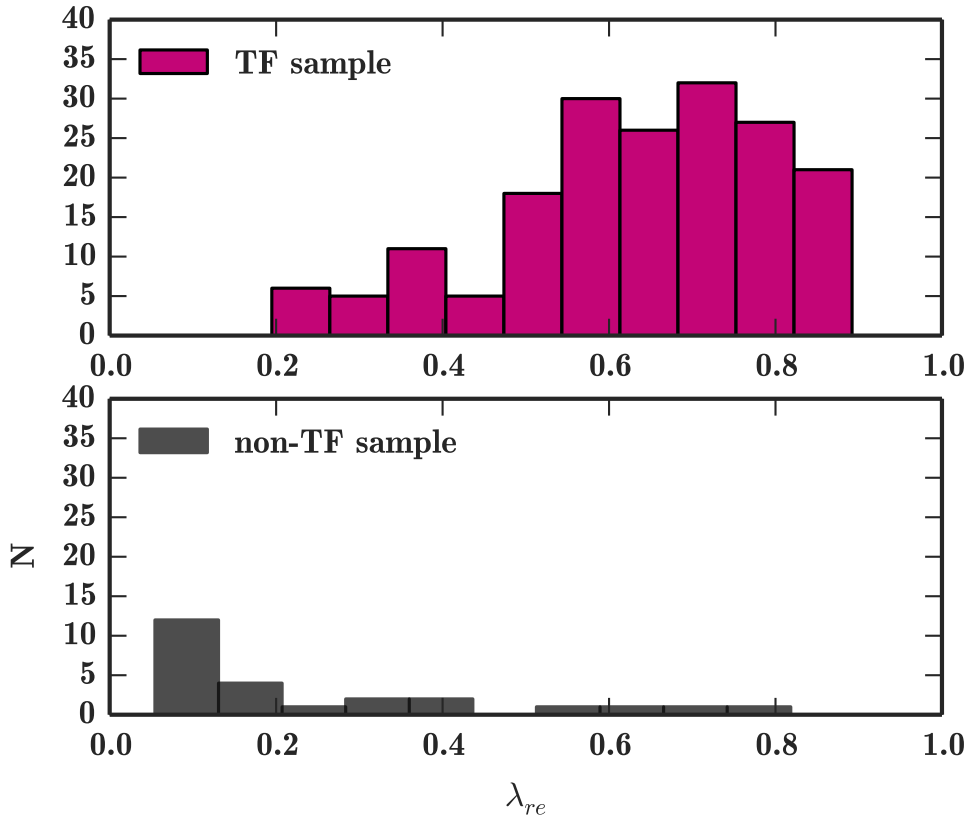

Figure 2.15: Lambda parameter $\lambda_{\rm Re}$ histogram for the TF sample (top) and the 25 outlier galaxies for which $\lambda_{\rm Re}$ values were available.

because of the low number statistics for such objects in the volume-complete sample. We did not a priori expect to retain the volume completeness during the outlier rejection because the rejection is non-random. The difference between the luminosity functions is an expected outcome of the outlier rejection procedure described in Sect. 2.6.2.

However, the mixture modelling is a reproducible procedure. Given a statistically representative sample, the same procedure can be performed again, yielding a distribution of galaxies that is representative of the overall rotation-supported galaxy population and is a subset of the joint volume-complete sample (within the limits of the observed sample). Even so, Fig. 2.2 shows that the Tully-Fisher sample can nevertheless be considered to be volume complete-able within the -20 $\geq M_r^c \geq$ -22 magnitude range.

To verify that velocity-field-based measurements do not show systematic offsets from the conventional long-slit measurements, we show the M_r^c - $v_{\rm circ}$ distribution of the TF sample and a comparison sample from Courteau (1997, hereafter C97) in Fig. 2.17. The TF sample shows a larger scatter than the comparison sample (the *rms* error of $\log(v_{\rm circ})$ is equal to 0.26 dex), which is expected given that the comparison sample used a sample of galaxies with specific selection criteria, such as late Hubble types, moderately high inclination, and lack of interactions or peculiar properties (Courteau

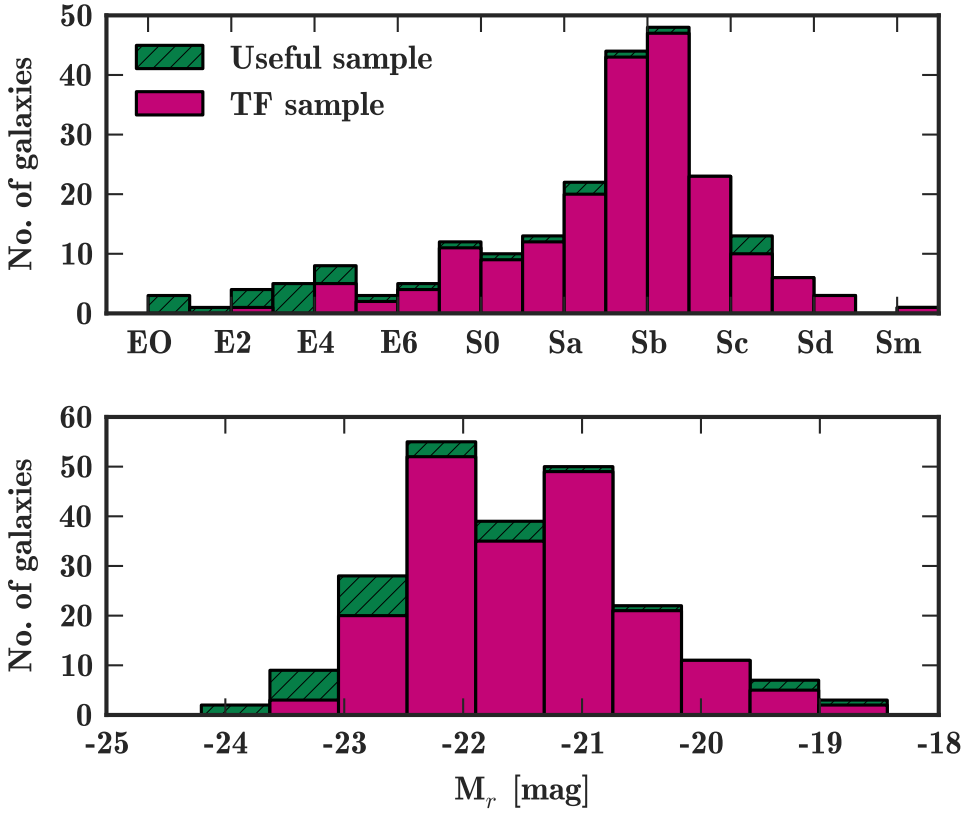

Figure 2.16: Morphological type and absolute magnitude histograms of the final TF sample and the useful sample.

1996). The TF sample has a higher proportion of brighter galaxies of earlier types. In addition to this, the CALIFA stellar circular velocities are typically higher than Hα v_{opt} measurements as a consequence of the circular velocity correction. A direct comparison would involve calculating an equivalent correction for the gas, which is not a trivial endeavour, as discussed in Sect.2.5.4. Nevertheless, the plot shows that circular velocity measurements from IFS velocity fields and rotation curves are compatible and do not show a significant systematic deviation from a similar underlying relation.

2.7 Tully-Fisher relation

Even though a simple straight-line model is not accurate, it is a useful tool in the area of distance determination and has been widely used to model the TFR, as well as to compare the local relation with high-redshift galaxy samples.

For comparison purposes we fitted the TFR as a straight line with free slope, intrinsic scatter and offset (zeropoint) parameters m, σ_i, b, assuming M_r^c as the independent variable. We used the HYPER-FIT hyperplane fitting package (Robotham & Obreschkow 2015), which provides the tools to fit heteroscedastic and covariant data,

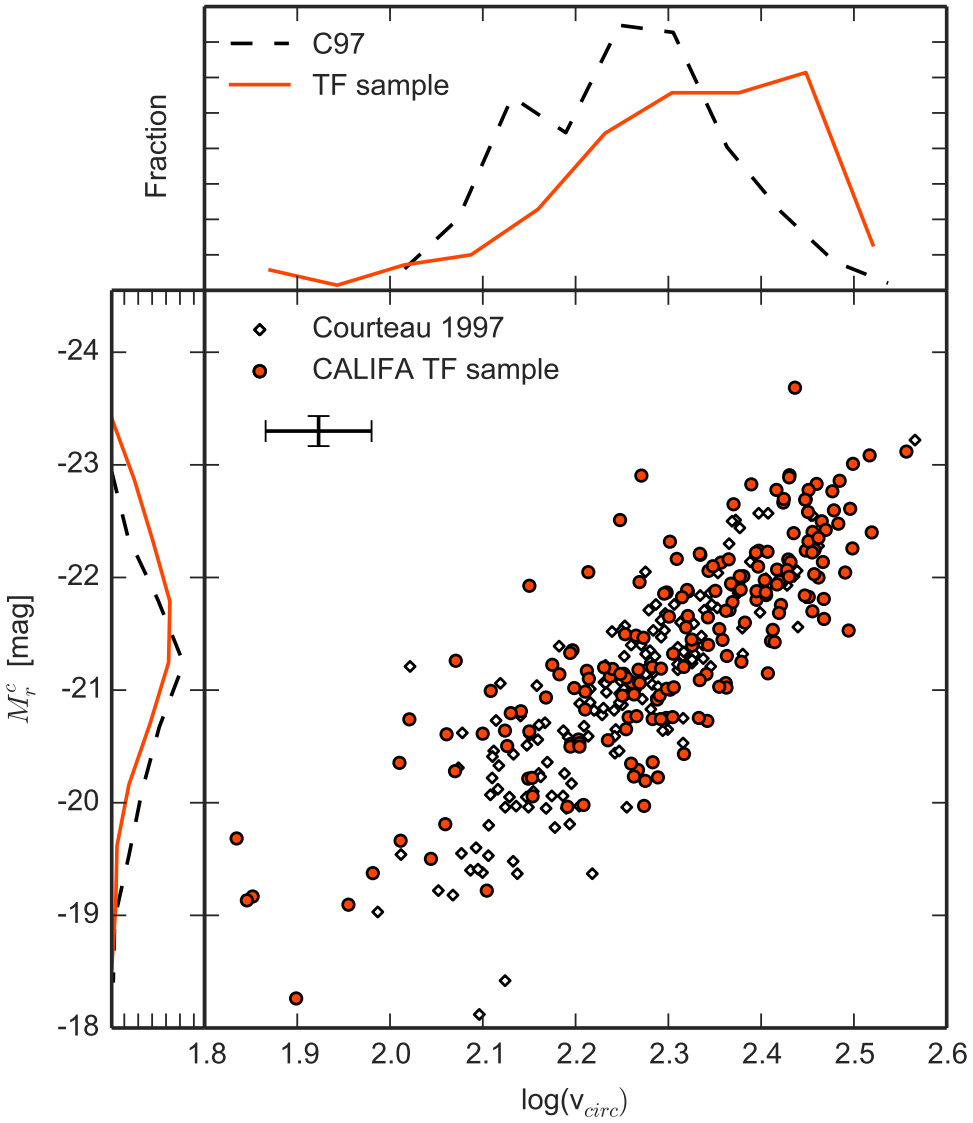

Figure 2.17: Comparison of our Tully-Fisher sample M_r^c - $v_{\rm circ}$ distribution and Courteau (1997) (C97) M_r^c - Hα $v_{\rm opt}$ measurements. The marginal plots show normalised histograms for both samples. The mean uncertainty magnitudes of CALIFA measurements are shown by the error bars.

and used $1/V_{\rm max}$ values as the fit weights.

To verify that the limited spatial coverage of CALIFA velocity fields and the necessity of extrapolating some rotation curves beyond the last measured point (see Sect.2.3) did not introduce a bias, we checked where our datapoints lie on the Tully-Fisher relation. There is no significant offset (Fig. 2.18).

We also verified that the infall corrections described in Sect. 2.4 did not affect the absolute magnitudes significantly by comparing them with luminosities estimated

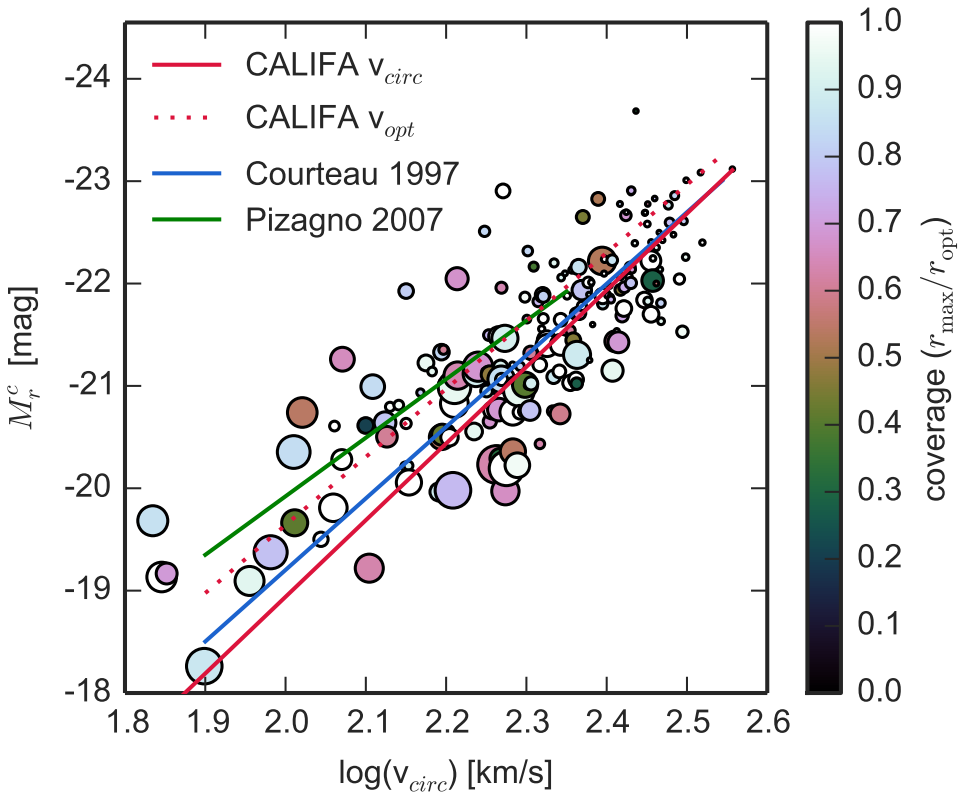

Figure 2.18: Linear fit (see text for more details) to CALIFA $v_{\rm circ}$ - M_r^c data, and comparison with Courteau (1997) and Pizagno et al. (2007) TF fits. Point sizes are proportional to $1/V_{\rm max}$ weights, colours indicate insufficient spatial coverage of the velocity field (sampling of the rotation curve is lower than 1 $r_{\rm opt}$). The fit to $v_{\rm opt}$ - M_r^c is also shown in the plot.

using pure Hubble-flow-based distances. Although the average difference between the two values is equal to 0.14 mag, there is no systematic effect on the TFR. Similarly, the lack of the extinction corrections described in Sect. 2.4 had a negligible effect on the intrinsic scatter of the TFR, but it made the slope slightly steeper.

We compared our fit result with C97 and Pizagno et al. (2007, hereafter P07), who investigated the r-band TF relation using Hα rotation curves, based on $v_{\rm opt}$. Our TFR, fit using a $v_{\rm circ}$ estimate, is shifted to the right and is steeper. Using the $1/V_{\rm max}$ weights leads to a slightly flatter TFR. This is expected because the unweighted relation is dominated by the more luminous galaxies. Applying volume weights acts in the opposite direction and brings the fit relation closer to the results of C97, which are based on a sample dominated by late-type spirals, as shown in Fig.2.17.

The slope, offset, and scatter values for a $v_{\rm circ}$ and $v_{\rm opt}$-based Tully-Fisher relation are provided in Table 2.1. The table also contains the forward TFR parameters provided by C97 and P07. We note that the scatter value reported by us is not the standard deviation of the points from the straight fit line, but the intrinsic scatter not accounted for

Table 2.1: Tully-Fisher relation fit parameters and literature values.

Velocity definition	slope	offset	scatter
CALIFA $v_{\rm circ}$	-7.5±0.5	-4.0±1.0	0.03±0.06
CALIFA $v_{\rm opt}$	-6.7±0.4	-6.3±0.9	0.09±0.03
C97 $v_{\rm opt}$	-6.99±0.33	-5.23±0.46	0.46
P07 $v_{\rm opt}$	-5.72±0.19	-7.9±0.03	0.42

by the measurement uncertainties during the modelling. The *rms* error of our measurements is 0.26 mag.

The intrinsic scatter value we obtain suggests low upper limits on the intrinsic scatter of the TFR. The sources of it include scatter in the dark matter halo spin, concentration and response to galaxy formation (Dutton et al. 2011), potential ellipticity (Franx & de Zeeuw 1992) and formation history (Eisenstein & Loeb 1996; Giovanelli et al. 1997), mass-to-light ratio (Gnedin et al. 2007) and morphology (Giovanelli et al. 1997), among others. A more in-depth study of the intrinsic TFR scatter that would include the additional measurement errors resulting from our adopted infall, extinction and circular velocity corrections is beyond the scope of this paper, but it is unlikely that the reported intrinsic scatter would be increased.

2.8 Volume-corrected bivariate distribution function in the Tully-Fisher plane

The volume and large-scale correction procedure described in Sect. 2.3 can be used to reconstruct a volume-complete bivariate distribution in the $M_r^c - v_{\rm circ}$ plane, applicable within the CALIFA completeness limits.

We used the kernel density estimation (KDE) to achieve this. KDE is a non-parametric probability density estimation procedure (Rosenblatt 1956; Parzen 1962) consisting of representing each datapoint as a smooth distribution and then inferring the underlying density distribution. It is superior to histograms because a smooth kernel can be chosen, there is no dependence on the choice of the starting bin, and the probability density function is obtained naturally.

We chose a two-dimensional Gaussian as the kernel function. The size and orientation (the kernel function covariance matrix) can be selected using various methods, such as cross-validation, or using one of the rules-of-thumb that empirically estimate the bandwidth based on the number of data points and dimensions of the dataset. We estimated the optimal kernel bandwidth based on the global shape of the distribution and the Silverman rule (Silverman 1986). First of all, the global covariance matrix of all the observed points was estimated, assuming that the observed point distribution is similar to a Gaussian distribution in a sense that it is unimodal, symmetric, and not heavy-tailed. Then this matrix was multiplied by a scaling factor $f_s = n^{-\frac{1}{6}}$, derived according to the Silverman rule (Scott & Sain 2005). Here n is the number of data points.

We used the *stats.gaussian_kde* routine from *SciPy* package (Jones et al. 2001-2015) as the basis for our analysis. The left panel of Fig. 2.19 shows the probability

density distribution in the v_{circ} - M_r^c space. The density distribution here is dominated by the brighter galaxies with M_r^c > -20.5 mag and v_{circ} > 200 km/s because of the CALIFA sample construction and smaller relative scatter at larger log(v_{circ}) values.

However, this picture changes when the $1/V_{max}$ factors are included as additional KDE weights, as shown in the right panel of Fig. 2.19. The area with the highest probability density now shifts to lower velocities (< 250 km/s) and magnitudes (M_r^c > -21.5 mag). We converted the probability density to space densities by multiplying the probability density (which integrates to 1) by the sum of all the $1/V_{max}$ factors in the TF sample.

The joint distribution of the luminosity function and the velocity function (discussed in an upcoming paper) are able to constrain galaxy formation and evolution models more than a single marginal distribution (LF or VF). The linear TFR does not directly provide information about the number of galaxies at a given location in the $M_r^c - v_{circ}$ plane, whereas we provide space densities that can be compared with simulations of cosmological volumes.

When comparing a model or simulation of a galaxy with the TFR, this traditionally consists of ensuring that the produced galaxies lie on the TFR. The TFR is typically defined by the slope and offset parameters, in some cases including the scatter. Here we determined the full volume-corrected bivariate distribution, or probability distribution, in the $L - v_{circ}$ plane for the first time. This allows a much more direct and quantitative estimate of the likelihood that a simulated galaxy is consistent with the real galaxy population. The halo velocities obtained from cosmological simulations would have to be converted into the circular velocity, which can be directly compared with our results. Analysis of such a volume-complete distribution, which would require a larger sample spanning diverse environments and luminosities, however, might shed some light on the environmental influence on the TFR, as indicated by Blanton et al. (2008).

Our analysis is limited by incompleteness problems at the low-velocity or fainter magnitude end. Nevertheless, the difference in the two distributions is apparent, showing that the most luminous galaxies do not contribute significantly to the bulk of the Universe's stellar angular momentum. The space densities shown in Fig. 2.19, as well as the other data, are available online at CDS.

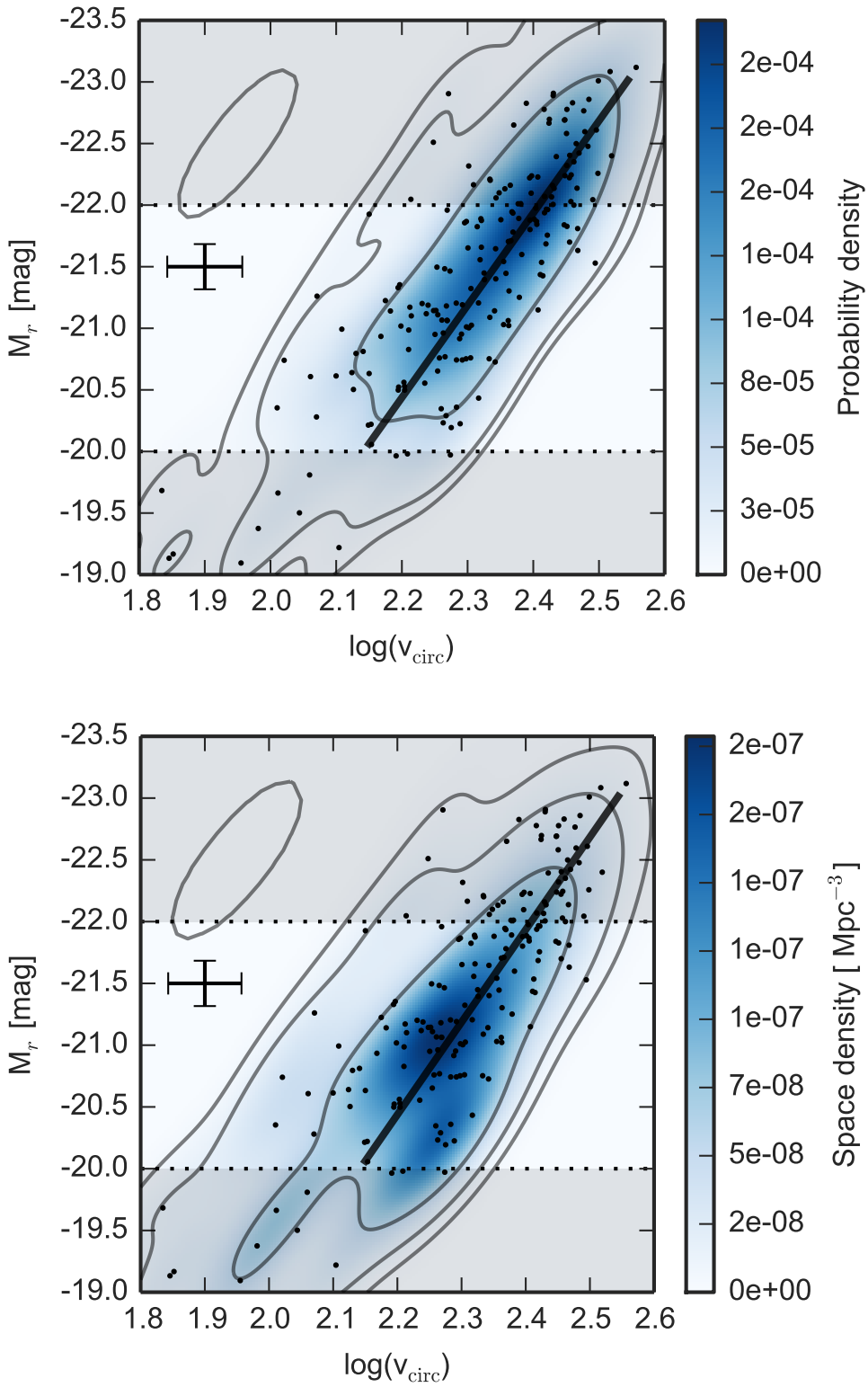

Figure 2.19: Left plot: the joint probability density of M_r^c-$v_{\rm circ}$. Right plot: the joint space densities distribution, estimated by weighting the KDE kernels by the $1/V_{\rm max}$ weights. Grey lines denote the 1, 2, and 3 standard deviation contours. The black line shows the TFR discussed in the previous section. A 1-σ contour of the Gaussian kernel used for density estimation is shown in the upper left corners. Grey shaded regions mark the regions where our sample is incomplete.

2.9 Conclusions

We presented the first space density distribution of rotating galaxies in the M_r^c-$v_{\rm circ}$ plane, derived using the CALIFA stellar velocity fields. The use of stellar IFS kinematics, careful extinction corrections, and the statistically well-understood CALIFA sample allowed us to perform volume corrections and provided a fair representation of the distribution of galaxies with -20 > M_r^c > -22 mag. Our key results are as follows.

- The velocity uncertainties in many TFR analyses are underestimated. The reason for this is a combination of direct use of photometric inclination estimates, lack of full 2D spatial information, and degeneracies between rotation curve parameters and inclination. Using consistent MCMC modelling of velocity fields, we obtained realistic velocity uncertainties, which were propagated to the further analysis.

- By avoiding any arbitrary cuts in our sample and instead modelling the TFR and non-TFR populations of galaxies, we used a reproducible, probabilistic approach to outlier rejection (Sect.2.6.2). This allowed us to generalise our analysis to other samples and let us preserve the capability of performing volume corrections.

- A $1/V_{\rm max}$-weighted linear fit with bivariate uncertainties provided an r-band TFR with slope, zeropoint and scatter equal to -7.5, -4.0, 0.03 for the $v_{\rm circ}$-based TFR and -6.7, -6.3 and 0.09 for $v_{\rm opt}$-based TFR (Sect. 2.7).

- We provided a bivariate local space density distribution in the $v_{\rm circ} - M_r^c$ plane (Sect. 2.8), which, although less straightforward to compare with than a simple linear parameterisation, provides more information than a single line and is more representative of the overall properties of galaxies. The full 2D distribution is what simulations ought to be compared with.

Chapter 3

The CALIFA and HIPASS Circular Velocity Function for All Morphological Galaxy Types

A version of this chapter was published in 2016 as "The CALIFA and HIPASS Circular Velocity Function for All Morphological Galaxy Types", S. Bekeraitė, C.J. Walcher, L. Wisotzki et al., The Astrophysical Journal Letters, Volume 827, Issue 2, article id. L36, 6 pp.

3.1 Abstract

The velocity function is a fundamental observable statistic of the galaxy population, similarly important as the luminosity function, but much more difficult to measure. In this work we present the first directly measured circular velocity function that is representative between $60 < v_{\rm circ} < 320$ km s^{-1} for galaxies of all morphological types at a given rotation velocity. For the low mass galaxy population ($60 < v_{\rm circ} < 170$ km s^{-1}), we use the HIPASS velocity function. For the massive galaxy population ($170 < v_{\rm circ} < 320$ km s^{-1}), we use stellar circular velocities from the Calar Alto Legacy Integral Field Area Survey (CALIFA). In earlier work we obtained the measurements of circular velocity at the 80% light radius for 226 galaxies and demonstrated that the CALIFA sample can produce volume-corrected galaxy distribution functions. The CALIFA velocity function includes homogeneous velocity measurements of both late and early-type rotation-supported galaxies and has the crucial advantage of not missing gas-poor massive ellipticals that HI surveys are blind to. We show that both velocity functions can be combined in a seamless manner, as their ranges of validity overlap. The resulting observed velocity function is compared to velocity functions derived from cosmological simulations of the $z = 0$ galaxy population. We find that dark matter-only simulations show a strong mismatch with the observed VF. Hydrodynamic simulations fare better, but still do not fully reproduce observations.

3.2 Introduction

The circular velocity function (VF), the space density of galaxies as a function of their circular rotation velocities, is directly related to total dynamical masses of the galaxies and not dominated by their baryonic content, unlike the galaxy luminosity function (LF) (Desai et al. 2004). As a tracer of dark matter halo masses (Zwaan et al. 2010, hereafter Z10), the VF can be used as a test of the ΛCDM paradigm (Klypin et al. 2015; Papastergis et al. 2011) and a probe of cosmological parameters (Newman & Davis 2000, 2002) or the relation between the dark matter halo and galaxy rotation velocities.

Observationally, VF differs significantly from the LF. The latter, although difficult to predict and interpret theoretically, is much easier to measure (Klypin et al. 2015) and does not depend on the spatial distribution of baryons in galaxies. Depending on the precise definition of circular velocity, the VF is a function of both the halo and baryonic mass spatial distribution and their ratio in a particular galaxy, however, it is not significantly affected by uncertainties in the stellar mass-to-light ratio. In this regard it is a superior tool for testing the results of cosmological simulations.

Measuring the VF is difficult on all halo mass scales. Cluster rotation velocities have completely different dynamical properties and require different observational methods than individual galaxies (Kochanek & White 2001), while the lowest velocity galaxy samples are not complete. Even at intermediate velocities the VF has not been fully constrained, because circular velocity measurements for gas-poor early-types, dominating the high velocity end of the galaxy velocity function, are notoriously challenging (Gonzalez et al. 2000; Papastergis et al. 2011; Obreschkow et al. 2013). Moreover, even though the circular velocity is easy to define theoretically, there is no clear observational definition, especially given that the rotation curves of some classes of galaxies do not flatten.

Several studies have attempted to use galaxy scaling relations in order to infer circular velocities from more accessible observable quantities. Gonzalez et al. (2000) estimate a VF by converting the SSRS2 luminosity function using the Tully-Fisher relation. A similar approach was adopted by Abramson et al. (2014), who construct galaxy group and field VFs using velocity estimates based on Sloan Digital Sky Survey (SDSS) photometric data. Desai et al. (2004) construct cluster and field VFs by using SDSS data, Tully-Fisher and Fundamental Plane relations.

In Klypin et al. (2015) a Local Volume VF, complete down to $v_{\rm circ} \approx 15$ km s^{-1}, was estimated using a combination of HI observations and line-of-sight velocities estimated from photometry. However, their study does not sample the velocities above ≈ 200 km s^{-1}.

An HI velocity function down to 30 km s^{-1} was directly measured from HI Parkes All Sky Survey (HIPASS) linewidths (Z10). Nevertheless, as shown in Obreschkow et al. (2013), massive, rapidly rotating, gas-poor ellipticals are systematically missing from HIPASS data. Therefore its high velocity end is very incomplete.

Papastergis et al. (2011) (P11) estimate the HI linewidth function from Arecibo Legacy Fast ALFA (ALFALFA) survey data and suggest using the linewidth function as a more useful probe of the halo mass distribusion. They also provide a VF for all types by combining their VF with the velocity function converted from Chae (2010) velocity dispersion measurements.

CALIFA is in a unique position with its well-understood selection function, a wide field of view and the first IFS sample that includes a large number of galaxies with diverse morphologies. As described in Krajnović et al. (2008), 80% of early-type galaxies can be expected to have a rotating component. The use of stellar kinematics enables us to include gas-poor, rotating early-type galaxies in a homogeneous manner. Therefore we are able to directly measure the VF for rotating galaxies of all morphological types, in contrast to the inferred VFs reported by Gonzalez et al. (2000); Desai et al. (2004); Chae (2010); Abramson et al. (2014).

Within this work, we assume a benchmark cosmological model with $H_0 = 70$ km s^{-1}/Mpc, $\Omega_\Lambda = 0.7$ and $\Omega_M = 0.3$. All VFs from the literature were rescaled to this particular cosmology, as described in Croton (2013).

3.3 CALIFA stellar circular velocity measurements

CALIFA observations use the PMAS instrument (Roth et al. 2005) in PPaK (Verheijen et al. 2004) mode, mounted on the 3.5 m telescope at the Calar Alto observatory. The CALIFA survey, sample and data analysis pipeline are described in detail Sánchez et al. (2012); Husemann et al. (2013); García-Benito et al. (2015); Walcher et al. (2014). We refer the reader to the first paper of the CALIFA stellar kinematics series (Falcón-Barroso et al., submitted) where the kinematic map extraction and sample is described in full detail.

In this analysis, we use the "useful" galaxy sample defined in Bekeraitė et al. (2016, B16) and the circular velocity measurements obtained therein. Briefly, we start with the initial statistically complete sample of 277 available stellar velocity fields, 51 of which were not useful for further analysis due to S/N issues (low number of Voronoi bins, foreground contamination) or extremely distorted velocity fields. The final sample consisted of 226 galaxies. As shown in B16, the rejected galaxies were predominantly fainter (SDSS $M_r > -20$ mag), which affected the lower completeness limit but did not introduce bias in the sample above it.

We then fit the position and rotation curve parameters by performing Markov Chain Monte Carlo (MCMC) modelling of the velocity fields. The rotation velocity $v_{\rm opt}$ was estimated by evaluating the model rotation velocity at the 80% light radius (the optical radius). Due to CALIFA's large but still limited field of view rotation curve extrapolation was necessary for 165 galaxies.

We do not split the galaxy sample into ellipticals and spirals to estimate their $v_{\rm circ}$ values separately. Instead, as described in Sec. 4.4 of B16, a correction estimated in Kalinova et al. (submitted) has been applied to all galaxies. Kalinova et al. (submitted) analyse the relationship between dynamical masses inferred using the classical ADC approach (see Chapter 4, Binney & Tremaine 2008) and axisymmetric Jeans anisotropic Multi-Gaussian (JAM) models applied to stellar mean velocity and velocity dispersion fields of 18 late-type galaxies observed with the SAURON IFS instrument. We utilise the relation provided in their Table 4 and calculate the circular velocities by multiplying the measured velocity by the square root of the factors provided, based on the ratio between the $v_{\rm opt}$ and the line-of-sight stellar velocity dispersion at the optical radius. We demonstrate that the obtained circular velocity is comparable with ionised gas rotation velocity in B16.

3.4 Results

3.4.1 CALIFA circular velocity function

We measure the CALIFA stellar circular VF $\Psi_{\rm circ}$ in the same manner as the LFs in Walcher et al. (2014, W14) and B16, estimating the optimal number of velocity bins using Scott's Rule (Scott 1979). The $1/V_{\rm max}$ weights, corrected for cosmic variance as described in W14 are assigned to each galaxy and then used to calculate the VF. We note that the uncertainties correspond to Poissonian errors in each bin only and do not include any uncertainties in circular velocity measurements (see Sec. 3.4.2.

As can be seen in Fig.3.1, the high-velocity end of $\Psi_{\rm circ}$ lies significantly above the Z10 or P11 HI velocity functions. This was to be expected since HI surveys are blind to gas-poor massive ellipticals (Obreschkow et al. 2013). However, the CALIFA VF is below the higher-velocity end of P11 inferred VF for all galaxy types. This is not surprising given that their VF combines the observed ALFALFA VF and the velocity dispersion function of Chae (2010). Our circular VF is defined for rotation-dominated galaxies only and we do not include the velocity dispersion contribution in any way, barring the circular velocity correction described in Sec. 3.3.

At lower velocities the CALIFA VF starts to fall off rapidly and deviates from the Schechter function shape. We estimate the region where incompleteness should become important, based on the luminosity function of the sample provided in B16. We convert the luminosity completeness limits to velocity using the Tully-Fisher relation measured in B16 and find that the CALIFA VF should be complete within the velocity range of $140 < v_{\rm circ} < 345$ km s^{-1}. Such a direct conversion excludes the scatter in TFR, which causes a fall-off sooner than would be naively expected from the TFR alone. By taking the *rms* TFR scatter (0.27 mag) into account, we find that the CALIFA velocity function, as shown in Fig.3.1, can be safely assumed to be complete above 170 km s^{-1}. At the high velocity end, the CALIFA survey is limited by its survey volume as the total number of galaxies brighter than M_r = -23 expected within the survey is of the order of unity. Given the low number of galaxies at the high velocity end of the TFR, we are unable to estimate the real TFR scatter among the most massive galaxies and the subsequent onset of bias. However, conservatively adopting the *rms* TFR scatter of 0.27 mag we find that the CALIFA VF is complete at least up to 320 km s^{-1}.

3.4.2 Uncertainties

The CALIFA stellar rotation velocity measurements have significant uncertainties, resulting from limited spatial resolution of binned stellar velocity fields, limited CALIFA field of view and pressure-support dependent correction term. The circular VF is likely affected by all these factors. A broader discussion of uncertainties in the circular velocity measurements and volume correction weights is contained in B16 and W14.

In order to check the impact of velocity measurement uncertainties we employ a resampling method similar to P11. We generate 200 mock CALIFA VF samples (shown in Fig. 3.2) in which the volume weights are not changed, but the velocities $v_{\rm circ}$ are replaced with randomly drawn values such that $v_{\rm circ}^{\rm test} = v_{\rm circ} + \mathcal{N}(0, \sigma_v)$, where σ_v are the individual velocity uncertainties of each point.

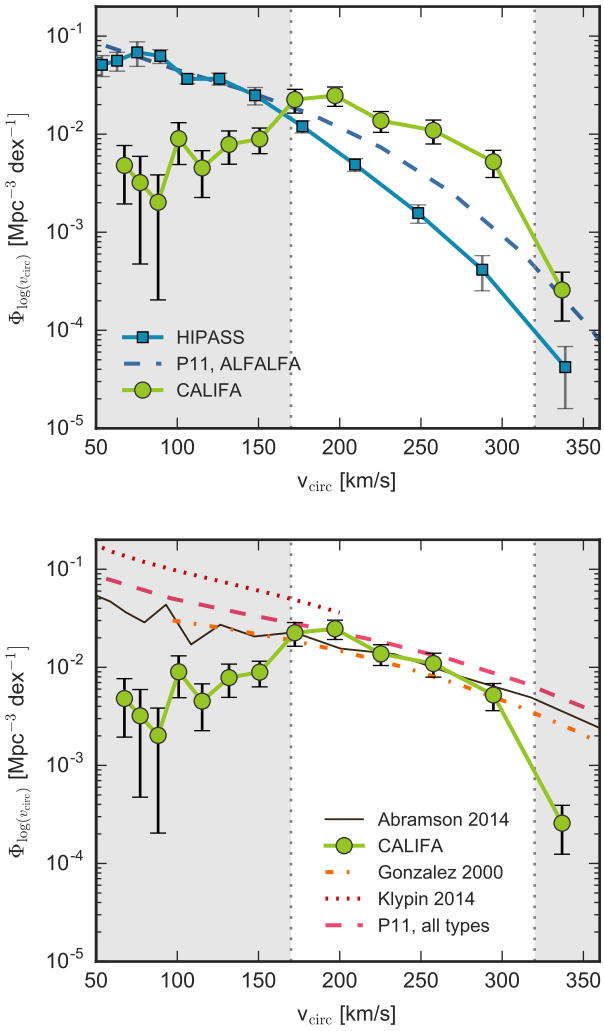

Figure 3.1: CALIFA velocity function, compared with the HIPASS (Z10), Gonzalez et al. (2000); Klypin et al. (2015); Abramson et al. (2014) and P11 measurements. The left panel shows the comparison with the observed VFs of rotation-dominated gas-rich galaxies. The right panel displays the comparison with indirectly estimated VFs. The shaded areas and dotted vertical lines show an approximate region where incompleteness in the CALIFA sample becomes important.

Overall, the effect is a smoothing of the VF as the datapoints are 'smeared' into the neighbouring bins. As the $1/V_{\rm max}$ weights are higher at the lower velocities, this leads to an artificial boost at the highest velocity end. Undoubtedly, this effect should be present in our VF as well, making the location of the highest velocity CALIFA datapoint even more uncertain. Given that this bin only includes 3 galaxies and is outside our estimated completeness range, we exclude it from all further analysis.

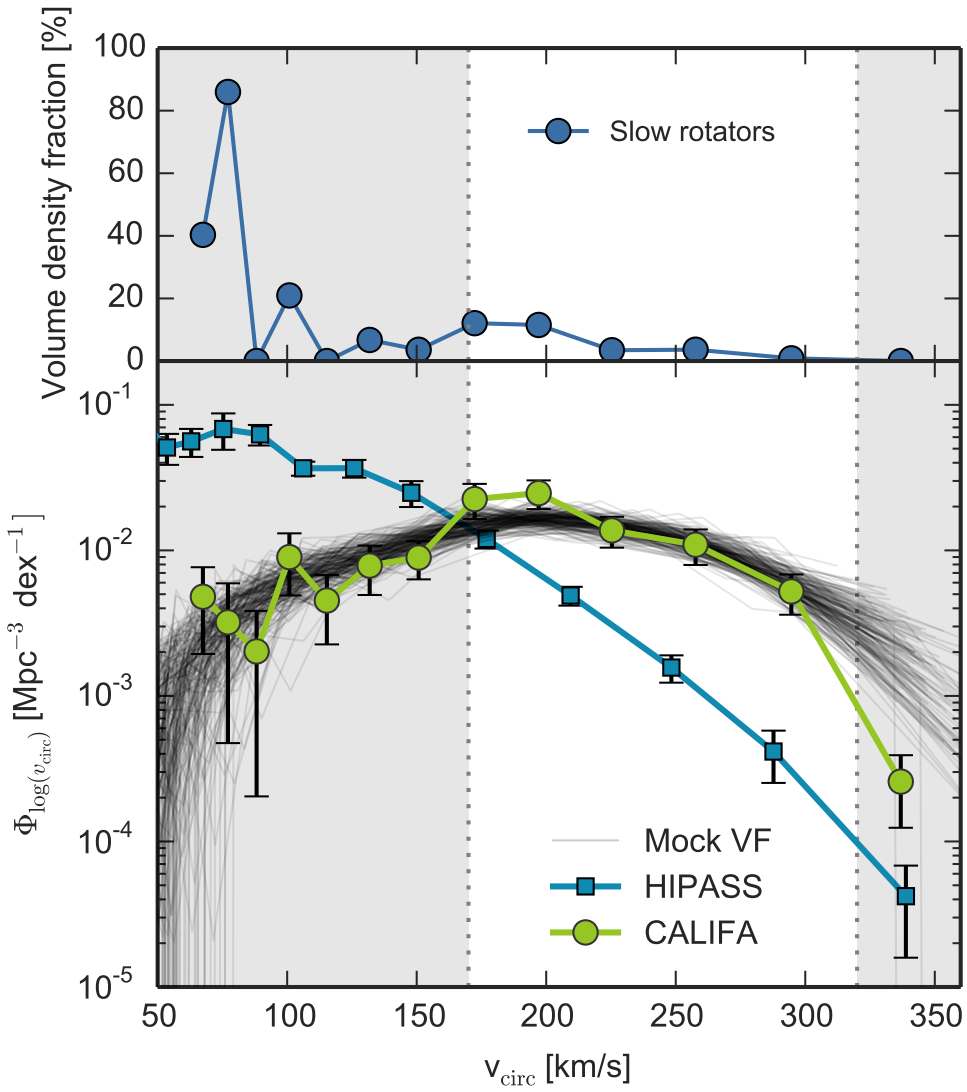

Figure 3.2: Top panel shows the volume density fraction of slow rotators (SR), for which the measured rotation velocities and circular velocity corrections are the most uncertain. This fraction does not reach 20% of volume density at for $v_{\rm circ} \gtrsim 110$ km s^{-}1. Bottom panel shows the effect of velocity measurement uncertainties on the velocity function. Thin grey lines are the mock realisations of the VF. The green points and line are the CALIFA VF. The blue line shows the HIPASS VF.

3.4.3 Combined CALIFA-HIPASS circular velocity function

In order to extend the VF to a wider velocity range we merge the HIPASS VF between 60-160 km s^{-1} and CALIFA circular velocities between 160-320 km s^{-1}, effectively choosing the more complete VF in each bin. Merging the two VFs in this way is justified as HI-rich late-type galaxies dominate the counts below 200 km s^{-1}. At the high mass limit, early-type massive rotators contribute significantly to the high velocity end, where

Table 3.1: Schechter function fit parameters for CALIFA+HIPASS VF (Eq.3.1).

Ψ_* [$\times 10^{-3}$ Mpc^{-3}]	v_* [km s^{-1}]	α
130.0±35.8	89.3±32.8	0.2±0.6

Table 3.2: CALIFA-HIPASS velocity function values.

Survey	$v_{\rm circ}$ [km s^{-1}]	$\Psi(\log_{10} v_{\rm circ})$ [$\times 10^{-3}$ Mpc^{-3}]
HIPASS	63.0	56.1 ± 12.2
	75.3	68.2 ± 19.1
	89.5	62.7 ± 10.1
	106.2	36.6 ± 4.1
	125.9	36.7 ± 5.1
	147.9	24.9 ± 5.0
CALIFA	172.4	22.5 ± 6.1
	197.1	24.7 ± 5.5
	225.4	13.7 ± 3.3
	257.7	10.9 ± 3.0
	294.6	5.2 ± 1.6

the CALIFA sample is expected to be complete at least up to $v_{\rm circ} = 320$ km s^{-1}, as described above.

We fit a Schechter function

$$\Psi(v_{\rm circ}) = \Psi_* \left(\frac{v_{\rm circ}}{v_*}\right)^{\alpha} \exp\left[-\left(\frac{v_{\rm circ}}{v_*}\right)\right] \tag{3.1}$$

to the combined VF, shown in Fig. 3.3. The datapoints are listed in Table 3.2 and the fit parameters are provided in Table 3.1. Uncertainties for the HIPASS values were taken from Obreschkow et al. (2013), where they supplement direct measurement and shot noise with other uncertainties such as distance errors, cosmology uncertainties and cosmic variance. Similarly to Z10, we find that the model parameters are highly covariant.

3.4.4 Discussion

Despite the care with which we have undertaken our analysis, combining the HI rotation velocities and stellar circular rotation velocities as we have done has some caveats.

First of all, the actual methods used to construct the HIPASS and CALIFA VFs are different. The CALIFA volume correction procedure uses a more straightforward $1/V_{\rm max}$ method (Schmidt 1968), improved by accounting for the radial density variations.

Meanwhile, Z10 employ a bivariate step-wise maximum likelihood (2DSWML) technique to obtain their space densities. Zwaan et al. (2003) verify that the method is insensitive to even large radial density variations However, the HIPASS linewidth function (WF) matches the WF obtained from the deeper ALFALFA survey down to 60 km s^{-1} (P11), confirming that the effect of large scale structure on the HIPASS VF is

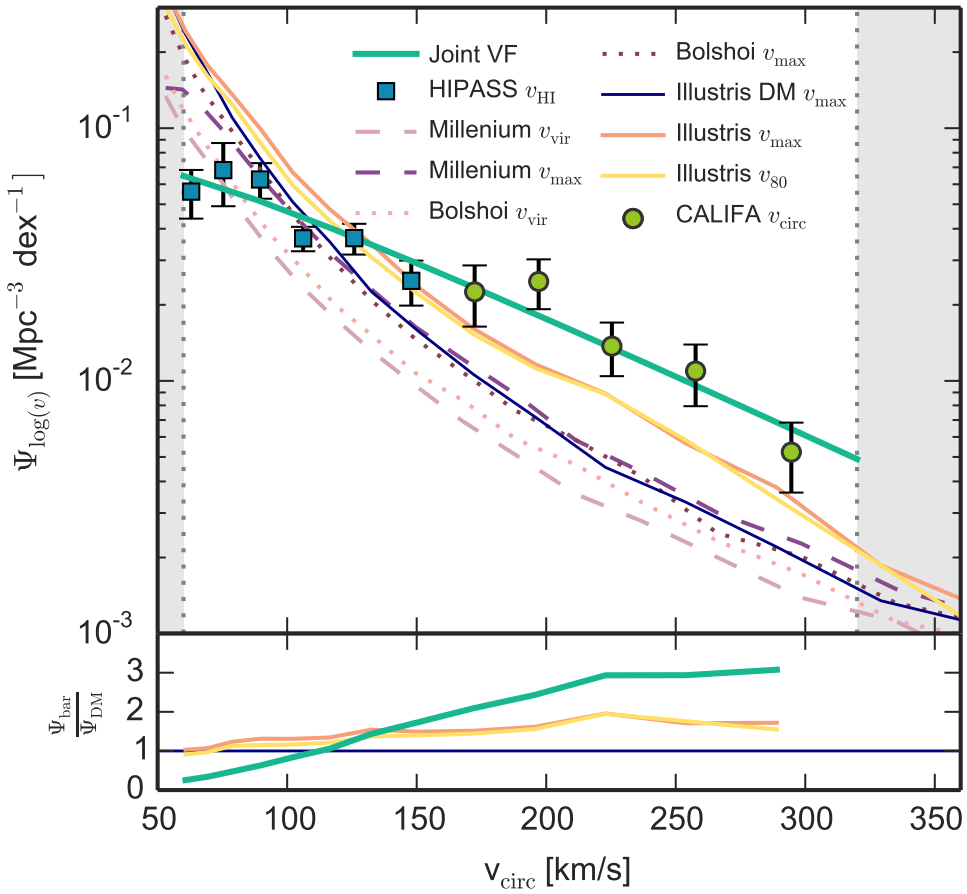

Figure 3.3: Zoomed-in view showing the combined CALIFA+HIPASS VF and the best Schechter fit, shown as thick solid teal line. In the top panel, dark matter-only halo VFs from Millenium and Bolshoi simulations are shown as purple and pink dashed and dotted lines. $v_{\rm max}$ VF from Illustris-1 dark-matter only simulation is shown by a thin dark blue line. Full-physics Illustris-1 simulation VFs, calculated using the subhalo $v_{\rm max}$ and circular velocity at 80% stellar mass radius (v_{80}) are displayed as orange and yellow solid lines respectively. The lower panel shows the ratio between the baryonic simulated VFs, the combined CALIFA+HIPASS fit and the DM-only Illustris VF. See Sec. 3.4.5 for a description, discussion, and references.

negligible, at least in the range of our analysis. As shown in Zwaan et al. (2003), the $1/V_{\rm max}$ and 2DSWML methods yield practically indistinguishable results, confirming that the two VFs derived using both methods are compatible.

The HIPASS sample consists of late-type galaxies only, since visually classified early-type galaxies, comprising 11% of the sample, have been removed. However, the fraction of early-type and S0 galaxies is reported to only have a noticeable effect on the VF only for galaxies with rotation velocities above 200 km s^{-1}, where we use CALIFA VF values already.

HIPASS linewidths have been corrected for inclination using SuperCOSMOS imaging b-band photometric axis ratios (Meyer et al. 2008), while we use kinematic inclinations obtained from MCMC modelling of the 2D velocity fields. Photometric inclination estimates are systematically affected by unknown intrinsic disk thickness, choice of b/a measurement radius and any departure from a perfect circular disk shape. However, given that Z10 exclude galaxies with estimated inclinations $i < 45°$due to larger uncertainties at low inclinations, inconsistencies in inclination measurements are unlikely to have had a significant effect.

As discussed in Z10, HIPASS may not detect HI at the flat part of the rotation curve for all galaxies, especially those with $v_{\rm circ} \leq 60$ km s^{-1}. Similarly, a small fraction of low-mass galaxies might not have enough gas to have been detected by HIPASS. We treat the lowest VF end with caution, and exclude HIPASS datapoints below 60 km s^{-1} from the combined fit. Therefore, the joint velocity function should be representative in the velocity range of $60 < v_{\rm circ} < 320$ km s^{-1}.

3.4.5 Comparison with simulations

We compare our work with a number of simulations. Shown in Fig. 3.3 are the VFs from the Millennium (Springel et al. 2005) and Bolshoi (Klypin et al. 2011) dark matter simulations. Here we are plotting friends-of-friends DM halos using two different halo circular velocity definitions: virial velocity $v_{\rm vir}$ and maximum circular velocity $v_{\rm max}$. In addition, we show the Illustris-1 DM-only run $v_{\rm max}$-based VF, constructed for haloes with $M_{\rm DM} > 10^{10} M_{\odot}$.

We also include two VFs measured from Illustris-1 full-physics simulations (Vogelsberger et al. 2014a,b). Illustris $v_{\rm max}$ is calculated for all subhaloes with stellar masses $M_* > 10^8 M_{\odot}$, while Illustris v_{80} is calculated as the gravitational potential-induced circular rotation velocity at the 80% stellar mass radius.

It is strikingly evident that the observed VF does not agree with the dark matter-only simulations, even though the low velocity end of Bolshoi and Millenium simulations displays marginal agreement with the observational data. At intermediate velocities the dark matter-only VFs sit well below both the observed data and the baryonic simulation.

However, we find that the observed VF cannot be reconciled with the Illustris v_{80} and $v_{\rm max}$-based VFs, though the full physics simulations produce VFs that are significantly closer to the observed VF. The lack of observed galaxies is evident for velocities lower than $v_{\rm circ} \approx 120$ km s^{-1}. This fact was already shown in Gonzalez et al. (2000); Papastergis et al. (2011); Abramson et al. (2014) and Z10, however, we find it worthy to revisit their results using the latest hydrodynamical simulation results.

Interestingly, at the intermediate velocities the predicted VFs are systematically offset from the observations, differing by up to a factor of 3. This discrepancy is not related to the "under-abundance" problem.

The mismatch between simulations and observations is either a result of an inconsistency in the way that observations and simulations are measuring the velocity function, or the structure of simulated galaxies is inconsistent with the structure of observed galaxies. We have not yet performed a fully fair comparison between the simulations and observations using the 80% light radius in both cases, employing adequate surface

brightness cuts and including projection effects for the simulation. In the very recent paper by Macciò et al. (2016) it was shown that at least some of the tension between the data and models at the low end of the velocity function can be alleviated by considering finite extent of HI disks and relatively larger vertical velocity dispersion. Observational confirmation of their result would go a long way towards explaining the tension in the VF comparison at low circular velocities. We additionally note that while the Illustris VF does not fully match the observed data at high circular velocities, further study of the effects of baryons on the masses and structure of dark matter halos may close the remaining gap. The difference between observed and simulated VF should be considered to be a constraint on the future generations of galaxy formation models.

3.5 Conclusions

In this work we measure the CALIFA stellar VF, derived from a sample of 226 stellar velocity fields. To our best knowledge, it is the first directly measured VF that includes early-type fast rotators as well as late-types.

We then combined this VF with the HIPASS VF to obtain the first directly measured velocity function that simultaneously covers a wide range of circular velocities and morphological types. This has the benefit of using the space density and velocity data measured from the same surveys, without assuming scaling relations or conversions between kinematic observables. The combined VF is complete in the range of $60 < v_{\rm circ} < 320$ km s^{-1}. We find that Illustris simulation VF does not reproduce the observed data in both the low and high velocity ranges.

The differences between ΛCDM predictions and the observed VF are not so dissimilar to those found when comparing the halo and stellar mass functions. There, physical processes important for galaxy formation cause a decoupling of the halo and galaxy growth. By highlighting similar discrepancies, this work opens a new window for comparison with theory that should deepen our understanding of galaxy evolution. The resulting velocity function is expected to provide constraints on galaxy assembly and evolution models, insights into baryonic angular momentum, help improve halo occupation distribution and semi-analytic disk formation models.

Chapter 4

Combining SAMI IFU data with HI linewidths for precision angular momentum measurements

4.1 Introduction

The mass and angular momentum are fundamental properties of galaxies, determining, among other observable properties, their morphologies (Fall 1983; Romanowsky & Fall 2012) to a large degree. A relation linking the specific baryonic angular momentum j_b, baryonic mass and bulge/disk ratio has been suggested by Obreschkow & Glazebrook (2014), based on accurate j_b measurements of 16 nearby spiral galaxies from the THINGS sample. This relation is claimed to be the 'Fundamental Plane for spirals', the basis of Tully-Fisher, size-luminosity and size-rotation velocity relations observed as projections.

Obreschkow & Glazebrook (2014) measure baryonic specific angular momentum -baryonic mass - bulge/total ratio (B/T) (j_b - M_b - β) distribution using deep HI velocity maps (covering up to 10 R_e) of 16 spiral galaxies from The HI Nearby Galaxy Survey (THINGS, Walter et al. 2008) and their stellar mass and gas surface densities published in Leroy et al. (2008).

In Obreschkow & Glazebrook (2014), THINGS galaxies have j_b measured down to 10-13% level. However, a larger, morphologically diverse sample is necessary in order to investigate the j_b - M_b - β distribution for all types of galaxies. In addition, the sample should provide the opportunity to perform volume corrections so that a volume-complete plane equation could be obtained using methods similar to those described in Robotham & Obreschkow (2015).

In order to precisely measure the specific stellar angular momentum of a galaxy, the shape of the rotation curve must be well constrained at all radii. A significant amount of j_* is included within the rising part of the rotation curve (see Fig. 4.1), therefore we need accurate rotation velocity measurements at radii before the turnover point. Respectively, the total amplitude of the rotation curve can be well constrained by HI measurements at large radii as HI gas is expected to be a cold dynamical tracer of the underlying potential. Combining SAMI 2D velocity fields (with a median sampling of

$1.7r_e$) with available ALFALFA survey (Giovanelli et al. 2005; Haynes et al. 2011) HI linewidths could allow precise measurements of j_* for large samples of galaxies without the need of deep spectroscopy with high spatial resolution.

Our final goal is to have precise j measurements for a large sample of galaxies, sampling the $M_\odot - B/T$ space well and therefore constraining the M_* - morphology - j relation (Obreschkow & Glazebrook 2014). One assumption we are making here is that stars are co-rotating with gas. This is, of course, not strictly valid given that stars are much a hotter dynamical component. However, as shown in Obreschkow & Glazebrook (2014), for disks of late type galaxies this assumption is justified. In any case, stellar rotation curves can be used to constrain j_* or corrections relating the stellar rotation to the circular rotation velocity can be made (Weijmans et al. 2008). Full treatment of this issue is beyond the scope of this feasibility study, which aims to explore the merits of such an approach for a limited sample of galaxies with available observations.

4.2 Feasibility tests using the THINGS data

In order to test several assumptions of our approach we employ the THINGS dataset together with their stellar mass surface density data. First of all we check, in a similar manner to the test described in (Obreschkow & Glazebrook 2014), if the measured and analytically fit quantities converge within the measurement radii. To test that, we fit a simple exponential model

$$v(r) = V_c * (1 - e^{-\frac{r}{r_{flat}}}) \tag{4.1}$$

to the measured rotation curve, where r_{flat} is the turnover radius and V_c is the velocity at the flat part of the rotation curve. The stellar mass surface densities were modelled as double exponents (see Fig. 4.2). We check whether deviations from idealised formulae, such as the spiral arms or irregularities in rotation curves are important, and find that they to not significantly affect the convergence of j_*.

Our data, of course, would not sample the rotation curves at these radii. The SAMI observations would hopefully cover the galaxy velocity fields to up to the turnover point, whereas HI W50 would be a single point at a large radius. In order to test whether we could constrain the rotation curve even with incomplete spatial coverage, we try to fit the simple exponential model described above to the THINGS rotation curves with datapoints at various radii removed. Fig.4.3 shows the measurements for a galaxy that is well sampled up to 1 effective radius and then has a single datapoint at a very large radius. The calculated and fit quantities match quite well, with the difference attributed to the stellar surface density fit. As might be expected, small variations in the Σ profile lead to large differences in the total mass, especially outside the inner regions of the galaxies.

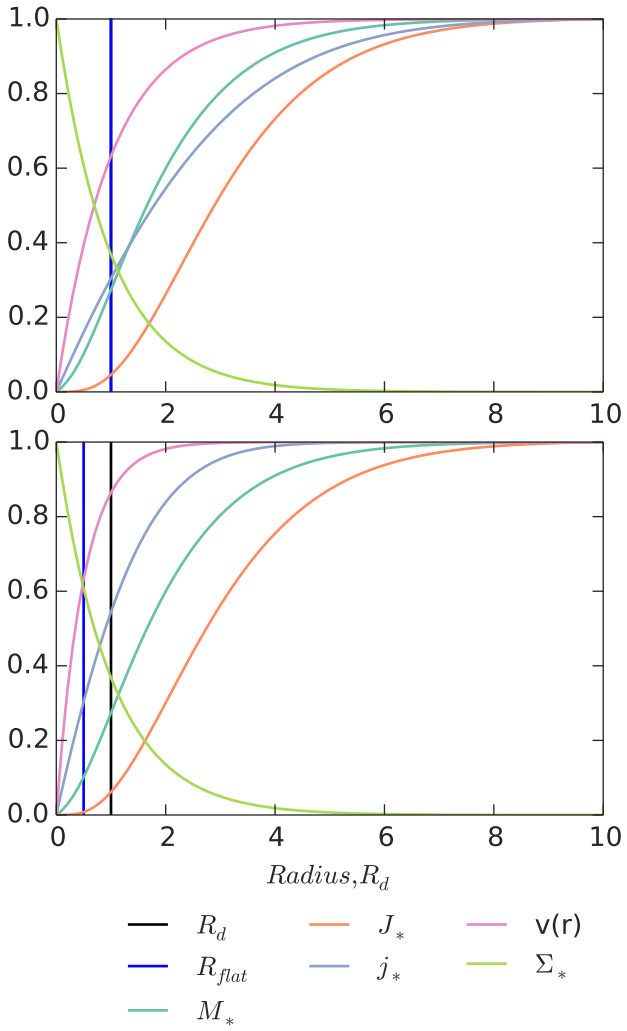

Figure 4.1: Analytical models of physical parameter convergence for two cases with different ratios of the effective radius R_d and the scale radius of flat rotation curve R_{flat}. In the top panel, the two are equal, wherein R_{flat} is twice as large as R_d in the bottom panel. All quantities are normalised to arbitrary units. The rotation curve is shown as pink line, stellar mass profile is the dark teal line, surface brightness is chartreuse, specific stellar angular momentum j_* is indigo line and the total angular momentum is orange. Disk scale radius is shown as a black solid line, while the rotation scale radius is shown as blue. The plot shows that a significant fraction of the specific angular momentum is contained before the flattening of rotation curve. In our idealised case, this depends on the ratio R_d/R_{flat}.

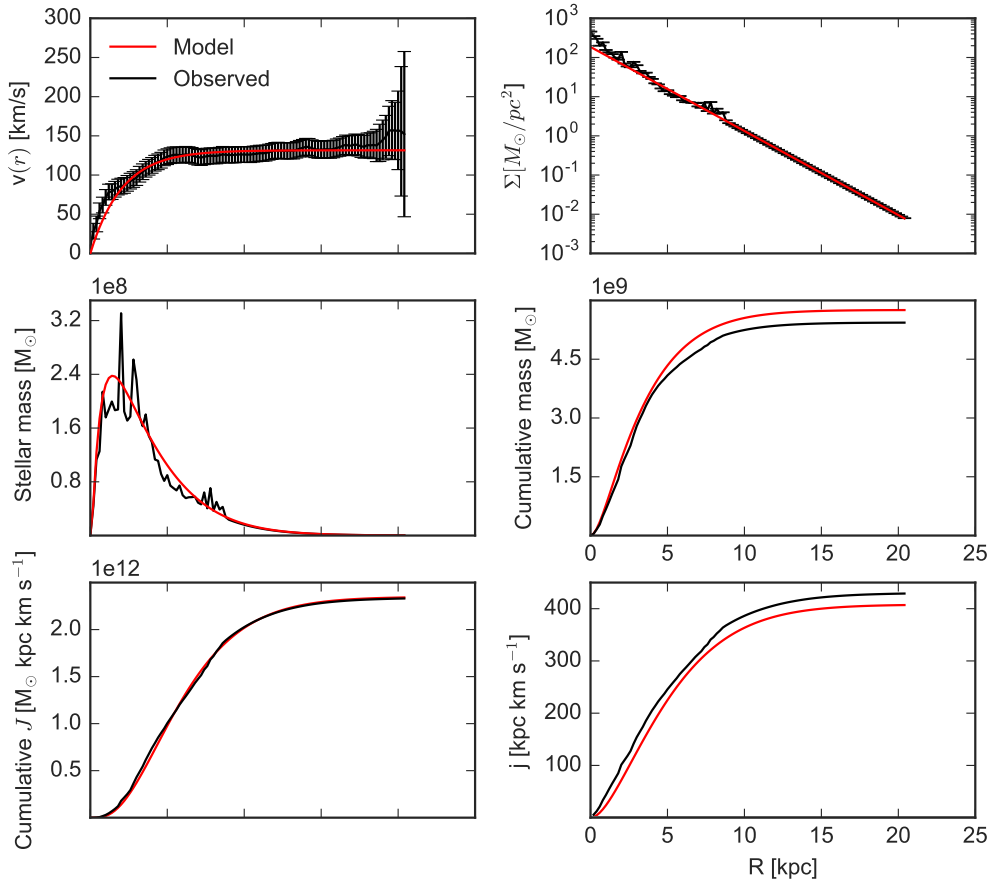

Figure 4.2: Testing model and fitting assumptions using THINGS HI rotation data of NGC 2403. Top left: exponential rotation curve fit (see text) is shown in red. Top right: double-exponent fit of the stellar surface density profile. Middle left: Stellar mass profile, calculated from the measured stellar mass surface density and from the double exponential model. Middle right: cumulative stellar mass. Bottom left: cumulative angular momentum. Bottom right: specific angular momentum.

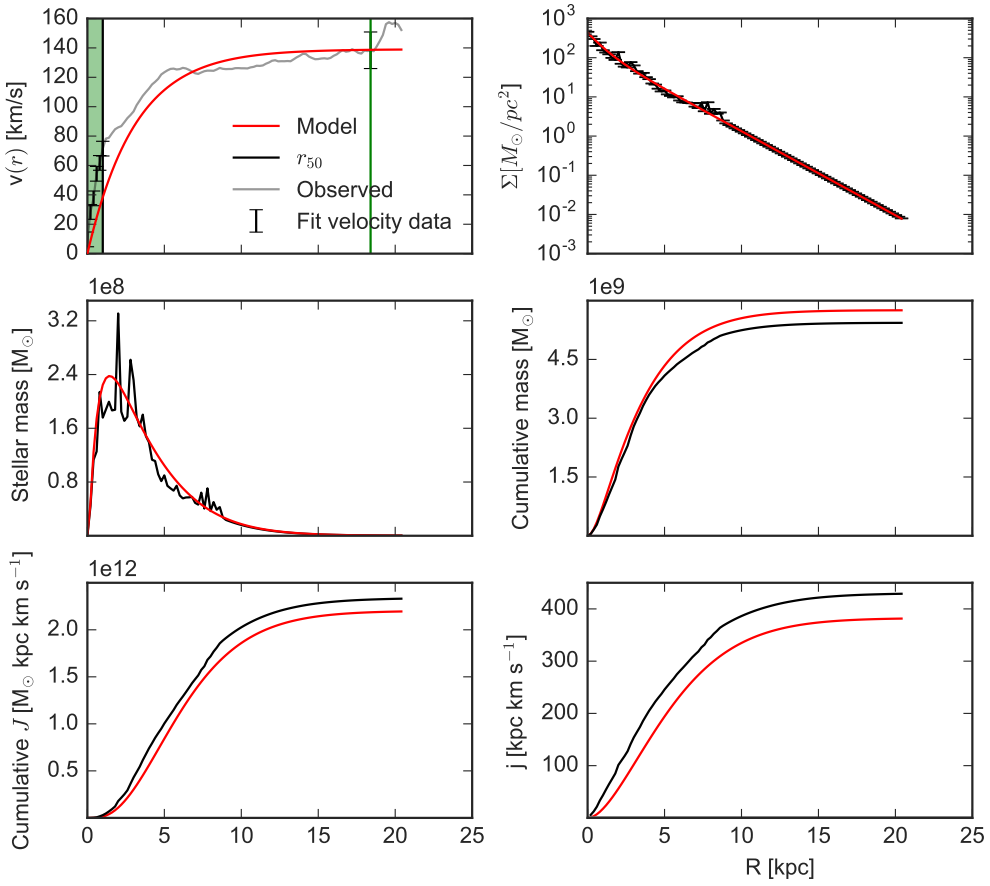

Figure 4.3: Testing the feasibility of using not entirely sampled rotation curve data with THINGS HI rotation data of NGC 2403. All rotation curve data between one effective radius and a single datapoint at 18 kpc were removed.

4.3 Observations and sample

SAMI (Croom et al. 2012; Bryant et al. 2015) is a large ongoing IFU survey that has been aiming for 3400 galaxies observed using the Sydney-AAO Multi-object Integral-field spectrograph (SAMI) mounted on the Anglo-Australian Telescope (AAT). The sample (Bryant et al. 2015), selected from the GAMA survey, spans the redshift range of 0.004 < z < 0.095 and stellar masses between 10^7-10^{12} $M_\odot$. SAMI observes 12 galaxies simultaneously, using hexagonal fiber bundles each containing 61 optical fiber with approximately 1.6" in diameter. It covers two spectral intervals: 3700 - 5700 Å with R≈1750, and 6250-7300 Å having R≈4500.

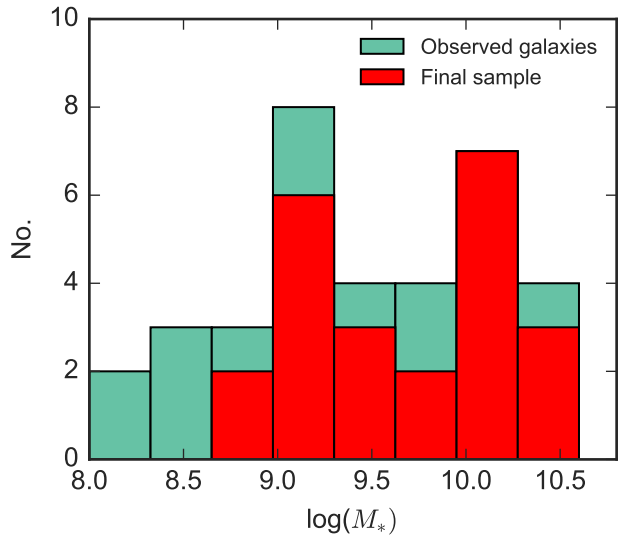

Figure 4.4: Stellar mass distributions of the initial and the final samples of SAMI galaxies with ALFALFA observations.

We cross-matched ALFALFA optical counterparts with the SAMI target catalogue (Bryant et al. 2015), requiring that the objects were within 1" in ra and dec and their redshifts would match within 0.005. There were 203 overlapping galaxies, 35 of which had available SAMI data (LZIFU v.0.8 emission line velocity fields) as of October 2014, when this analysis was started.

We selected 26 SAMI galaxies with reasonable quality ALFALFA data from this initial sample. The 10 rejected galaxies (GAMA 91924, 238085, 238164, 301098, 345646, 388603, 422907, 514260, 593645, 623726) were either late type spirals or irregulars with little or no ordered rotation, or face-on galaxies whose velocity fields were impossible to fit.

4.4 Fitting the velocity fields

The observed SAMI velocity fields were fit using an adaptation of the Bayesian MCMC approach described in more detail in Bekeraitė et al. (2016). We used a simple expo-

nential model (Eq. 4.2) to fit the rotation curves:

$$v(r) = v_0 + v_{asympt} * (1 - exp(-1 * \frac{r}{c \cdot r_{50}}), \tag{4.2}$$

where v_{asympt} is a free parameter determining the amplitude of the rotation curve, c is a free parameter describing the sharpness of turnover, r_{50} is the optical half-light radius. v_0 is the recession velocity: even though the SAMI velocity fields had already had the recession velocity $v_0 = cz$ subtracted, we found it useful to allow the v_0 to be a small free parameter. In addition, the galaxy is allowed to have arbitrary inclination and position angles. We do not allow the kinematic center position to vary due to limited spatial resolution. This rotation curve model is not suitable for rising or falling rotation curves, however, since our assumptions are valid for disks only, we use it in this study in order to avoid further parameter degeneracies.

We have prior knowledge of the v_{asympt} of these galaxies from the ALFALFA W50 data, and combine it with the IFU data-based rotating disk model. Of course, additional complications arise due to the fact that both quantities (W50 and V_c) are observed in projection. In order to remedy this, we also use GAMA photometric inclination estimate-based prior on inclination i. The GAMA inclination estimates were obtained by the SAMI collaboration from photometric Sersíc decompositions of the r-band GAMA images. The prior has a truncated Gaussian shape, with the mean $\mu = cos(i_{GAMA})$, $\sigma = 0.1$ and cutoff at $\sigma \pm 0.5$.

The final log-likelihood function can be expressed as

$$\ln\ \mathcal{L} \propto -0.5\Sigma[\frac{(V_c - v_{model})^2}{v_{err}^2}] + Prior \tag{4.3}$$

We test three models: fitting the velocity fields without a prior, a Gaussian prior based on GAMA inclination estimates (cos i) and a combination of the inclination prior and a truncated Gaussian prior based on inclination-corrected W_{50}. The width of the Gaussian prior is equal to $\sigma = 10 + err_{HI}$ km/s, where err_{HI} is half of the inclination-corrected ALFALFA HI linewidth uncertainty. In the latter model, we essentially constrain the model so that the asymptotic rotation velocity, or the v_{asympt} parameter of ionised gas at a large radius is close to $W_{50}/(2sin(i))$, i.e. half of the inclination-corrected linewidth.

After modelling, we calculate the model j value using Eq. 3 from Obreschkow & Glazebrook (2014).

The fitting results for GAMA 79635 using the no-prior model, the model with only the inclination prior and the model combining prior inclination and W_{50} information are shown at Fig. 4.5, 4.6 and 4.7, respectively. An obvious feature of the unconstrained velocity field model is the fact that the inner part of the rotation curve is fit well, yielding small residual values, however, upon a closer inspection the model parameters are not well constrained (for instance, $\Delta v_{asympt} = 447.5$ km/s, which indicates that the MCMC chains do not converge). The posterior distributions of model parameters are highly degenerate (see Fig. 4.10). The reason of these difficulties lies in the fact that the velocity field is not sampled beyond the turnover radius, meaning that models with rising rotation curve shapes(i.e. having unphysically large v_{asympt} and c values cannot be rejected. On average, models with the inclination prior do not fare much better.

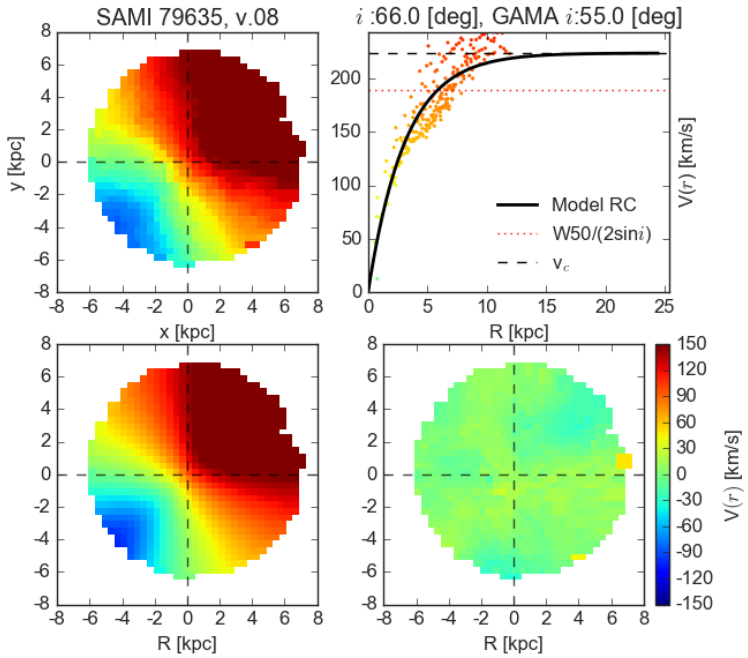

Figure 4.5: The emission line velocity field of GAMA 79635 (top left), the model rotation curve (top right), model velocity field (bottom left) and the residuals. Inclination corrected (see text) HI W_{50} value is shown as the red dotted line.

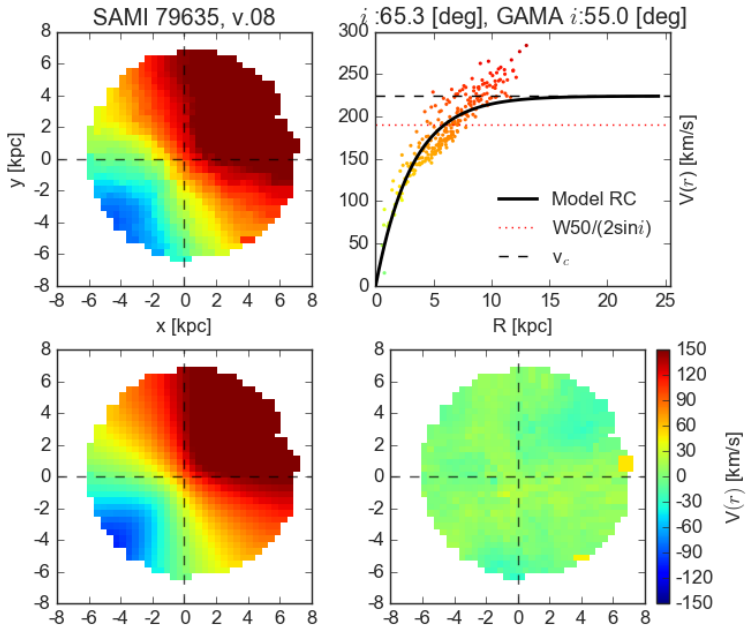

Figure 4.6: Modelling the velocity field including prior knowledge about inclination. The emission line velocity field of GAMA 79635 (top left), the model rotation curve (top right), model velocity field (bottom left) and the residuals. Inclination corrected (see text) HI W_{50} value is shown as the red dotted line.

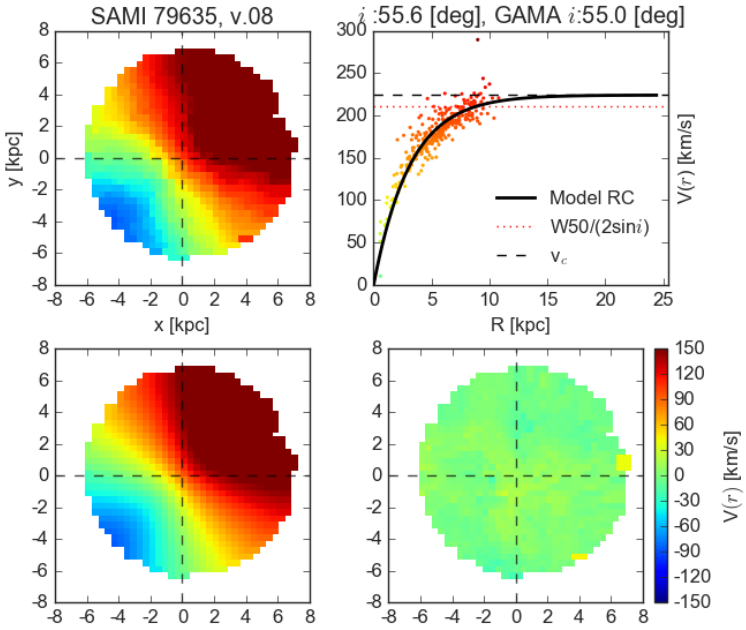

Figure 4.7: Modelling the velocity field with additional HI linewidth and inclination information. The emission line velocity field of GAMA 79635 (top left), the model rotation curve (top right), model velocity field (bottom left) and the residuals. Inclination corrected (see text) HI W_{50} value is shown as the red dotted line. The black dashed line indicates the v_{asympt} value.

On contrast, we have found that using a prior derived from the HI linewidth breaks parameter degeneracies and constrains the shape of the rotation curve as well.

The correspondence between the model v_{asympt} and ALFALFA W_{50} values is shown in Fig. 4.11. Fig. 4.9 shows the posterior distributions of j of GAMA 78667 illustrating the gains in precision. The asymptotic rotation velocity is probably better constrained by HI linewidth-based estimates, however, j measurements require not only the amplitude but also the shape of the rotation curves. In Table 4.1 we show the calculated j values together with additional information of our galaxy sample.

4.5 Discussion

This study has been intended to be a feasibility study, designed to test if combining IFU velocity fields and HI linewidth data could yield reasonable results. Although far from obtaining precise measurements (as shown in Table 4.1, the method described in this paper shows a promise significant gains in precision compared to standalone IFS or radio observations. In IFS data analysis, the λ parameter (Emsellem et al. 2007) is usually used as a proxy of j, but the trade-off between depth of observations/field of view and survey size has prevented precision j measurements for large samples. Similarly, angular momentum is best measured using resolved radio rotation curves, which is not feasible for a large number of galaxies.

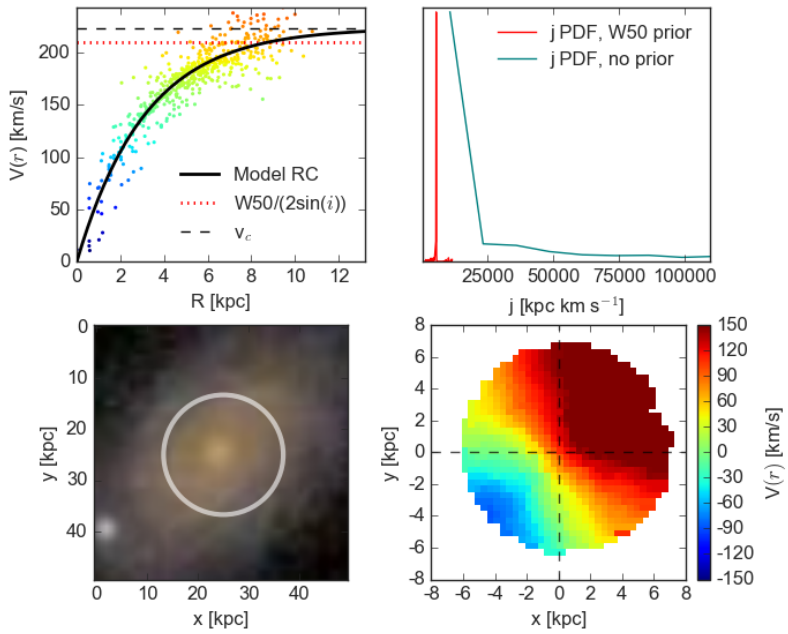

Figure 4.8: Top left: model rotation curve and data. Top right: the posterior distributions of j of GAMA 78667 for the no-prior and inclination/linewidth prior models. j PDFs are normed to the same y-scale. Bottom: a cutout view of the galaxy, with the SAMI hexabundle superimposed, and the observed velocity field.

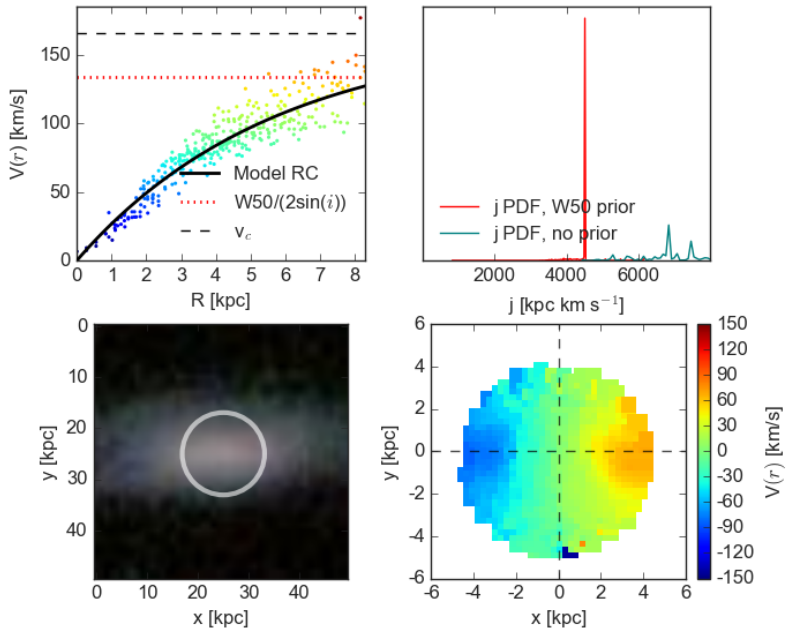

Figure 4.9: Same as above, for GAMA 239376.

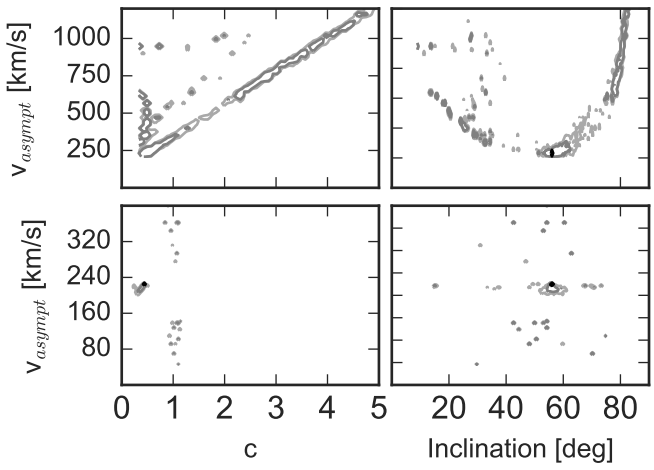

Figure 4.10: Joint probability density functions of inclination - v_{asympt} and c - v_{asympt} of GAMA 79635 for a model without any prior (top) and with a W_{50} and inclination prior (bottom). Note the different v_{asympt} scales between the top and bottom panels.

Our approach combines the available data in a statistically sound way, and shows that it is possible to constrain the rotation curves even when a part of spatial information is missing. Although our assumptions are valid for exponential disks only, in further work the method could be expanded to include galaxies with bulges or rotating ellipticals as well.

With more stringent sample selection criteria (for instance, requiring a specific coverage of the IFU velocity field, rejecting disturbed, interacting and face-on galaxies), more sophisticated rotation curve and mass distribution models and detailed analysis of the posterior j distributions, it will be feasible to obtain j measurements for large survey samples of galaxies, probing new regions of galaxy parameter space. If the sample selection is such that the statistical properties of the whole galaxy population are preserved, the relation between the specific baryonic angular momentum, baryonic mass and morphology could be evaluated, offering deep insights into formation and evolution of galaxies.

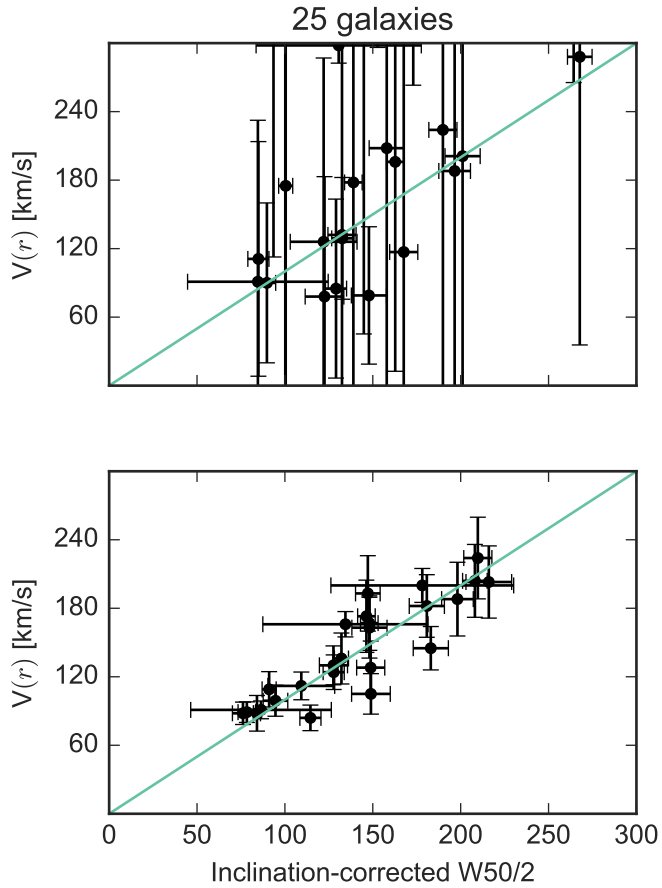

Figure 4.11: v_c vs. inclination-corrected HI linewidth without a inclination prior (top) and with both inclination and linewidth-based priors (bottom).

Table 4.1: Main properties and measured j values of analysed galaxies. The Δj values are standard deviations of the posterior j distributions.

GAMA ID	M_*	r_{50} [kpc]	v_{asympt} [km s^{-1}]	c	j [kpc km s^{-1}]]	Δj
15218	9.11e+00	9.3	124	0.79	1.78e+03	2.63e+02
77754	1.05e+01	7.0	163	0.25	7.34e+02	5.24e+02
78667	1.02e+01	6.8	193	0.93	2.71e+03	1.46e+03
79635	1.05e+01	9.1	224	0.43	1.94e+03	1.09e+03
105962	8.96e+00	6.0	88	0.84	9.02e+02	1.62e+02
106376	1.03e+01	8.5	105	0.55	1.57e+03	7.03e+02
106389	1.02e+01	6.0	203	0.60	1.67e+03	6.43e+02
106717	1.02e+01	5.2	173	0.39	9.07e+02	8.29e+02
215292	1.01e+01	5.7	182	0.29	8.01e+02	7.44e+02
216843	9.26e+00	7.7	91	0.55	8.26e+02	1.79e+02
238395	9.87e+00	4.1	167	0.89	1.37e+03	3.74e+02
239376	9.58e+00	7.9	166	1.30	3.06e+03	2.18e+02
279917	9.32e+00	9.8	88	1.01	1.54e+03	4.15e+02
318936	8.90e+00	6.8	89	0.81	9.65e+02	2.85e+02
319381	1.03e+01	12.2	188	0.47	2.46e+03	1.05e+03
383283	9.16e+00	4.4	112	0.93	7.97e+02	2.21e+02
383318	9.92e+00	9.6	99	0.66	2.19e+03	1.15e+03
388451	8.43e+00	7.2	84	0.46	5.87e+02	2.33e+02
422355	9.26e+00	5.1	145	0.47	7.07e+02	3.24e+02
422366	9.62e+00	8.9	130	0.51	1.36e+03	6.22e+02
422933	1.02e+01	6.4	204	0.64	1.84e+03	8.47e+02
593680	1.04e+01	11.5	200	0.34	1.63e+03	6.85e+02
619105	9.68e+00	12.5	128	0.52	1.79e+03	6.76e+02
620098	9.03e+00	8.6	136	0.75	1.58e+03	7.33e+02
622744	9.16e+00	5.4	109	2.14	2.09e+03	3.07e+02

Chapter 5

Conclusions and outlook

5.1 Conclusions

In this thesis we present the main scientific results and methods developed during the course of PhD studies. They mostly concern the various facets of distribution of angular momentum in galaxies, starting with indirect proxy (the Tully-Fisher relation) and finishing with a feasibility study of direct measurement of specific angular momentum for large IFU samples. The overarching themes of this work are attention to statistical completeness of input samples, universal results (i.e. derivation of volume complete galaxy property distributions) and synergy of IFU observations with other methods, e.g. imaging and radio observations.

The introduction presents the context of this study and CALIFA sample classification work done during the PhD studies within the CALIFA collaboration.

In the second chapter we present the volume-corrected distribution of galaxies in absolute magnitude-circular velocity plane, measured from CALIFA (Calar Alto Legacy Integral Field Area) survey stellar velocity fields. Such a distribution, being a joint distribution of the velocity function and the luminosity function, could provide stricter constraints on galaxy formation and evolution models than the luminosity function alone. Two novel features presented in this work are MCMC-based fitting of the velocity fields, offering a robust way to estimate the measurement uncertainties, and incorporation of the CALIFA sample volume weights in the final distribution, providing an unbiased view into the properties of the galaxies in the Universe. We suggest that this 2D distribution is what the simulations might be compared with.

Throughout the third chapter we discuss one of the two measured marginal distributions of fundamental galaxy properties – the velocity function – in more detail, given that it is the first directly measured velocity function that includes galaxies of all morphological types. We also combine the CALIFA velocity function with the HIPASS HI VF in order to obtain a directly measured VF available over a wide rotation velocity range and including all morphological types of galaxies relevant at a given rotation velocity. By comparing our VF with dark-matter only and baryonic simulations, we find that even full-physics simulations do not reproduce the VF, diverging at both high- and intermediate-velocity ends. This mismatch either suggests that the comparison between simulations and the observed galaxies is not entirely adequate, or that the simulated galaxies have a different structure than the observed ones. Further work from both the-

oretical and observational standpoints may help to clarify this problem. However, the published joint HIPASS-CALIFA VF can already be used as a constraint on galaxy formation models.

In the following chapter we present a method of precision specific angular momentum measurements combining IFS and HI linewidth data, developed in collaboration with D. Obreschkow (ICRAR). We attempt to improve the precision of specific angular momentum measurements by statistically combining 2D velocity field measurements and ALFALFA HI linewidths of several SAMI galaxies. It is a feasibility study demonstrating the possibility of measuring specific angular momenta of a large number of galaxies without deep individual radio observations. We find that even by using undersampled rotation curves obtained by combining IFU velocity fields reaching out up to 1.7 R_e with a HI-linewidth based prior, we can constrain galaxy rotation curve shape.

5.2 Outlook

The methods developed or applied in the thesis are not limited to the topics investigated within it and can be applied for a wide range of investigations outside the scope of this work and for several large-scale integral field surveys that are currently ongoing or at the planning stage, such as MANGA (Mapping Nearby Galaxies, Bundy et al. (2015)), SAMI (Sydney-AAO Multi-object Integral Field Spectrograph, Croom et al. (2012); Bryant et al. (2015)), HETDEX (Hobby-Eberly Telescope Dark Energy Experiment, Hill et al. (2008)).

The Bayesian velocity field fitting tools developed and described in Sec. 2 could be used in and beyond galaxy kinematics research, for example, in studies of galaxy spin alignment. The fitting routines allow obtaining realistic uncertainties of fit parameters and rigorously including any prior information, such as photometric quantities or morphology. For example, posterior probabilities of spin alignments of galaxies in a volume of space could be evaluated simultaneously while taking their morphologies, different impact of seeing and redshift space distortions into account.

The well-defined selection criteria of CALIFA sample enabled us to obtain the volume-complete distributions of statistical properties of galaxies. In this work, we only calculated two distributions, or rather one 2D distribution ($M_r - v_{circ}$) and investigated one of its marginal distributions, the velocity function. The application of volume corrections allows the derivation of space densities and distribution functions of any measurable galaxy physical property from the CALIFA sample. For instance, it is straightforward to evaluate a volume complete $\lambda_R - \epsilon$ distribution, which could yield new insights into the relation between galaxy morphology and angular momentum. Such work could be the most useful if extended beyond the massive galaxies targeted in CALIFA survey and applied to other large ongoing surveys.

The MANGA and SAMI surveys, having large and diverse samples, could benefit greatly from investigating volume complete properties of galaxies. Using their data together with proper procedures for volume corrections would yield more precise picture of galaxy statistical distributions than what could be attained in this work. Obtaining results analogous to the M_r-v_{circ} distribution or a velocity function described in the second and third chapters of this thesis could be quite straightforward and very informative, as

new regions of galaxy parameter space would be probed for the first time. In particular, both additional observational data and theoretical work/simulations are needed to help explain the discrepancy between the observed and simulated velocity functions reported in Chapter 3. Such studies, aiming to explain the difference between observations and simulations are essential tests of the LCDM model.

An immediate extension of Chapter 4, describing a feasibility study of precise angular momentum measurements using IFU velocity fields and HI linewidths would be further work using more sophisticated models of rotation curves, relaxed assumptions about galaxy brightness profiles, more realistic j calculations and expansion of such work to a wider range of morphological galaxy types. Then such analysis could be performed for a large sample of galaxies, allowing more detailed studies of the mass-angular momentum-morphology relation.

Appendix A: growth curve photometry measurements

Motivation for having independent photometry measurements

As the CALIFA sample was selected from the SDSS survey, all the CALIFA galaxies have SDSS Petrosian magnitudes. However, SDSS Petrosian magnitudes are designed to capture a fixed percentage of the total flux, and that percentage depends on the galaxy profile. As shown in Blanton et al. (2001), the Petrosian flux measurement of a large exponential disk includes virtually all the flux, however, the ratio between the total flux and the Petrosian flux of a galaxy with de Vaucouleurs profile is only ≈80%. Moreover, the SDSS Petrosian radii are based on signal-to-noise-ratio of the image, therefore flux in bands with low S/N (u, z) is underestimated, possibly affecting photometric stellar mass models.

The CALIFA survey is primarily diameter-limited and consists of galaxies with relatively large (40-80") SDSS isophotal radii. The SDSS DR7 pipeline does not always perform well for bright, large galaxies, over-subtracting the sky or picking secondary ("child") photometric components instead of the total flux measurements. Besides, all images contain foreground and background objects (stars, background galaxies, cosmic rays, image artefacts) that, if not accounted for, contribute to the error in both flux and sky value measurements.

Image preparation

Just masking nuisance objects would lead to systematic underestimation of the galaxy magnitude, because the galaxy areas under them would remain excluded from the total flux measurement. Simple interpolation would not be applicable due to the large number of missing adjacent pixels, so we chose a procedure known as inpainting – masked pixels were iteratively replaced with a Gaussian inverse-distance weighted average of the neighbouring real pixels, starting with the pixels with the largest number of nearest neighbours. In order to apply the masks provided by the collaboration, available for r band images, to the other 4 SDSS bands, we measured the shift between the different images and their *r*-band counterparts using their WCS (FITS World Coordinate System) α and δ coordinates, then shifted the masks and cropped the images accordingly.

A small number of galaxies with large masked regions yield inpainted images that were distorted and underlying brightness profiles could not be recovered. In such

cases, only flux from non-masked regions was included and an error flag added in the photometric measurements table.

The procedure

Surface photometry of galaxies is made difficult due to the fact that galaxies are extended objects without clear outer edges. Various methods have been used to measure the galaxy magnitudes, including 2D modelling of galaxy images, signal-to-noise based methods such as Petrosian magnitudes (Petrosian 1976; Strauss et al. 2002), measuring flux inside a radius limited by surface brightness, using fixed apertures, etc.

Growth curve of a galaxy is the profile of integrated magnitude shown as a function of the radius of the current aperture (Okamura et al. 1999). This aperture can and should be elliptical in general case. If the sky is subtracted accurately, this profile flattens asymptotically as the flux from the galaxy drops to zero. In a perfect case, the cumulative flux at the end of such a profile corresponds to the total flux of the galaxy.

In theory, growth curve photometry measurements are superior to the other methods mentioned, retrieving the flux of all types of galaxy profiles well and making no prior assumptions or applying arbitrary cutoffs in surface brightness level, S/N level or aperture size. It is sensitive to even small flux levels at the outskirts of galaxies. In addition, it does not depend on the global features of the image, measuring the sky level in the immediate vicinity of the galaxy. The local sky values are more accurate than the sky mean frequently used for sky subtraction, resulting in better sky subtraction and more accurate magnitudes. It is also testable, because the shapes of the growth curves reveal inaccurate sky subtraction or interloping objects.

Our implementation of a growth curve photometry algorithm first measures the sky value by constructing a mean flux-per-pixel profile in 1px-wide ellipses with given position angles, axis ratios, and major axis values). We use per-pixel values so as to avoid dependence on geometry, i.e. the ellipse shape, distance from the center, parts of galaxies which are outside the image frame.

We assume that flux falls off asymptotically until it is indistinguishable from the sky fluctuations. If we were fitting the slope of the mean flux per pixel profile in sufficiently wide rings, the best fit line should become horizontal at some radius, which we might then consider the edge of the galaxy. In practice this is not the case, given that incomplete masks, light from the other objects and sky gradients make the best fit slope switch from negative to slightly positive at some point.

We fit 150 px wide annuli of the flux profile using linear regression, going outwards in steps of 10 px. When the flux profile slope becomes non-negative, we take the mean of the unmasked pixels in the current annulus as the sky value, and the ellipse with major axis value at the middle of the ring as the galaxy's edge. We use the photometric galaxy center from SDSS DR7 as the starting point and position angles from light moments fitting done by the collaboration. Three colour-composite images of all the galaxies were inspected by eye and either the SDSS isophotal axis ratio or the light moments fit axis ratio was selected visually.

We have checked that this procedure gives good results and is robust even in the presence of large masked regions or faint unmasked objects. The sky values obtained were consistently lower than a simple mean of the image outside the galaxy and SDSS

sky values provided in image headers.

In the second step we construct two growth curves for each galaxy - the sky subtracted cumulative flux profiles for all pixels and for unmasked pixels only. For the vast majority of cases they do flatten, showing that the sky subtraction was accurate. Then we calculate the magnitudes using the standard prescription given at `http://www.sdss.org/dr7/algorithms/fluxcal.html#counts2mag`

Outliers and quality flags

In several cases the growth curve procedure did not work well, either producing artificially large flux values due to incomplete masking of the foreground, or missing some of the flux because of being too close to the frame border. In the first case, we used flux from non-masked pixels only, after checking that we do not lose a large fraction of the flux near the center of the galaxy.

Error estimation

Magnitude errors

First of all we estimate the error in counts as described in `http://www.sdss.org/dr7/algorithms/fluxcal.html#counterr`. The number of counts provided in the corrected SDSS frames is related to the number of photo-electrons counted by the CCDs via the inverse gain, provided with the SDSS frames:

$$photo - electrons = counts * inversegain \tag{1}$$

The contributions of the dark current and read noise are included too via the following expression:

$$error_{count} = \sqrt{([counts + sky]/inverse\ gain + Npix * (Var_d + sky_{err}))} \tag{2}$$

Here $error_{count}$ is the count error, $counts + sky$ is the sum of the counts within the galaxy without sky subtraction, $Npix$ is the number of pixels within the galaxy and dark variance $Var_d$is the total noise caused by dark current and read noise and provided by the SDSS pipeline. We used the difference between sky values for all pixels and unmasked pixels only as the sky error value:

$$sky_{err} = sky - skyM \tag{3}$$

Note that eq.3 only accounts for the Poissonian error in counts. To estimate the uncertainties due to sky subtraction, we add the difference between sky-subtracted flux and the same flux with $sky + sky_{err}$ subtracted:

$$err_{skySub} = |(allcounts\ -\ sky * Npix) - (all\ counts\ -\ (sky - sky_{err}) * Npix)| \tag{4}$$

In order to roughly estimate the influence of masked foreground objects we also add half of the difference between sky-subtracted counts of all pixels and unmasked pixels only:

$$count_{diff} = \frac{1}{2}(all\ counts\ -\ sky * Npix)\ -\ (all\ countsM - skyM * NpixM)) \quad (5)$$

$$total\ error = \sqrt{error_{count}} + \frac{1}{2} count_{diff} + err_{skySub} \quad (6)$$

Finally, the apparent magnitude uncertainty is calculated as shown at `http://www.sdss.org/dr7/algorithms/fluxcal.html#counts2mag`:

$$error(mag) = 2.5/ln(10) * total\ error/counts \quad (7)$$

Half light semi-major axis and 90% light radii errors

The main contribution to the uncertainty of these two quantities comes from errors in sky subtraction and masking errors. The former contributes to the total flux profile, whereas the latter is provided by the photometry pipeline as the difference between masked and non-masked half-light radii. We add them too.

Tests

We filled a blank image with real sky from one of the CALIFA SDSS images (140). We selected a large patch of sky outside the previously determined limit of the galaxy. The mean value of the empty sky was 122.93 counts with σ = 5.4 counts.

We created fake galaxies with GALFIT, using de Vaucouleur's profile (n = 4) and an exponential disk. Its *r* magnitude was equal to 12.76 mag, half-light radii of both profiles were set equal to 45 px, the axis ratio b/a = 0.5.

The recovered sky value for an exponential profile was 123.01 counts, for a de-Vaucouleur profile – 123.22 counts. The recovered magnitudes were 12.77 mag and 12.88 respectively, differing from the input ones by 0.01 and 0.12 mag.

Results

The growth curve magnitudes in the 5 SDSS bands are brighter than the SDSS Petrosian magnitudes by 0.78, 0.39, 0.33, 0.36 and 0.46 mag respectively, demonstrating an improvement over SDSS photometry pipeline values. The CALIFA Survey has been using the obtainedgrowth curve photometry values in the majority of its publications.

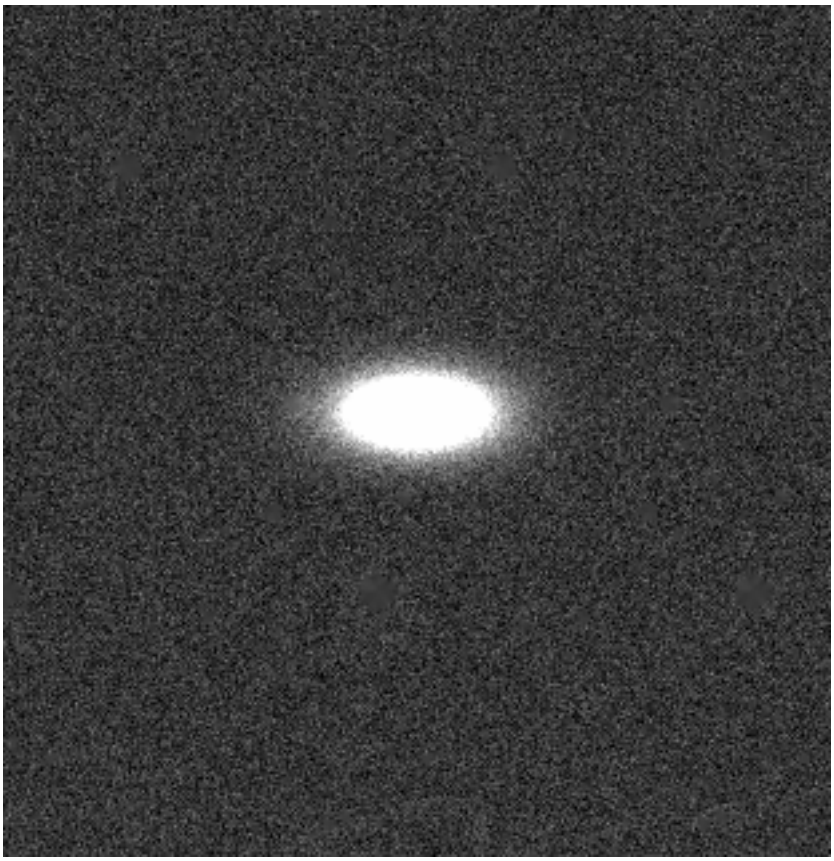

Figure 1: Simulated galaxy with an exponential profile.

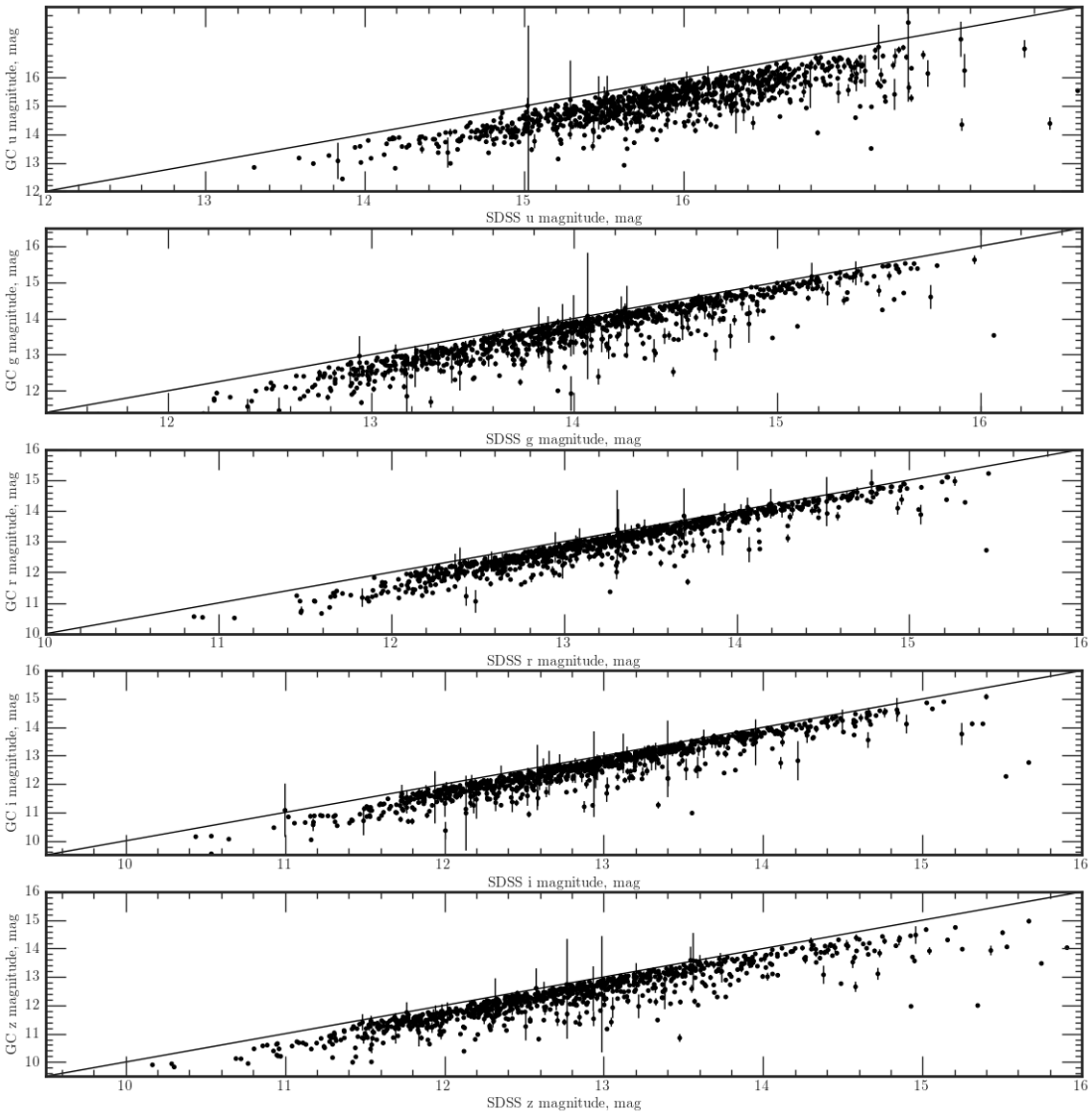
GC u magnitude, mag
SDSS u magnitude, mag
GC g magnitude, mag
SDSS g magnitude, mag
GC r magnitude, mag
SDSS r magnitude, mag
GC i magnitude, mag
SDSS i magnitude, mag
GC z magnitude, mag
SDSS z magnitude, mag

Appendix B: Two-dimensional Gaussian kernel density estimation

Bivariate Gaussian kernel density estimation

KDE is a non-parametric technique for estimating the probability density function (pdf) of the underlying distribution from a finite sample of randomly-selected points. The contribution of each datapoint is smoothed and the pdf of the unknown distribution is then evaluated.

Let us denote the bivariate data points $_1$, X_2, ..., X_n. The kernel density estimate (Rosenblatt 1956; Parzen 1962) is defined as

$$f(\mathbf{x}, H) = \frac{1}{n}\sum_{i=1}^{n} K_{\mathbf{H}}(\mathbf{x} - \mathbf{X_i}) \tag{8}$$

where $\mathbf{x}$ is a column vector of all points that we want to calculate the density at, i.e. $\mathbf{x} = (x, y)^T$, $\boldsymbol{X}_i = (X_{i1}, X_{i2})^T$, $i = 1, 2, ..., n$. $K(\mathbf{x})$ is the kernel with a bandwidth matrix $\mathbf{H}$. In the 2D Gaussian case, $\mathbf{H}$ defines the covariance matrix of the kernel. The kernel is a symmetric, unimodal probability density function such that

$$K_{\mathbf{H}}(\mathbf{x}) = |\mathbf{H}|^{-1/2} K(\mathbf{H}^{-1/2}\mathbf{x}). \tag{9}$$

Combining the above equations yields

$$f(\mathbf{x}, H) = \frac{1}{n}\sum_{i=1}^{n} |\mathbf{H}|^{-1/2} K(\mathbf{H}^{-1/2}(\mathbf{x} - \mathbf{X_i})) \tag{10}$$

The kernel function, a pdf of a 2D Gaussian with a covariance matrix $\mathbf{H}$, is defined as:

$$pdf_G = \frac{1}{2\pi \cdot \sqrt{|\mathbf{H}|}} \exp\left(-\frac{1}{2}(\mathbf{x} - \boldsymbol{\mu})^T \mathbf{H}^{-\frac{1}{2}} (\mathbf{x} - \boldsymbol{\mu})\right) \tag{11}$$

where $\boldsymbol{\mu}$ is a 2D mean vector (in our case – $\mathbf{X_i}$, the locations of datapoints the Gaussian kernels are centered on), $\mathbf{x}$ – all the points evaluated.

Substituting the 2D Gaussian pdf definition (Eq. 11) into Eq.10, we obtain

$$f(\mathbf{x}, H) = \frac{1}{n}\sum_{i=1}^{n}|\frac{1}{2\pi}|\mathbf{H}|^{-1/2}\cdot \exp\left[-\frac{1}{2}\left(\mathbf{H}^{-1/2}(\mathbf{x}-\mathbf{X_i}\right)^T \mathbf{H}^{-1/2}(\mathbf{x}-\mathbf{X_i})\right] = \\ = \frac{1}{2\pi n\sqrt{|\mathbf{H}|}}\sum_{i=1}^{n}\exp\left[-\frac{1}{2}\left((\mathbf{x}-\mathbf{X_i})^T\mathbf{H}^{-1}(\mathbf{x}-\mathbf{X_i})\right)\right] \tag{12}$$

Choosing the bandwidth matrix H

When selecting the bandwidth function, sometimes the simpler Gaussian functions with symmetric (round Gaussians) or diagonal (Gaussians with ellipse axes aligned to the coordinate axes) covariance matrixes are used. However, it is possible to use full covariance matrixes that allow choosing arbitrary sizes and orientations of the resulting Gaussians, which can lead to more accurate density estimation.

In our work, we estimate the optimal kernel bandwidth based on the global shape of the distribution and the Silverman's rule (Silverman 1986). First of all, the global covariance matrix of all the observed points is estimated, assuming that the observed points distribution is similar to a Gaussian distribution in a sense that it is unimodal, symmetric and not heavy-tailed. Then this matrix is multiplied by a scaling factor f_s derived according to the Silverman's rule (Scott & Sain 2005):

$$f_s = \left(n * \frac{d+2}{4}\right)^{-\frac{1}{d+4}} \tag{13}$$

where d is the number of dimensions, n – the number of datapoints.

Weighted KDE

Since we wanted to include the volume correction factors $1/V_{max}$, the calculations are slightly different. A weighted mean is calculated as

$$\mu_* = \sum_{i=1}^{n} w_i \mathbf{X_i} \tag{14}$$

An unbiased covariance matrix Σ of the observed points is then given as

$$\Sigma = \frac{\sum_{i=1}^{n} w_i}{\left(\sum_{i=1}^{n} w_i\right)^2 - \sum_{i=1}^{n} w_i^2} \sum_{i=1}^{n} w_i(\mathbf{X_i} - \boldsymbol{\mu}_*)^T(\mathbf{X_i} - \boldsymbol{\mu}_*) \tag{15}$$

The kernel bandwidth Σ_s is calculated by scaling Σ in the manner described above, using the Silverman's factor f_s. A weighted KDE is then calculated as

$$f(\mathbf{x}, \Sigma_s, \mathbf{w}) = \frac{\mathbf{w}}{2\pi n \sqrt{|\Sigma_s|}} \sum_{i=1}^{n} \exp\left[-\frac{1}{2}\left((\mathbf{x} - \mathbf{X_i})^T \Sigma_s^{-1} (\mathbf{x} - \mathbf{X_i})\right)\right] \tag{16}$$

Bibliography

Abramson, L. E., Williams, R. J., Benson, A. J., Kollmeier, J. A., & Mulchaey, J. S. 2014, ApJ, 793, 49

Adams, J. J., Gebhardt, K., Blanc, G. A., et al. 2012, ApJ, 745, 92

Aguerri, J. A. L., Méndez-Abreu, J., Falcón-Barroso, J., et al. 2015, A&A, 576, A102

Amram, P., Marcelin, M., Balkowski, C., et al. 1994, A&AS, 103, 5

Andersen, D. R. & Bershady, M. A. 2003, ApJ, 599, L79

Bacon, R., Accardo, M., Adjali, L., et al. 2010, in Proc. SPIE, Vol. 7735, Ground-based and Airborne Instrumentation for Astronomy III, 773508

Bacon, R., Adam, G., Baranne, A., et al. 1995, A&AS, 113, 347

Bacon, R., Copin, Y., Monnet, G., et al. 2001, MNRAS, 326, 23

Balkowski, C., Bottinelli, L., Chamaraux, P., Gouguenheim, L., & Heidmann, J. 1974, A&A, 34, 43

Barden, S. C. & Wade, R. A. 1988, in Astronomical Society of the Pacific Conference Series, Vol. 3, Fiber Optics in Astronomy, ed. S. C. Barden, 113–124

Barrera-Ballesteros, J. K., Falcón-Barroso, J., García-Lorenzo, B., et al. 2014, A&A, 568, A70

Barrera-Ballesteros, J. K., García-Lorenzo, B., Falcón-Barroso, J., et al. 2015, A&A, 582, A21

Bekeraitė, S., Walcher, J., & Falcón-Barroso, J. 2016, ApJ, accepted

Bell, E. F. & de Jong, R. S. 2001, ApJ, 550, 212

Bershady, M. A., Andersen, D. R., Harker, J., Ramsey, L. W., & Verheijen, M. A. W. 2004, PASP, 116, 565

Bershady, M. A., Verheijen, M. A. W., Swaters, R. A., et al. 2010, ApJ, 716, 198

Bertola, F., Bettoni, D., Danziger, J., et al. 1991, ApJ, 373, 369

Binney, J. & Tremaine, S. 2008, Galactic Dynamics: Second Edition (Princeton University Press)

Bland, J., Taylor, K., & Atherton, P. D. 1987, MNRAS, 228, 595

Blanton, M. R., Dalcanton, J., Eisenstein, D., et al. 2001, The Astronomical Journal, 121, 2358

Blanton, M. R., Geha, M., & West, A. A. 2008, ApJ, 682, 861

Blumenthal, G. R., Faber, S. M., Primack, J. R., & Rees, M. J. 1984, Nature, 311, 517

Blumenthal, G. R., Pagels, H., & Primack, J. R. 1982, Nature, 299, 37

Böhm, A. & Ziegler, B. L. 2007, ApJ, 668, 846

Böhm, A., Ziegler, B. L., Saglia, R. P., et al. 2004, A&A, 420, 97

Bosma, A. 1978, PhD thesis, PhD Thesis, Groningen Univ., (1978)

Bottinelli, L. 1971, A&A, 10, 437

Bowen, I. S. 1938, ApJ, 88, 113

Bryant, J. J., Owers, M. S., Robotham, A. S. G., et al. 2015, MNRAS, 447, 2857

Bundy, K., Bershady, M. A., Law, D. R., et al. 2015, ApJ, 798, 7

Calzetti, D. 2013, Star Formation Rate Indicators, ed. J. Falcón-Barroso & J. H. Knapen, 419

Cappellari, M., Bacon, R., Bureau, M., et al. 2006, MNRAS, 366, 1126

Cappellari, M. & Copin, Y. 2003, MNRAS, 342, 345

Cappellari, M. & Emsellem, E. 2004, PASP, 116, 138

Cappellari, M., Emsellem, E., Bacon, R., et al. 2007, MNRAS, 379, 418

Cappellari, M., Emsellem, E., Krajnović, D., et al. 2011a, MNRAS, 413, 813

Cappellari, M., Emsellem, E., Krajnović, D., et al. 2011b, MNRAS, 416, 1680

Catalán-Torrecilla, C., Gil de Paz, A., Castillo-Morales, A., et al. 2015, A&A, 584, A87

Chae, K.-H. 2010, MNRAS, 402, 2031

Chan, T. K., Kereš, D., Oñorbe, J., et al. 2015, MNRAS, 454, 2981

Codis, S., Pichon, C., Devriendt, J., et al. 2012, MNRAS, 427, 3320

Cole, S., Lacey, C. G., Baugh, C. M., & Frenk, C. S. 2000, MNRAS, 319, 168

Content, R. 2006, New A Rev., 50, 374

Courteau, S. 1996, ApJS, 103, 363

Courteau, S. 1997, AJ, 114, 2402

Courteau, S., Andersen, D. R., Bershady, M. A., MacArthur, L. A., & Rix, H.-W. 2003, ApJ, 594, 208

Courteau, S. & Dutton, A. A. 2015, ApJ, 801, L20

Courteau, S., Dutton, A. A., van den Bosch, F. C., et al. 2007, ApJ, 671, 203

Courteau, S. & Rix, H.-W. 1999, ApJ, 513, 561

Courtes, G. 1982, in Astrophysics and Space Science Library, Vol. 92, IAU Colloq. 67: Instrumentation for Astronomy with Large Optical Telescopes, ed. C. M. Humphries, 123

Cresci, G., Hicks, E. K. S., Genzel, R., et al. 2009, ApJ, 697, 115

Croom, S. M., Lawrence, J. S., Bland-Hawthorn, J., et al. 2012, MNRAS, 421, 872

Croton, D. J. 2013, PASA, 30, 52

Croton, D. J., Springel, V., White, S. D. M., et al. 2006, MNRAS, 365, 11

Davis, M., Efstathiou, G., Frenk, C. S., & White, S. D. M. 1985, ApJ, 292, 371

Davis, T. A., Bureau, M., Young, L. M., et al. 2011, MNRAS, 414, 968

de Zeeuw, P. T., Bureau, M., Emsellem, E., et al. 2002, MNRAS, 329, 513

Desai, V., Dalcanton, J. J., Mayer, L., et al. 2004, MNRAS, 351, 265

Di Teodoro, E. M., Fraternali, F., & Miller, S. H. 2016, A&A, 594, A77

Doroshkevich, A. G. 1970, Astrophysics, 6, 320

Drory, N., MacDonald, N., Bershady, M. A., et al. 2015, AJ, 149, 77

Dutton, A. A., Conroy, C., van den Bosch, F. C., et al. 2011, MNRAS, 416, 322

Dutton, A. A. & van den Bosch, F. C. 2009, MNRAS, 396, 141

Dutton, A. A., van den Bosch, F. C., Dekel, A., & Courteau, S. 2007, ApJ, 654, 27

Efstathiou, G. & Jones, B. J. T. 1979, MNRAS, 186, 133

Einasto, J., Kaasik, A., & Saar, E. 1974, Nature, 250, 309

Eisenhauer, F., Abuter, R., Bickert, K., et al. 2003, in Proc. SPIE, Vol. 4841, Instrument Design and Performance for Optical/Infrared Ground-based Telescopes, ed. M. Iye & A. F. M. Moorwood, 1548–1561

Eisenhauer, F. & Raab, W. 2015, ARA&A, 53, 155

Eisenstein, D. J. & Loeb, A. 1996, ApJ, 459, 432

Eke, V. R., Navarro, J. F., & Steinmetz, M. 2001, ApJ, 554, 114

Emsellem, E., Cappellari, M., Krajnović, D., et al. 2011, MNRAS, 414, 888

Emsellem, E., Cappellari, M., Krajnović, D., et al. 2007, MNRAS, 379, 401

Fabry, C. & Perot, A. 1901, ApJ, 13, 265

Falcón-Barroso, J., Lyubenova, M., & van de Ven, G. 2015a, in IAU Symposium, Vol. 311, Galaxy Masses as Constraints of Formation Models, ed. M. Cappellari & S. Courteau, 78–81

Falcón-Barroso, J., Lyubenova, M., & van de Ven, G. 2015b, in IAU Symposium, Vol. 311, IAU Symposium, ed. M. Cappellari & S. Courteau, 78–81

Falcón-Barroso, J., Lyubenova, M., & van de Ven, G. 2016, A&A, submitted

Falcón-Barroso, J., Lyubenova, M., van de Ven, G., Mendez-Abreu, J., & et al. submitted, A&A

Fall, S. M. 1983, in IAU Symposium, Vol. 100, Internal Kinematics and Dynamics of Galaxies, ed. E. Athanassoula, 391–398

Flores, H., Hammer, F., Puech, M., Amram, P., & Balkowski, C. 2006, A&A, 455, 107

Foreman-Mackey, D., Conley, A., Meierjurgen Farr, W., et al. 2013, emcee: The MCMC Hammer, Astrophysics Source Code Library

Franx, M. & de Zeeuw, T. 1992, ApJ, 392, L47

Fraser, G. W. 2009, X-ray Detectors in Astronomy

García-Benito, R., Zibetti, S., Sánchez, S. F., et al. 2015, A&A, 576, A135

García-Lorenzo, B., Márquez, I., Barrera-Ballesteros, J. K., et al. 2015, A&A, 573, A59

Garrido, O., Marcelin, M., & Amram, P. 2004, MNRAS, 349, 225

Giovanelli, R., Haynes, M. P., Herter, T., et al. 1997, AJ, 113, 53

Giovanelli, R., Haynes, M. P., Kent, B. R., et al. 2005, AJ, 130, 2598

Gnedin, O. Y., Weinberg, D. H., Pizagno, J., Prada, F., & Rix, H.-W. 2007, ApJ, 671, 1115

Gnerucci, A., Marconi, A., Cresci, G., et al. 2011, A&A, 528, A88

Gonzalez, A. H., Williams, K. A., Bullock, J. S., Kolatt, T. S., & Primack, J. R. 2000, ApJ, 528, 145

Goodman, J. & Weare, J. 2010, Communications in Applied Mathematics and Computational Science, 5, 65

Governato, F., Willman, B., Mayer, L., et al. 2007, MNRAS, 374, 1479

Green, A. W., Glazebrook, K., McGregor, P. J., et al. 2014, MNRAS, 437, 1070

Guth, A. H. 1981, Phys. Rev. D, 23, 347

Hagen, N. & Kudenov, M. W. 2013, Optical Engineering, 52, 090901

Hahn, O., Porciani, C., Carollo, C. M., & Dekel, A. 2007, MNRAS, 375, 489

Hall, M., Courteau, S., Dutton, A. A., McDonald, M., & Zhu, Y. 2012, MNRAS, 425, 2741

Haynes, M. P., Giovanelli, R., Martin, A. M., et al. 2011, AJ, 142, 170

Hill, G. J., Gebhardt, K., Komatsu, E., et al. 2008, in Astronomical Society of the Pacific Conference Series, Vol. 399, Panoramic Views of Galaxy Formation and Evolution, ed. T. Kodama, T. Yamada, & K. Aoki, 115

Holmes, L., Spekkens, K., Sánchez, S. F., et al. 2015, MNRAS, 451, 4397

Hubble, E. P. 1926, ApJ, 64, 321

Husemann, B., Jahnke, K., Sánchez, S. F., et al. 2013, A&A, 549, A87

Jimenez, R., Slosar, A., Verde, L., et al. 2010, MNRAS, 404, 975

Jones, E., Oliphant, T., Peterson, P., et al. 2001-2015, SciPy: Open source scientific tools for Python, [Online; accessed 2015-06-17]

Kalinova, V. & Lyubenova, M. 2015, PhD thesis, Univ. Heidelberg

Kalinova, V., van de Ven, G., Lyubenova, M., Falcón-Barroso, J., & et al. submitted, MNRAS

Klypin, A., Karachentsev, I., Makarov, D., & Nasonova, O. 2015, MNRAS, 454, 1798

Klypin, A. A., Trujillo-Gomez, S., & Primack, J. 2011, ApJ, 740, 102

Kochanek, C. S. & White, M. 2001, ApJ, 559, 531

Koda, J., Sofue, Y., & Wada, K. 2000, ApJ, 532, 214

Krajnović, D., Bacon, R., Cappellari, M., et al. 2008, MNRAS, 390, 93

Laurent, F., Adjali, L., Arns, J., et al. 2010, in Proc. SPIE, Vol. 7739, Modern Technologies in Space- and Ground-based Telescopes and Instrumentation, 77394M

Le Fèvre, O., Saisse, M., Mancini, D., et al. 2003, in Proc. SPIE, Vol. 4841, Instrument Design and Performance for Optical/Infrared Ground-based Telescopes, ed. M. Iye & A. F. M. Moorwood, 1670–1681

Lee, J. & Erdogdu, P. 2007, ApJ, 671, 1248

Leroy, A. K., Walter, F., Brinks, E., et al. 2008, AJ, 136, 2782

Libeskind, N. I., Hoffman, Y., Knebe, A., et al. 2012, MNRAS, 421, L137

Linde, A. D. 1982, Physics Letters B, 108, 389

Lyubenova, M., Martín-Navarro, I., van de Ven, G., et al. 2016, MNRAS, 463, 3220

Macciò, A. V., Udrescu, S. M., Dutton, A. A., et al. 2016, MNRAS, 463, L69

Maller, A. H., Berlind, A. A., Blanton, M. R., & Hogg, D. W. 2009, ApJ, 691, 394

Marcelin, M. & Athanassoula, E. 1982, A&A, 105, 76

Martinsson, T. P. K., Verheijen, M. A. W., Westfall, K. B., et al. 2013, A&A, 557, A131

Masters, K. L., Springob, C. M., Haynes, M. P., & Giovanelli, R. 2006, ApJ, 653, 861

McCarthy, I. G., Schaye, J., Font, A. S., et al. 2012, MNRAS, 427, 379

McGaugh, S. S., Schombert, J. M., Bothun, G. D., & de Blok, W. J. G. 2000, ApJ, 533, L99

Meyer, M. J., Zwaan, M. A., Webster, R. L., Schneider, S., & Staveley-Smith, L. 2008, MNRAS, 391, 1712

Miller, S. H., Bundy, K., Sullivan, M., Ellis, R. S., & Treu, T. 2011, ApJ, 741, 115

Miller, S. H., Ellis, R. S., Sullivan, M., et al. 2012, ApJ, 753, 74

Miller, S. H., Sullivan, M., & Ellis, R. S. 2013, ApJ, 762, L11

Mo, H., Van den Bosch, F., & White, S. 2010, Galaxy formation and evolution (Cambridge University Press)

Mould, J. R., Huchra, J. P., Freedman, W. L., et al. 2000, ApJ, 529, 786

Naab, T., Oser, L., Emsellem, E., et al. 2014, MNRAS, 444, 3357

Neistein, E., Maoz, D., Rix, H.-W., & Tonry, J. L. 1999, AJ, 117, 2666

Neumayer, N., Walcher, C. J., Andersen, D., et al. 2011, MNRAS, 413, 1875

Newman, J. A. & Davis, M. 2000, ApJ, 534, L11

Newman, J. A. & Davis, M. 2002, ApJ, 564, 567

Nicholson, R. A., Bland-Hawthorn, J., & Taylor, K. 1992, ApJ, 387, 503

Obreschkow, D. & Glazebrook, K. 2014, ApJ, 784, 26

Obreschkow, D., Ma, X., Meyer, M., et al. 2013, ApJ, 766, 137

Obreschkow, D. & Meyer, M. 2013, ApJ, 777, 140

Okamura, S., Yasuda, N., Shimasaku, K., Yagi, M., & Weinberg, D. H. 1999, Publications of the Astronomical Society of the Pacific, 111, 31

Opik, E. 1922, ApJ, 55, 406

Ostriker, J. P. & Peebles, P. J. E. 1973, ApJ, 186, 467

Papastergis, E., Martin, A. M., Giovanelli, R., & Haynes, M. P. 2011, ApJ, 739, 38

Parzen, E. 1962, Ann. Math. Statist., 33, 1065

Peebles, P. J. E. 1969, ApJ, 155, 393

Peebles, P. J. E. 1971, A&A, 11, 377

Perlmutter, S., Aldering, G., Goldhaber, G., et al. 1999, ApJ, 517, 565

Persic, M. & Salucci, P. 1991, ApJ, 368, 60

Persic, M., Salucci, P., & Stel, F. 1996, MNRAS, 281, 27

Petrosian, V. 1976, The Astrophysical Journal, 209, L1

Pizagno, J., Prada, F., Weinberg, D. H., et al. 2007, AJ, 134, 945

Planck Collaboration, Ade, P. A. R., Aghanim, N., et al. 2014, A&A, 571, A22

Puech, M., Flores, H., Hammer, F., et al. 2008, A&A, 484, 173

Querejeta, M., Eliche-Moral, M. C., Tapia, T., et al. 2015, A&A, 579, L2

Riess, A. G., Filippenko, A. V., Challis, P., et al. 1998, AJ, 116, 1009

Rix, H.-W., Guhathakurta, P., Colless, M., & Ing, K. 1997, MNRAS, 285, 779

Roberts, M. S. 1969, AJ, 74, 859

Roberts, M. S. 1976, Comments on Astrophysics, 6, 105

Robotham, A. & Obreschkow, D. 2015, MNRAS, submitted

Rodríguez, S. & Padilla, N. D. 2013, MNRAS, 434, 2153

Rogstad, D. H., Wright, M. C. H., & Lockhart, I. A. 1976, ApJ, 204, 703

Romanowsky, A. J. & Fall, S. M. 2012, ApJS, 203, 17

Rosenblatt, M. 1956, Ann. Math. Statist., 27, 832

Roth, M. M., Kelz, A., Fechner, T., et al. 2005, PASP, 117, 620

Rubin, V. C., Burstein, D., Ford, Jr., W. K., & Thonnard, N. 1985, ApJ, 289, 81

Rubin, V. C. & Ford, Jr., W. K. 1970, ApJ, 159, 379

Rubin, V. C., Thonnard, N., & Ford, Jr., W. K. 1978, ApJ, 225, L107

Saintonge, A. & Spekkens, K. 2011, ApJ, 726, 77

Sánchez, S. F., García-Benito, R., Zibetti, S., et al. 2016, A&A, 594, A36

Sánchez, S. F., Kennicutt, R. C., Gil de Paz, A., et al. 2012, A&A, 538, A8

Sánchez, S. F., Rosales-Ortega, F. F., Iglesias-Páramo, J., et al. 2014, A&A, 563, A49

Schäfer, B. M. 2009, International Journal of Modern Physics D, 18, 173

Schmidt, B. P., Suntzeff, N. B., Phillips, M. M., et al. 1998, ApJ, 507, 46

Schmidt, M. 1968, ApJ, 151, 393

Schommer, R. A., Bothun, G. D., Williams, T. B., & Mould, J. R. 1993, AJ, 105, 97

Scott, D. W. 1979, Biometrika, 66, pp. 605

Scott, D. W. & Sain, S. R. 2005, Handbook of Statistics, 24, 229

Sharples, R., Bender, R., Bennett, R., et al. 2006, New A Rev., 50, 370

Sheth, R. K., Mo, H. J., & Tormen, G. 2001, MNRAS, 323, 1

Shostak, G. S. 1975, ApJ, 198, 527

Silverman, B. W. 1986, Density estimation for statistics and data analysis, Vol. 26 (CRC press)

Slosar, A., Land, K., Bamford, S., et al. 2009, MNRAS, 392, 1225

Springel, V., White, S. D. M., Jenkins, A., et al. 2005, Nature, 435, 629

Steinmetz, M. & Navarro, J. F. 1999, ApJ, 513, 555

Strauss, M. A., Weinberg, D. H., Lupton, R. H., et al. 2002, The Astronomical Journal, 124, 1810

Swinbank, A. M., Bower, R. G., Smith, G. P., et al. 2006, MNRAS, 368, 1631

Tempel, E. & Libeskind, N. I. 2013, ApJ, 775, L42

Tempel, E., Stoica, R. S., & Saar, E. 2013, MNRAS, 428, 1827

Tonini, C., Maraston, C., Ziegler, B., et al. 2011, MNRAS, 415, 811

Trowland, H. E., Lewis, G. F., & Bland-Hawthorn, J. 2013, ApJ, 762, 72

Trujillo, I., Carretero, C., & Patiri, S. G. 2006, ApJ, 640, L111

Trujillo-Gomez, S., Klypin, A., Primack, J., & Romanowsky, A. J. 2011, ApJ, 742, 16

Tully, R. B. & Fisher, J. R. 1977, A&A, 54, 661

Tully, R. B. & Pierce, M. J. 2000, ApJ, 533, 744

Valdes, F., Gupta, R., Rose, J. A., Singh, H. P., & Bell, D. J. 2004, ApJS, 152, 251

van Albada, T. S. & Sancisi, R. 1986, Philosophical Transactions of the Royal Society of London Series A, 320, 447

van den Bosch, F. C. 2000, ApJ, 530, 177

van den Bosch, F. C., Abel, T., Croft, R. A. C., Hernquist, L., & White, S. D. M. 2002, ApJ, 576, 21

van den Bosch, F. C., Robertson, B. E., Dalcanton, J. J., & de Blok, W. J. G. 2000, AJ, 119, 1579

Vanderriest, C. 1980, PASP, 92, 858

Verheijen, M. A. W. 2001, ApJ, 563, 694

Verheijen, M. A. W., Bershady, M. A., Andersen, D. R., et al. 2004, Astronomische Nachrichten, 325, 151

Vogelsberger, M., Genel, S., Sijacki, D., et al. 2013, MNRAS, 436, 3031

Vogelsberger, M., Genel, S., Springel, V., et al. 2014a, Nature, 509, 177

Vogelsberger, M., Genel, S., Springel, V., et al. 2014b, MNRAS, 444, 1518

Vogt, N. P., Forbes, D. A., Phillips, A. C., et al. 1996, ApJ, 465, L15

Walcher, C. J., Lamareille, F., Vergani, D., et al. 2008, A&A, 491, 713

Walcher, C. J., Wisotzki, L., Bekeraité, S., et al. 2014, A&A, 569, A1

Walter, F., Brinks, E., de Blok, W. J. G., et al. 2008, AJ, 136, 2563

Weijmans, A.-M., de Zeeuw, P. T., Emsellem, E., et al. 2014, MNRAS, 444, 3340

Weijmans, A.-M., Krajnović, D., van de Ven, G., et al. 2008, MNRAS, 383, 1343

Weitzel, L., Krabbe, A., Kroker, H., et al. 1996, A&AS, 119, 531

White, S. D. M. & Rees, M. J. 1978, MNRAS, 183, 341

Wild, V., Charlot, S., Brinchmann, J., et al. 2011a, MNRAS, 417, 1760

Wild, V., Groves, B., Heckman, T., et al. 2011b, MNRAS, 410, 1593

Williams, M. J., Bureau, M., & Cappellari, M. 2009, in Astronomical Society of the Pacific Conference Series, Vol. 419, Galaxy Evolution: Emerging Insights and Future Challenges, ed. S. Jogee, I. Marinova, L. Hao, & G. A. Blanc, 167

Wilson, T. L., Rohlfs, K., & Hüttemeister, S. 2013, Tools of Radio Astronomy

Wyatt, Jr., S. P. & Brown, F. G. 1955, AJ, 60, 415

Yegorova, I. A. & Salucci, P. 2007, MNRAS, 377, 507

Yıldırım, A., van den Bosch, R. C. E., van de Ven, G., et al. 2016, MNRAS, 456, 538

Ziegler, B. L., Böhm, A., Fricke, K. J., et al. 2002, ApJ, 564, L69

Zwaan, M. A., Meyer, M. J., & Staveley-Smith, L. 2010, MNRAS, 403, 1969

Zwaan, M. A., Staveley-Smith, L., Koribalski, B. S., et al. 2003, AJ, 125, 2842

Zwicky, F. 1937, ApJ, 86, 217

Acknowledgements

I want first of all to thank to my supervisors Lutz Wisotzki, C.J. Walcher and M. Roth, without whose unwavering patience and support this thesis would not have been completed. I am grateful to Jakob, in particular, for his kindness and perseverance in pushing me forward.

Among the many friends, mentors and dear colleagues I have met at AIP, I would like to especially thank Metin Ata, Friedrich Anders, Christian Herenz, Bernd Husemann, Daniel Kupko, Sebastian Kamann, Maneenate Wechakama, Karl-Heinz Boening and Antje Timmermann. I would also like to extend my gratitude to Sebástian Sanchez, Glenn van de Ven, Mariya Lyubenova, Danail Obreshkow, Jesus Falcón Barroso, Vivienne Wild, Bodo Ziegler, Veselina Kalinova, Joss Bland-Hawthorn, Kristine Spekkens, Martin A. Zwaan and many more scientists who inspired and supported me during my PhD studies. In particular, I would like to thank the CALIFA collaboration for being such a welcoming and supportive environment for a fledgling scientist.

A special thanks goes to my friends: Karolis Tamulis, Urtė Sabutytė, Augustė Vickūnaitė, Kipras Britkus, *ffwd*, Tomas Verbaitis and Maryja Šupa, Lilija Duoblienė, Eglė Marija Ramanauskaitė, Aleksas and Dolita, Technarium and XI20 crew. I am forever grateful to Jurgita, Hagen and the rest of the Pelka family for welcoming me to Berlin.

I would not have thought of starting a PhD in a foreign country without Albertas Mickėnas. May all cats be friends with you.

Tomas Bekeris has always made me do my best during the long last years of the PhD process – thank you for this, and for many other things.

Lastly, I would like to thank my parents, Lina and Levas, and my siblings Adomas and Marija, who nurtured my curiosity, sacrificed so much for my education, and believed in me even when I failed to explain what and why I was doing.